Geophys. J. Int. (1994) **119,** 893–930

Location of the Africa–Australia–India triple junction and motion between the Australian and Indian plates: results from an aeromagnetic investigation of the Central Indian and Carlsberg ridges

Charles DeMets,[1] Richard G. Gordon[2,*] and Peter Vogt[3]

[1] 1215 *West Dayton St, Department of Geology and Geophysics, University of Wisconsin, Madison,* WI 53706, *USA*
[2] *Laboratoire de Géodynamique Sous-Marine, BP 48,* 06230 *Villefranche-sur-Mer, France*
[3] *Code 5110, Naval Research Laboratory, Washington,* DC 20375, *USA*

Accepted 1994 June 7. Received 1994 May 23; in original form 1993 May 24

SUMMARY

Prior studies have proposed and examined the hypothesis that India and Australia are separate rigid plates separated by a wide, near-equatorial, E–W striking, plate boundary. Attempts to place narrow limits on the location of the Africa–Australia–India triple junction have been hindered, however, by the lack of useful magnetic profiles crossing the eastern Carlsberg Ridge and northern Central Indian Ridge. Herein we present near-ridge portions of new profiles from an aeromagnetic survey of the Carlsberg Ridge east of 66°E and of the Central Indian Ridge north of 19°S. These new data are used to estimate 35 new spreading rates averaged from the middle of chron 2A (3.03 Ma) to the present. All other plate motion data along the Central Indian and Carlsberg ridges are also analysed to investigate the present kinematics of the Indian Ocean, especially the motion and boundary between the Indian and Australian plates. Unlike prior efforts, we objectively estimate uncertainties in the strikes of transform faults along the Carlsberg and Central Indian ridges.

Indian Ocean plate motion data are unambiguously inconsistent with a model in which India and Australia lie on the same rigid plate, but remain consistent with the existence of distinct and rigid Indian and Australian plates. The plate motion data also remain consistent with closure of the Africa–Arabia–India plate motion circuit. The data are consistent with closure of the Africa–Antarctic–Australia plate motion circuit and place an upper bound of 7 mm yr^{-1} on the summed deformation around the Rodriguez triple junction if we have accurately estimated the errors in the data. From data along the Carlsberg and Central Indian Ridges, 95 per cent confidence limits on the location of the Africa–Australia–India triple junction are 6.2°S to ~9°S if the boundary between India and Australia is discrete (i.e. very narrow) where it intersects the Central Indian Ridge. When closure is enforced about the Owen and Rodriguez triple junctions, these limits decrease to 8°S–9°S, which is centred on the Vema fracture zone and is more than 10 times narrower than we found without the new data. The resulting specific prediction of the location of, and velocity across, a hypothetical narrow boundary between the Indian and Australian plates permits us to test the hypothesis of a narrow boundary. Available data suggest, but do not prove, that no such narrow boundary accommodating the predicted direction of

* Now at: Department of Geological Sciences, Northwestern University, Evanston, IL 60208-2150, USA.

motion exists. We think it likely that the motion is taken up on many fracture zones between ~8°S and ~4°S, which is an interval containing most of the near-, but off-ridge, seismicity.

The confidence limits on the new angular velocities, especially those describing the motion between India and either Africa or Australia, are much smaller than we found before. In particular the NW-oriented axis of the confidence ellipse of the India–Australia pole of rotation is seven times smaller than we found before. The shrinking of these uncertainties is accompanied by a shrinking of the uncertainties in the predicted velocities between India and Australia. For example, a point (8.5°S, 68.3°E) assumed to be on the Australian plate near the Central Indian Ridge moves 5.1 ± 2.2 mm yr^{-1} toward S38 ± 12°E (95 per cent confidence limits) relative to the Indian plate, indicating net divergence of Australia from India along a N–S profile near the Central Indian Ridge. A point (11°S, 90°E) assumed to be on the Australian plate near the Ninetyeast Ridge moves 9.8 ± 2.4 mm yr^{-1} toward N27 ± 12°E relative to the Indian plate, indicating net convergence of Australia toward India along a N–S profile through the Ninetyeast Ridge. These now very specific predictions remain consistent with independent data that indicate the orientation and (to a lesser extent) the rate of deformation in the zone between India and Australia. The data reinforce our earlier conclusion that the most important way in which shortening is taken up in the non-subducting convergent portion of the plate boundary, i.e. the eastern portion, is by strike-slip faulting and north-eastward delivery of oceanic lithosphere to the Java–Sumatra trench.

Key words: Africa, Australia, geomagnetic field, India, plate motion, triple junction.

INTRODUCTION

For 25 years, the theory of plate tectonics has provided the framework for simply and comprehensively describing the large-scale horizontal motions of the surface of the solid Earth. Plate tectonics has been and continues to be useful because of its predictive capabilities. The geometrical precision and rigour provided by the assumption of plate rigidity, combined with accurately navigated magnetic and bathymetric surveys, allows horizontal displacements to be determined accurately over most of Earth's surface. Many of the most important problems today, however, are in examining the limits of plate tectonics and in discovering the ways in which the original theory must be modified. Increasingly rigorous tests of plate tectonics have identified some oceanic regions in which the model of rigid plates separated by narrow plate boundaries breaks down. The largest of these regions is in the equatorial Indian Ocean, which has been cited many times as the type example of oceanic 'intraplate' deformation (Fig. 1).

Much evidence suggests that a wide zone of near-equatorial lithosphere between the Central Indian Ridge and the Sumatra Trench is deforming. Evidence includes thrust faulting and undulations of the basement revealed by reflection seismic profiling (Curray & Moore 1971; Eittreim & Ewing 1972; Weissel, Anderson & Geller 1980; Geller, Weissel & Anderson 1983; Curray & Munasinghe 1989; Bull 1990; Bull & Scrutton 1990; Chamot-Rooke *et al.* 1993), lineated gravity and geoid anomalies that accompany the basement undulations (Weissel *et al.* 1980; McAdoo & Sandwell 1985; Haxby 1987; Zuber 1987), and large earthquakes along and near Ninetyeast Ridge, between Ninetyeast Ridge and Chagos-Laccadive Ridge in the southern Bay of Bengal and Ceylon Abyssal Plain, and near and along the Chagos–Laccadive Ridge (Gutenberg & Richter 1954; Sykes 1970; Stein & Okal 1978; Wiens & Stein 1984; Bergman, Nabelek & Solomon 1984; Bergman & Solomon 1985; Wiens 1986; Petroy & Wiens 1989). Global plate motion models published in 1978 (Chase 1978; Minster & Jordan 1978) were unable to fit the plate motion data along the three boundaries that meet at the Rodriguez triple junction. Minster & Jordan (1978) attributed the non-closure of this plate motion circuit to possible intraplate deformation or a diffuse plate boundary along the Ninetyeast Ridge and possibly continuing southward to the Southeast Indian Ridge.

Understanding this deforming zone is important. Significant distributed deformation in oceanic lithosphere is rare. Thus, this region is the largest of few that contain information (other than a lower bound) on the strength of oceanic lithosphere. It is also the largest of few that can be compared with the many wide deforming zones on the continents. The deformation in this zone seems surely connected with the great uplift of the Tibetan plateau and the Himalayan mountains. The processes and evolution of the equatorial deforming zone may provide insights into processes and evolution of the plateau and mountains.

Whether this deforming zone represents intraplate deformation or a wide plate boundary is also important. If it is intraplate deformation, the high deformation rates would imply that the predictions of plate tectonics are very uncertain. In any event, the existence of this deforming zone conflicts with the widely held belief that oceanic lithosphere is composed of rigid plates separated only by narrow boundaries.

In the original model for the plate geometry of the Indian

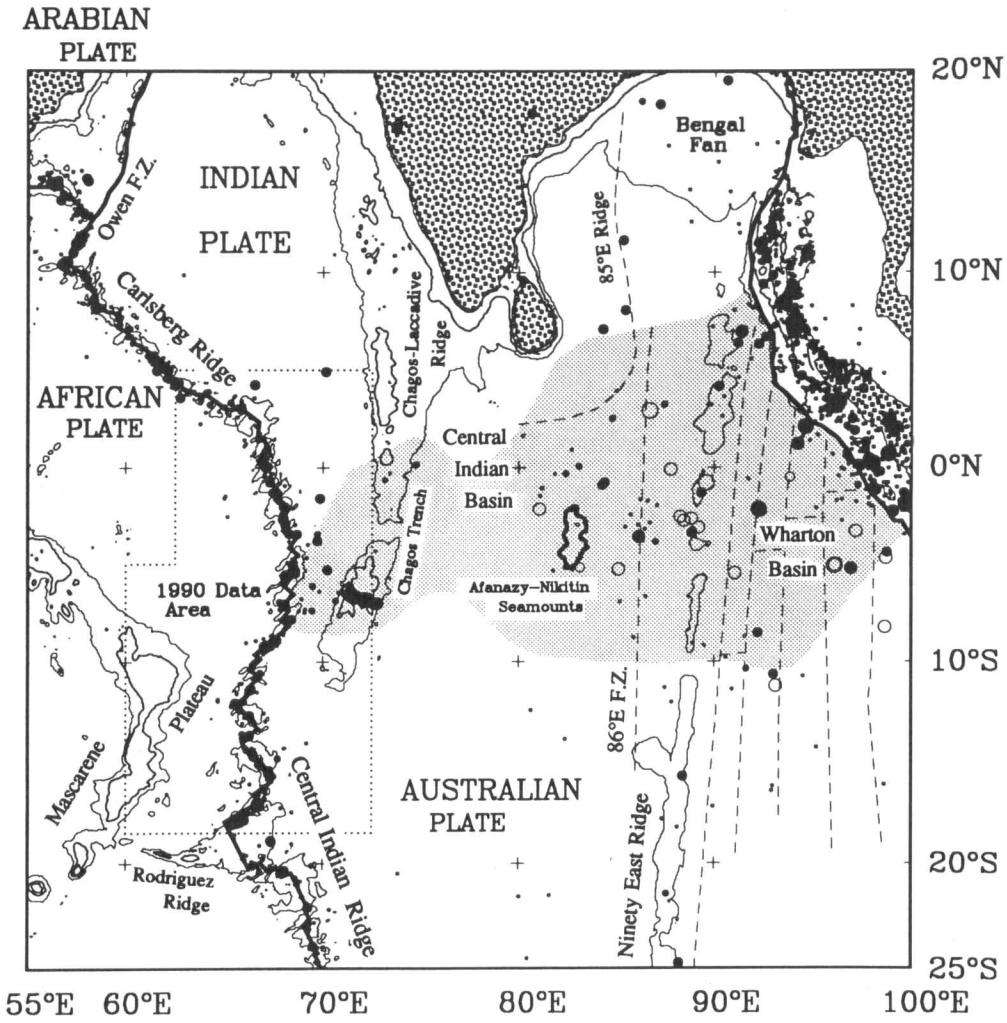

Figure 1. Location map showing the approximate extent of distributed sea-floor deformation between the Indian and Australian plates (shaded region). The dotted line encloses the area where new aeromagnetic profiles were obtained. Dashed lines show inferred locations of fracture zones (Curray *et al.* 1982; Liu, Curray & McDonald 1983). Open circles show shallow, pre-1963 earthquakes (Petroy & Wiens 1989). Solid circles show shallow earthquakes from 1963 to 1988 from the Earthquake Data File from the National Geophysical Data Center along with five earthquakes from 1988 to 1991 with m_b exceeding 4.5 from the Harvard centroid moment tensor catalogues. Bathymetric contours are at 1000 and 3000 m. This and later maps are produced using Mercator's projection.

Ocean (Wilson 1965; Mckenzie & Sclater 1971; Chase 1978; Minster & Jordan 1978), India and Australia were hypothesized to be on the same plate, the Indo-Australian plate, which was separated on the west from the Arabian plate by the Owen fracture zone. In 1985 we and our colleagues proposed a new Indian Ocean plate geometry in which India and Australia lie on distinct plates separated by a wide E–W striking plate boundary in the equatorial Indian Ocean (Wiens *et al.* 1985). In a series of papers we showed that this model, with some modifications, was successful in several ways. All available plate motion data from the Indian Ocean are consistent with a five-plate model consisting of the African, Antarctic, Arabian, Australian and Indian plates. Moreover, the motion between India and Australia predicted from the rigid-plate model, although highly uncertain, agrees well with independent data that indicate the orientation of deformation in the wide plate boundary, the key observations being N–S to NW–SE shortening in the deforming belt east of the pole of rotation, and N–S stretching in the deforming belt west of the pole of rotation. The region near the pole is expected to deform very slowly; the absence of observable deformation is consistent with this expectation. Because of the consistency with plate motion data, the explanatory and predictive power of the model, and the quantification attained, these results strongly suggest that it is more useful to treat this deforming zone as a wide plate boundary rather than as a zone of intraplate deformation (DeMets, Gordon & Argus 1988; Gordon & DeMets 1989; Gordon, DeMets & Argus 1990).

In our prior studies we tried to do as much as was possible with available data. A strong limitation on what could be accomplished was the paucity of magnetic profiles along the northern Central Indian Ridge and eastern Carlsberg Ridge, with very few profiles lying between 4°N and 15°S. Many of the profiles available outside of this zone were collected at

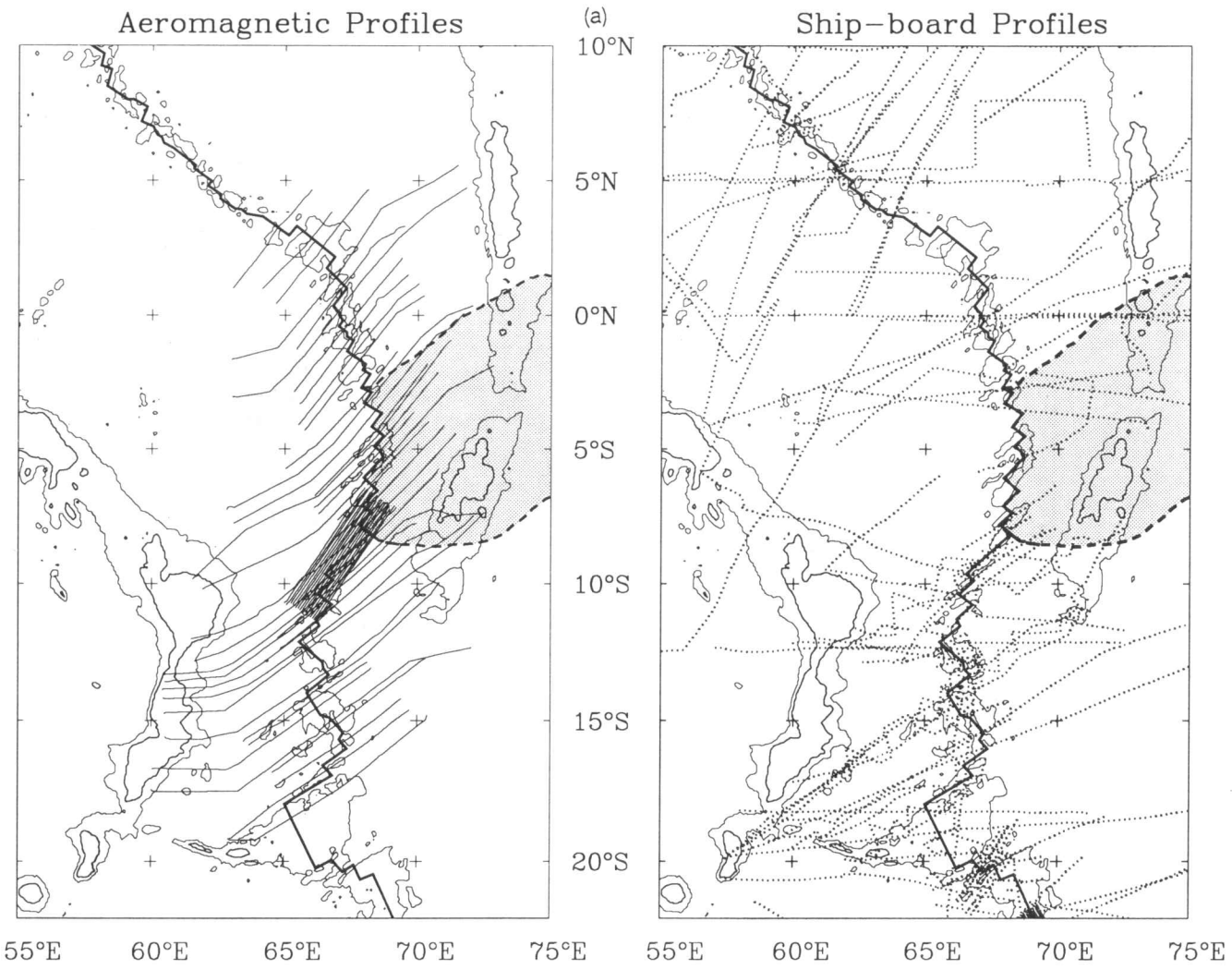

Figure 2. (a) Left: Flight tracks from the 1990 Diego Garcia aeromagnetic experiment. Right: Tracks of oceanographic cruises with near-ridge magnetic data. Only track segments striking within ~60° of the fracture zones and with magnetic sampling intervals short enough to record crustal magnetic anomalies are shown. (b) Locations of spreading rates (squares) and transform-fault azimuths (circles) along the Central Indian and Carlsberg ridges.

high angles to plate-motion flow lines and thus crossed fracture zones; many profiles, especially those across the Carlsberg Ridge, were collected before the widespread use of satellite navigation.

To remedy the lack of useful plate motion data along much of the Central Indian and Carlsberg ridges, we conducted an aeromagnetic survey between 18.5°S and 3.5°N, and between 60°E and 72°E, encompassing nearly the entire 2200 km of the most sparsely surveyed section of the ridge (Figs 1 and 2). We also examined over 100 archived cruises and found that more than 40 of them provide useful supplemental data. Here we report on these data and use the near-ridge portions of the new profiles to estimate new spreading rates, which in turn are used to test our prior models more rigorously and to narrow the uncertainty on estimated parameters. We also use the results of a recent GLORIA survey of part of the Central Indian Ridge (Parson *et al.* 1993) to estimate transform azimuths and their uncertainties.

We investigate the following questions. Are the new data from the Carlsberg and Central Indian ridges inconsistent with motion between an assumed-rigid African plate and an assumed-rigid Indo-Australian plate, as previously concluded from sparser data? If so, are the data consistent with the existence of two rigid plates, the Indian plate and the Australian plate, lying to the east and north-east of the Central Indian and Carlsberg ridges and moving relative to an assumed-rigid African plate? If so, where does the boundary between the Indian and Australian plates intersect the Central Indian or Carlsberg ridge, and how wide is the boundary? Are the observations consistent with a narrow boundary between India and Australia? If it is not narrow, but wide, how is deformation accommodated and what structures take up the deformation? Are the independently observed indicators of the orientation and rate of deformation within the near-equatorial deforming zone consistent with the motion predicted between the assumed-rigid Indian and Australian plates?

In this paper, we describe the motion between a pair of plates by an angular velocity, which is a vector. It is

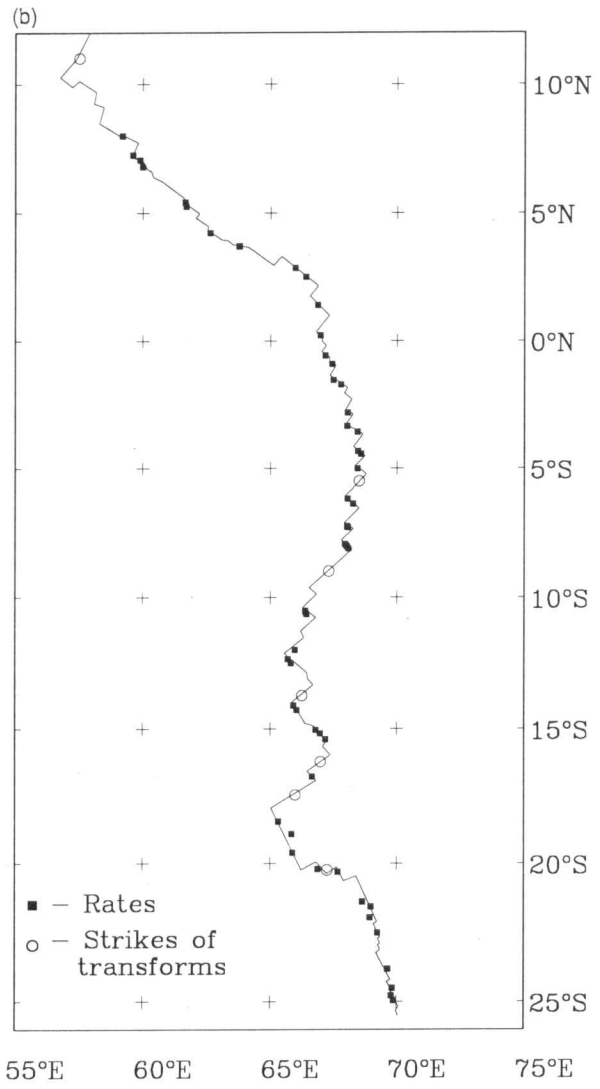

Figure 2. (*Continued.*)

commonly described either by its three Cartesian components or by its latitude, longitude and rotation rate. We refer to its orientation as a pole of rotation, which is most conveniently specified by its latitude and longitude. An angular velocity derived only from data along a single plate boundary is termed a *best-fitting* angular velocity, whereas an angular velocity (for the same plate pair) derived only from data from all other relevant plate boundaries is termed a *closure-fitting* angular velocity (Minster *et al.* 1974; Minster & Jordan 1984). When an angular velocity is calculated subject to the constraint of plate circuit closure, it is termed a *closure-enforced* angular velocity, and in the case of enforcement of closure about a three-plate circuit, it is sometimes referred to as a *three-plate* angular velocity. Herein we take the Carlsberg Ridge to be that part of the mid-ocean ridge system that lies east-south-east of the Owen transform fault but north and north-west of about 2°S, 68°E. We take the Central Indian Ridge to be that part of the mid-ocean ridge system that lies south of 2°S and north of the Rodriguez triple junction. For consistency with our prior work in the Indian Ocean and with spreading rates used in the NUVEL-1 global plate motion model (DeMets *et al.* 1990), we use the time-scale of Harland *et al.* (1982) to estimate spreading rates.

AEROMAGNETIC SURVEY

Survey design and data acquisition

Most of our flight time was devoted to 35 long flight lines consisting of 39 flight segments each up to 1592 km long. Together these sum to 37 500 km of profile. The flight lines were designed to be parallel to known fracture-zone strikes and synthetic plate-motion flow lines. Our results and interpretation indicate that these lines sample magnetic anomalies in 24 distinct fracture zone corridors between 18.5°S and 3.3°N (Fig. 2). That we have identified long correlatable sequences of anomalies for nearly all the new long profiles suggests that we rarely crossed fracture zones or pseudo-faults, a conclusion that is further corroborated by tectonic interpretations of high-resolution altimetry data (P. Vogt, unpublished chart). Eighteen ~580 km long profiles spaced 8 km apart and totalling 10 408 km in length were flown to obtain higher resolution data in the vicinity of the Vema transform fault (Fig. 2). These 18 closely spaced lines plus the 39 flight segments composing the 35 long flight lines add up to a total of 47 908 km of new aeromagnetic track, shown in Fig. 2.

The data were collected during 14 flights on a Naval Research Laboratory P-3 Orion between 1990 April 24 and 1990 May 21. The P-3 Orion is a 117 foot long, four turbo-propeller aeroplane that is capable of extended flights exceeding 3200 km. Each flight started and ended at Diego Garcia Naval Air Base (Fig. 3) and typically lasted 10–11 hr. Flight altitudes were 300 to 900 m above the sea surface and were varied in response to the local weather and the size of background magnetic noise fluctuations. The mean water depth in the survey region (20°S–5°N, 60°E–73°E) is 3.5 km, with depths ranging from sea-level (above the Chagos Bank) to 6 km in the Vema transform fault valley (Fisher, Jantsch & Comer 1982), giving an average height of 3.8 km above the sea-floor. Magnetic field intensity was recorded continuously on a strip-chart and digitally every 1–2 s. The average low-altitude flight velocity of 490 km hr^{-1} coupled with the 1–2 s sampling interval gave observations with an average spacing of ~230 m. Because the shortest wavelength of crustal anomalies resolvable at the sea surface is about 3 km (Parker 1974), anomalies due to crustal and shallow mantle sources are highly oversampled in our raw data. We also monitored time-dependent behaviour of the magnetic field with a stationary magnetometer located on Diego Garcia. The ground-based data (Fig. 4) permitted the assessment of the magnitude of time variations such as the daily variation and sudden impulses associated with geomagnetic storms (Courtillot & Le Mouel 1988; Joselyn & Tsurutani 1990). The observed time variations were far too slow to affect our analysis of anomalies due to crustal and shallow mantle sources.

Basic reduction of the aeromagnetic data

The magnetic-field intensity observations were merged with navigation positions determined from Omega, which is a

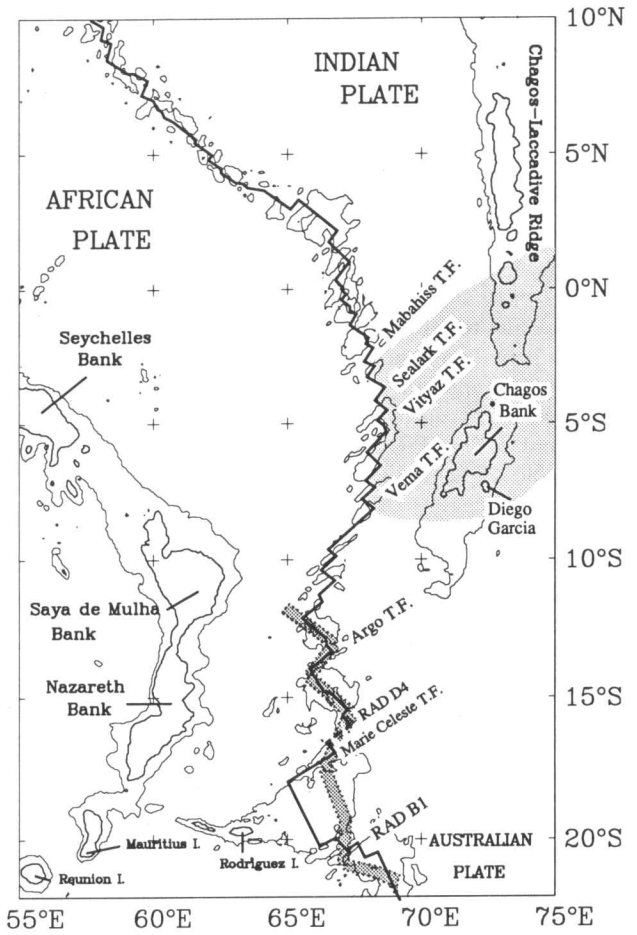

Figure 3. Locations of transform faults and other features discussed in the text. The shading along the ridge south of 10°S shows the extent of GLORIA long-range side-scan sonar mapping of the ridge in 1987 (Parson *et al.* 1993).

long-range marine radio-navigation system maintained by the US Government (see, e.g. Telford *et al.* 1976). We also determined locations from two on-board Global Positioning System (GPS) receivers. For the eight flights with overlapping Omega and GPS navigation, we compared 221 699 estimates of locations and found a mean difference of 1.8 ± 1.1 km between the Omega and GPS coordinates and a most frequent difference between 1 and 1.25 km. Omega navigation was available continuously for all the flights, but GPS could not be used for some flights because of instrument failure. At best, GPS was available only during the middle 6 hr of a flight because there were too few satellites in the sky for reliable navigation during the remaining 18 hr of the day. Thus, we chose to reduce the data using the Omega navigation. When GPS was working reliably, which was about half the flight time, the differences between Omega and GPS navigation suggest that the Omega navigation differs from the true location with a 2-D standard deviation of about 2.0 km, corresponding to a 1-D standard deviation of 1.4 km (see, eqs (12) and (14) of Cox & Gordon 1984). If errors in GPS navigation were not negligible relative to those in Omega, then the estimated errors of the Omega navigation are smaller than these values.

Preliminary residual magnetic-field intensities were calculated by subtracting the ambient magnetic-field intensities from the observed total field intensities. The ambient magnetic-field intensity was computed from the 1980 International Geomagnetic Reference Field (IGRF) projected forward to the time of the flight. During the flights, we occasionally observed impulsive high-frequency (~0.1–1 Hz) noise that apparently was caused by poor grounding of the magnetometer. Much of this noise, which constituted about ~1 per cent of the data from all flights, but as much as ~2 per cent of the observations from some flights, was removed by hand-editing. The rest of the noise was removed by filtering out high wavenumbers, as is further discussed below. Because its wavelength is so different from the crustal signal, this type of noise was not hard to identify and remove from the data.

We removed least-squares estimates of means and straight lines, which contain no information about anomalies produced by sea-floor spreading, from all aeromagnetic profiles. Each profile was then interpolated to an even interval using a cubic spline algorithm. Short wavelengths were filtered from all 57 aeromagnetic flight segments. On most (40) aeromagnetic profiles, i.e. those with noise bursts as described above, and on four ship segments (*Wilkes 728, Wilkes 821, Charcot 1ER* and *Charcot 2EME*), we removed the short wavelengths with a cosine-cubed half taper from unity at 3 km wavelength to zero at 2.25 km wavelength. For the remaining 17 aeromagnetic profiles, wavelengths less than 1 km were filtered with a taper that decreased from unity at 1 km wavelength to zero at 0.75 km wavelength. No bandpass filtering was applied to the other ship profiles that we analysed.

Figures 5 and 6 illustrate the effect of the filtering for two profiles collected on 1990 May 4. The profile that crosses the ridge at 1.5°S is the profile most affected by this type of noise and has high-wavenumber, high-amplitude noise along ~300–450 km of the profile between anomaly 3 on either side of the ridge (Figs 5a and b). Filtering of this noisy profile with a short wavelength cut-off (i.e. tapered between 2.25 and 3.0 km) eliminates nearly all this noise; after the profile is phase shifted to the pole, the resultant profile is easily correlated (see uppermost profile in Fig. 8b). The second profile, which was collected ~90 min after the first profile and crosses the ridge ~20 km south of it, is typical of our data and exhibits much less high-wavenumber noise. The mean absolute difference between the filtered profile and a profile that has only had the mean and best-fitting straight line removed (Figs 6a and b) is only 1.3 nanoTeslas for the 3333 observations along this track (including along-track observations outside of the track segments shown in Fig. 6(a)). In contrast, the noisy profile has an average absolute difference of 6.8 nT for the 2599 along-track field measurements.

PLATE MOTION DATA

Spreading rates

Phase shifting

Each magnetic profile, both aeromagnetic and ship-board, was phase shifted to reduce it to the pole (Blakely & Cox

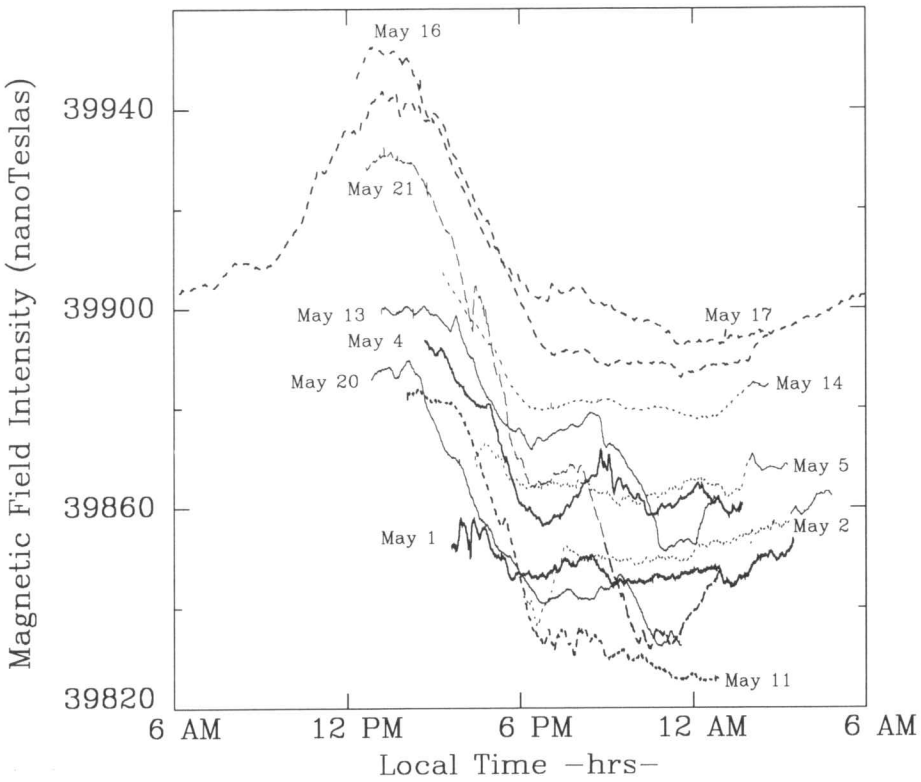

Figure 4. Magnetic field intensities observed from a magnetometer located at Diego Garcia Naval Air Base, Indian Ocean, 1990 May 1 to May 21. The intensity of the ambient field peaked daily at about 1:30 pm when the sun was near the zenith. The magnitude of the diurnal variation was typically 50 nT. The maximum field variation, which was 100 nT, occurred on May 21.

1972; Schouten & McCamy 1972). For simple models of sea-floor magnetization with constant direction of magnetization (except for reversals of polarity) and vertical boundaries between rectangular prisms of sea-floor of opposing polarity, anomaly skewness is determined by the strike of the magnetic lineation, the inclination and declination of the present magnetic field (which we calculate from the IGRF), and the inclination and declination of the remanent magnetization of the sea-floor (which we calculate assuming an axial geocentric dipolar palaeomagnetic field). The Central Indian Ridge and Carlsberg Ridge have a large along-ridge gradient in anomaly skewness (Fig. 7). Ignoring the direction of travel along a profile, profiles crossing the ridge in the study area span the complete range of possible skewnesses from symmetric (near 25°S) through anti-symmetric to inverted (near 3°N) with many asymmetric profiles in between. The large along-ridge gradient in the skewness of any single anomaly within the study area adds a level of complexity that slows the analysis and increases the chance of correlating anomalies erroneously. To simplify the analysis, we reduced each profile to the pole, i.e. we phase shifted each profile by an angle determined from the effective inclinations of the present field and remanent magnetization (assuming an axial geocentric dipole field) corresponding to the point where the profile crossed the spreading centre. This simple adjustment produced profiles that appear satisfactorily deskewed (Figs 8a–e). The phase-shifted profiles are more easily compared with one another and with a common set of synthetic magnetic anomalies, and contain the same spreading rate information contained in the original data.

Rate determination method

Several more steps are required to estimate the 3.0 Myr average spreading rate for each profile that crosses anomaly 2A (3.0 Ma) on both sides of the ridge. Each profile was projected onto the ridge-normal direction, which has little effect on most of the aeromagnetic profiles, which are within 5° of the ridge-normal direction. Each profile was compared with synthetic magnetic profiles generated at increments of 1 mm yr^{-1}. For two ridge segments where no single profile gave a spreading rate, multiple profiles were used to estimate the spreading rate. We compiled and correlated all the aeromagnetic and shipboard magnetic profiles on large-scale maps to ensure that our correlations of anomaly 2A for individual profiles are consistent with our correlations of nearby anomalies.

Rate results

Along the Central Indian and Carlsberg ridges, 33 rates were determined solely from our new aeromagnetic profiles; these 33 profiles are shown in Figs 8(a)–(e). Of the 33 new aeromagnetic rates, seven were determined from the closely spaced profiles that crossed the ridge segments flanking the Vema fracture zone at 9°S, and 26 were determined from the long fracture-zone parallel profiles. Twenty-two rates

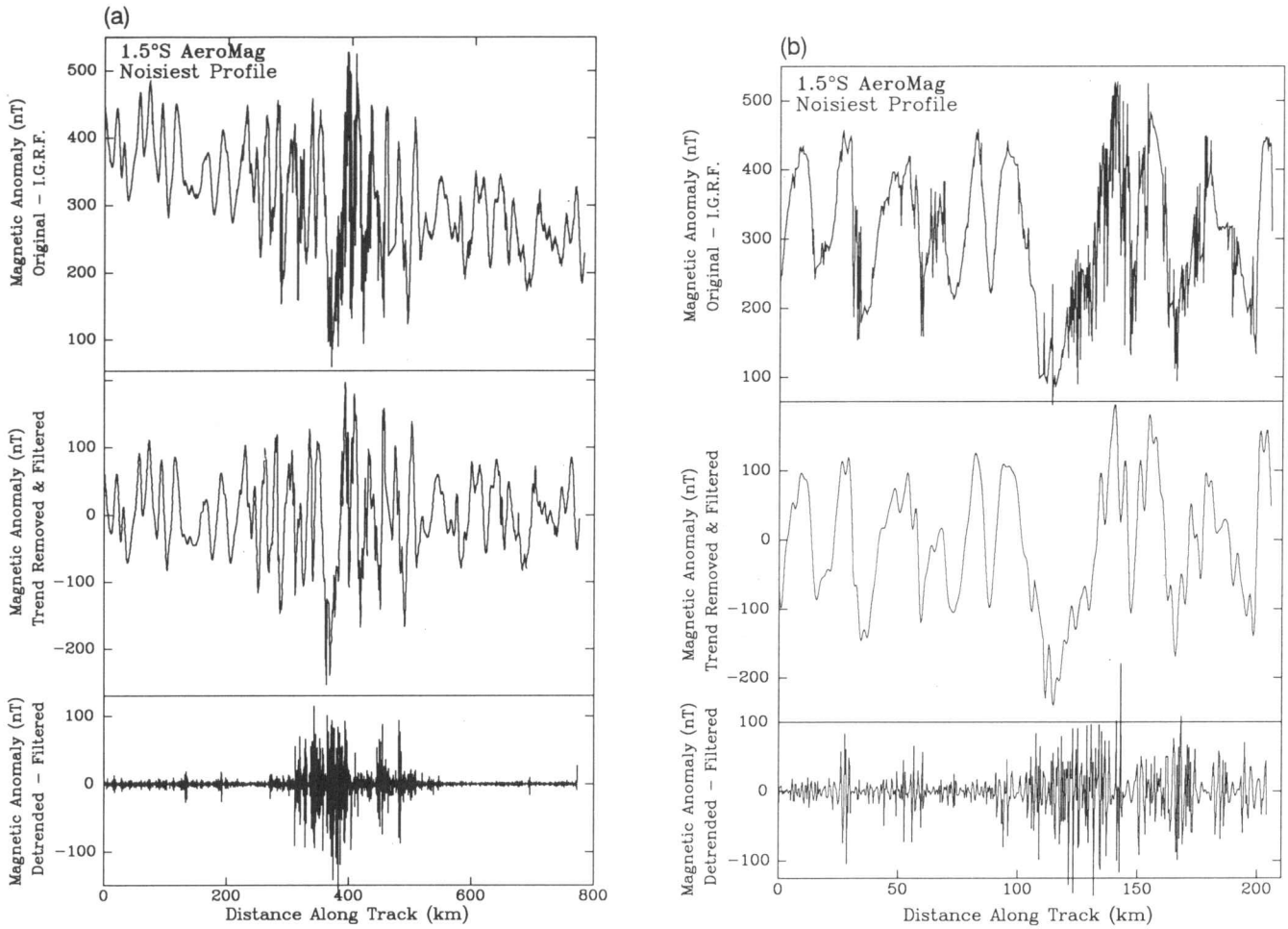

Figure 5. Effect of filtering our noisiest aeromagnetic profile, which crosses the ridge at 1.5°S. (a) The entire profile; (b) the near-ridge portion of the profile. In both parts, the upper profile is the original observed field intensity minus the field computed from the 1980 IGRF projected forward to 1990. (Use of the more recent 1990 IGRF considerably reduces the magnitude of the mean value of the residual anomaly.) The data were further reduced by removing the mean and best-fit straight line, and filtering to remove wavelengths of less than 3 km (middle profile). The lowest profile is the difference between the profile before and after short wavelengths were removed.

were determined from only shipboard data and one rate was determined from a Project Magnet profile. Two additional rates, discussed below, were determined from a combination of aeromagnetic and shipboard data. The spreading rate uncertainties that we assigned depended on several factors, including the strike of the profile relative to the ridge-normal direction and how well the observed anomaly shapes and sequence matched those for the synthetic profiles. Among the 33 rates determined only from our new aeromagnetic data, 22 were assigned standard errors of 1 mm yr^{-1}, nine were assigned errors of 2 mm yr^{-1}, and two were assigned errors of 3 mm yr^{-1}.

In contrast, among the 22 rates determined only from shipboard data, one was assigned an error of 1 mm yr^{-1}, three were assigned errors of 2 mm yr^{-1}, 11 were assigned errors of 3 mm yr^{-1}, six were assigned errors of 4 mm yr^{-1}, and one was assigned an error of 5 mm yr^{-1}. The new aeromagnetic data were assigned smaller errors than the shipboard data for several reasons: (1) the relevant portions of the new aeromagnetic profiles cross fracture zones in few places, which is a problem that plagues the interpretation of many of the shipboard profiles. (2) Because the new profiles are also nearly perpendicular to ridge segments, the error introduced in projecting the profile onto the ridge-normal direction is negligible for the new aeromagnetic profiles, but is substantial for many of the shipboard data. (3) The archived digital data available to us for some of the shipboard profiles, especially older profiles, are sparsely sampled and therefore spreading rates are less easily, and less unambiguously, resolved. (4) The navigation for some of the older shipboard data may be poor, especially for cruises before satellite navigation. An *a posteriori* analysis of normalized residuals indicated that the much smaller errors that we assign to the aeromagnetic data are in approximately correct proportion to those we assign to the shipboard data.

We compiled and analysed shipboard magnetic profiles to supplement the aeromagnetic data. A search of the National Geophysical Data Center (NGDC) and Lamont–Doherty Geobase archives provided over 100 cruises that crossed the study area. In several cases we were able to obtain archived data for cruises for which we only had published figures to

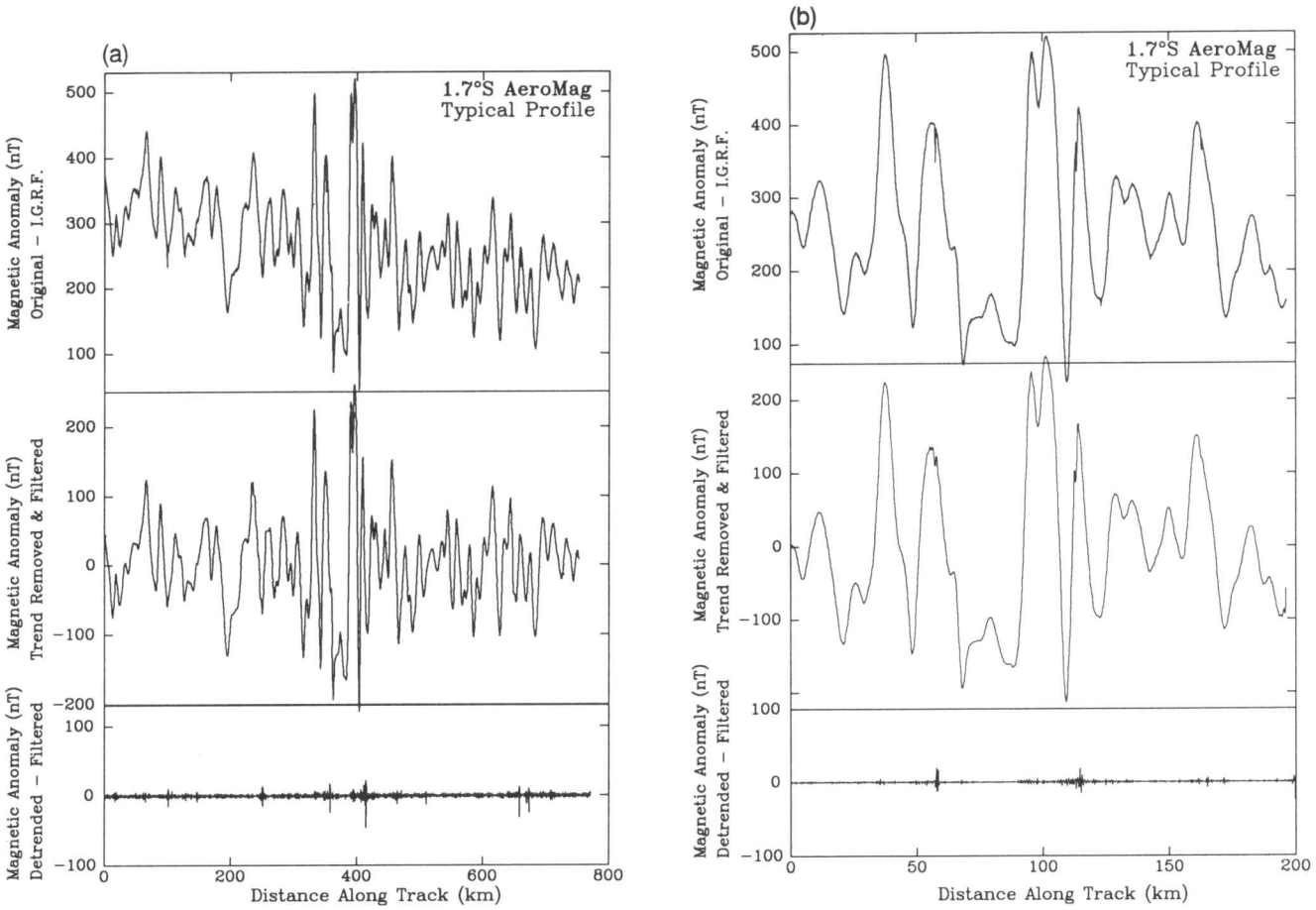

Figure 6. Effect of filtering a typical aeromagnetic profile, which crosses the ridge at 1.7°S. (a) The entire profile; (b) the near-ridge portion of the profile. In both parts, the upper profile is the original observed field intensity minus the field computed from the IGRF. The data were further reduced by removing the mean and best-fit straight line, and filtering to remove wavelengths of less than 3 km (middle profile). The lowest profile is the difference between the profile before and after short wavelengths were removed. The noise removed from this profile is about 10 times smaller than that removed from the noisiest profile (Fig. 5).

work with before (i.e. in DeMets *et al.* 1988, and Gordon & DeMets 1989). We were unable to obtain data in digital format from two recent Indian cruises (Chaubey *et al.* 1990); instead we digitized the magnetic profiles in the published figures. Other cruises have recently surveyed parts of the Central Indian Ridge (i.e. *Marion du Fresne* cruises 57 and 61), but the data are not yet available to us. Of the more than 100 cruises we examined, only 22 provided reliable spreading rates useful to this study. Anomaly locations identified from shipboard profiles agree with one another and with those from nearby airplane profiles typically within 5 km or less in the ridge-normal direction, even for cruises from the early 1960s before satellite navigation was used.

Our fresh look at the magnetic anomaly data available from archives, especially those from the western Carlsberg Ridge, led us to revise some spreading rates we had estimated before (DeMets *et al.* 1988; Gordon & DeMets 1989). Most revisions are a consequence of our improved knowledge of the locations and orientations of transform faults and ridge segments made possible from the interpretation of classified GEOSAT altimetry data (P. Vogt, unpublished map). All the maps in this paper incorporate the revised ridge-transform geometry interpreted from the classified GEOSAT data. In some locations along the ridge (e.g. at ~3.5°N and ~0.5°S), the ridge-transform geometry is poorly constrained by the GEOSAT data and the sparse bathymetric observations (Fig. 3). Because our aeromagnetic tracks were designed to avoid crossing the ridge near these locations, their largely unknown ridge-transform geometries have no effect on the results described below.

The most significant changes in estimated rates along the Carlsberg Ridge are the following.

(1) Various rates were changed by 1–3 mm yr^{-1}, in most cases because of a revision to our estimate of the strike of the ridge (Table 1). For example, we now estimate the strike of ridge segments along the western Carlsberg Ridge (59°E–66°E) to be N54°–55°W (P. Vogt, unpublished map), whereas we assumed a strike of N50°W in our prior work.

(2) We omitted the two westernmost rates that we had used before because none of the correlations for these profiles was very convincing.

(3) We omitted rates near 60.2°E from two of the three *Vema* 19–10 ridge crossings because we now believe that these two profiles cross a fracture zone or non-transform offset before reaching anomaly 2A on both sides of the ridge.

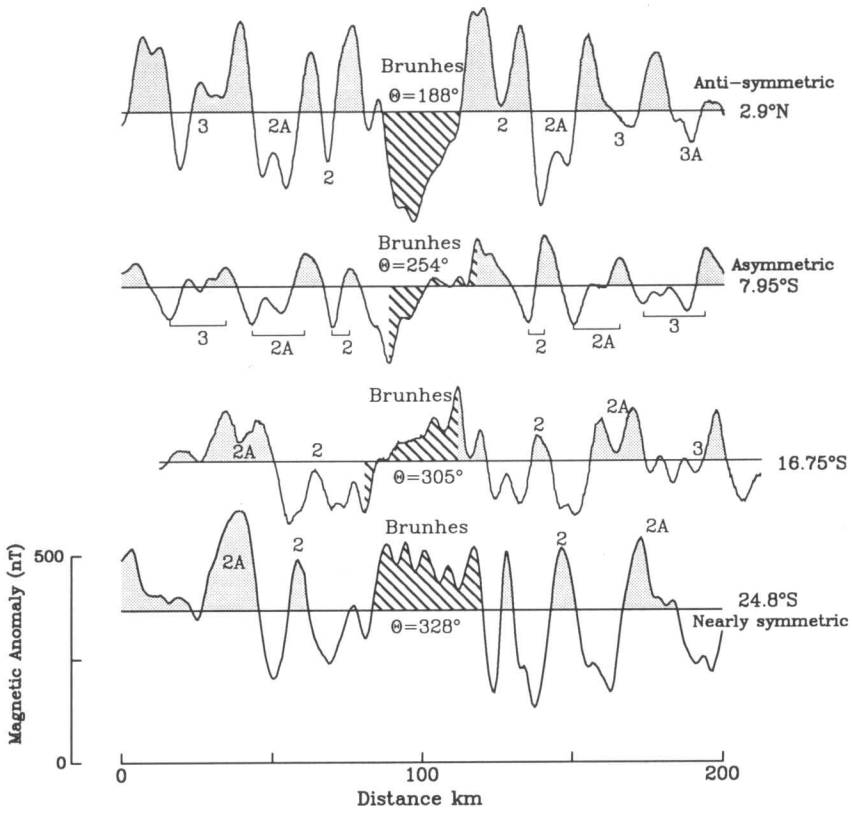

Figure 7. Four magnetic profiles that cross the Carlsberg and Central Indian ridges between 3°N and 25°S. The upper three profiles are new aeromagnetic data; the lowest profile is from cruise *Atlantis II* 9306. The Brunhes central anomaly (hachured) illustrates the large range in observed anomaly skewness θ. Anomalies 2 and 2A also show the anti-symmetric (180°S), asymmetric (270°) and nearly symmetric (330°) shapes exhibited by the Brunhes anomaly.

(4) We omitted the rate near 61.66°E from the Indomed 04 cruise because the profile crosses a fracture zone south-west of the ridge before reaching anomaly 2A.

(5) We omitted the rate near 62.2°E from Project Magnet profile 506 because it crosses a fracture zone south-west of the ridge before reaching anomaly 2A.

(6) We added one rate from a profile, *Conrad* 17-07, which had been unavailable to us before.

(7) We omitted the four rates between 1.5°N and 2.9°S along the southernmost Carlsberg Ridge (and northernmost Central Indian Ridge). These anomaly profiles give poorly constrained spreading rates, which were reflected in the very high uncertainties we had assigned to them. These data are now superseded by rates from the new aeromagnetic data.

The average rate and rate gradient along the Carlsberg Ridge from the new shipboard rates are not very different from those of our prior data set.

The most significant changes along the Central Indian Ridge are the following.

(1) We omitted the rate at 12.4°S from *Chain* 99-5 because it crosses a fracture zone south-west of the ridge before reaching anomaly 2A and may also cross a fracture zone north-east of the ridge.

(2) We omitted the rate at 12.8°S from the Circe 6 cruise because the correlation now seems unconvincing and we now have better data available from the new aeromagnetic profiles.

(3) We changed the rate for the *Conrad* 14-02 profile (wrongly labelled as *Conrad* 14-12 in Table 3 of DeMets *et al.* 1990) from a previous value of $37 \pm 10\,\mathrm{mm\,yr^{-1}}$ to a faster $40 \pm 5\,\mathrm{mm\,yr^{-1}}$. Two new aeromagnetic profiles immediately north-west of this previously isolated ship track showed that our earlier correlation of anomaly 2A was incorrect.

(4) We added a rate at 19.6°S determined by projecting three partial shipboard profiles (Circe 07, *Conrad* 17-06, and *Chain* 99-5) onto the ridge-normal direction and by correlating the resulting composite profile.

(5) We added a new rate at 22.5°S from a *Charcot* 2EME profile that was previously unavailable to us.

(6) We omitted the rate at 24.4°S from the Circe 7 cruise (but wrongly labelled 'Indomed-6' in Table 3 of DeMets *et al.* (1990) because we concur with Mitchell (1991) that the anomaly correlations for this profile are unreliable. Although the anomaly positions north-east of the ridge agree well with those of nearby more recent cruises, the anomaly positions south-west of the spreading axis are systematically offset by ~10 km from those interpreted from more recent, presumably better navigated, cruises. This suggests that the Circe 7 profile either crosses a small-offset fracture zone, or that the navigation has a problem that causes apparent stretching along the profile.

(7) Two rates across ridge segments located from 12°S to 15°S were determined from a combination of aeromagnetic and shipboard profiles.

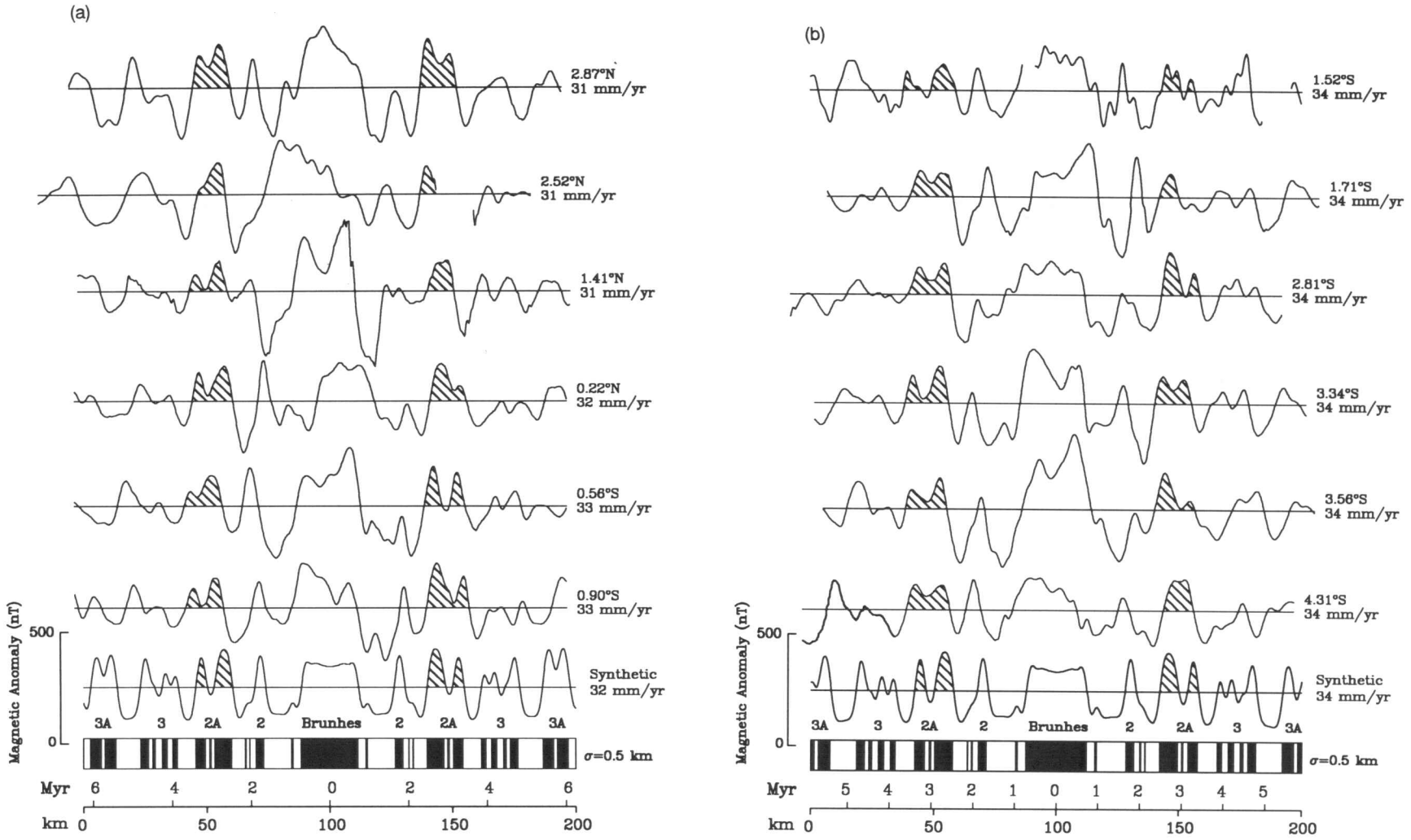

Figure 8. Thirty-three new ridge-normal aeromagnetic profiles crossing the Carlsberg and Central Indian ridges between 3°N and 18.5°S (Figs 1 and 2). Each profile has had the best-fitting mean and straight-line removed, has been interpolated and filtered to remove wavelengths shorter than 1–3 km, and has been reduced (i.e. phase shifted) to the pole. The spreading rate that best fits each profile appears to the right of each profile. Synthetic magnetic profiles, calculated with a $1-\sigma$ transition width of 0.5 km, are shown at the bottom of each figure. For some profiles where anomaly 2A is poorly formed (e.g. 6.38°S), the best spreading rate was determined from the optimal fit of a synthetic profile to the anomalies 2, 2A and 3 waveforms. Larger uncertainties were assigned to such spreading rates.

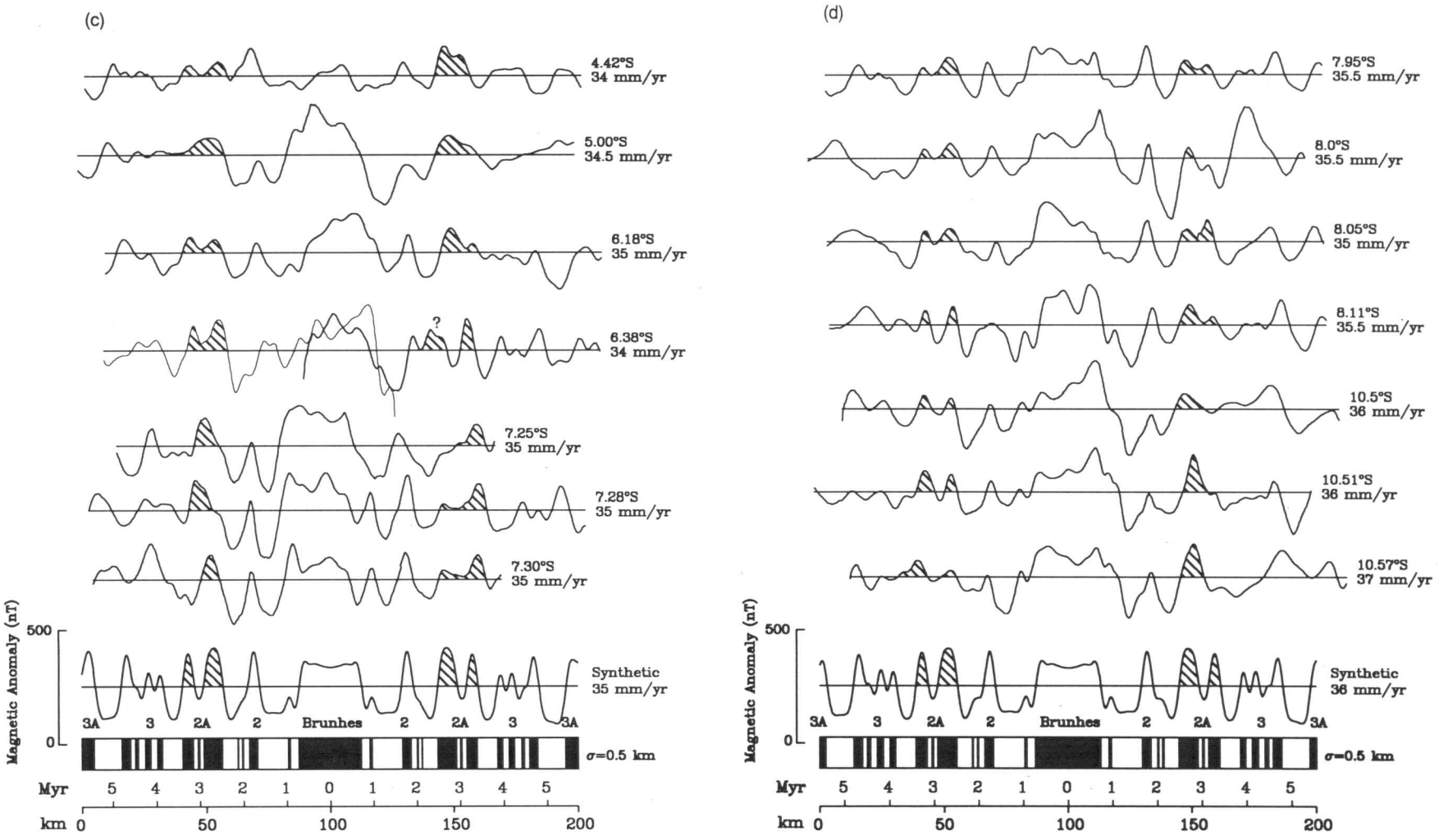

Figure 8. (*Continued.*)

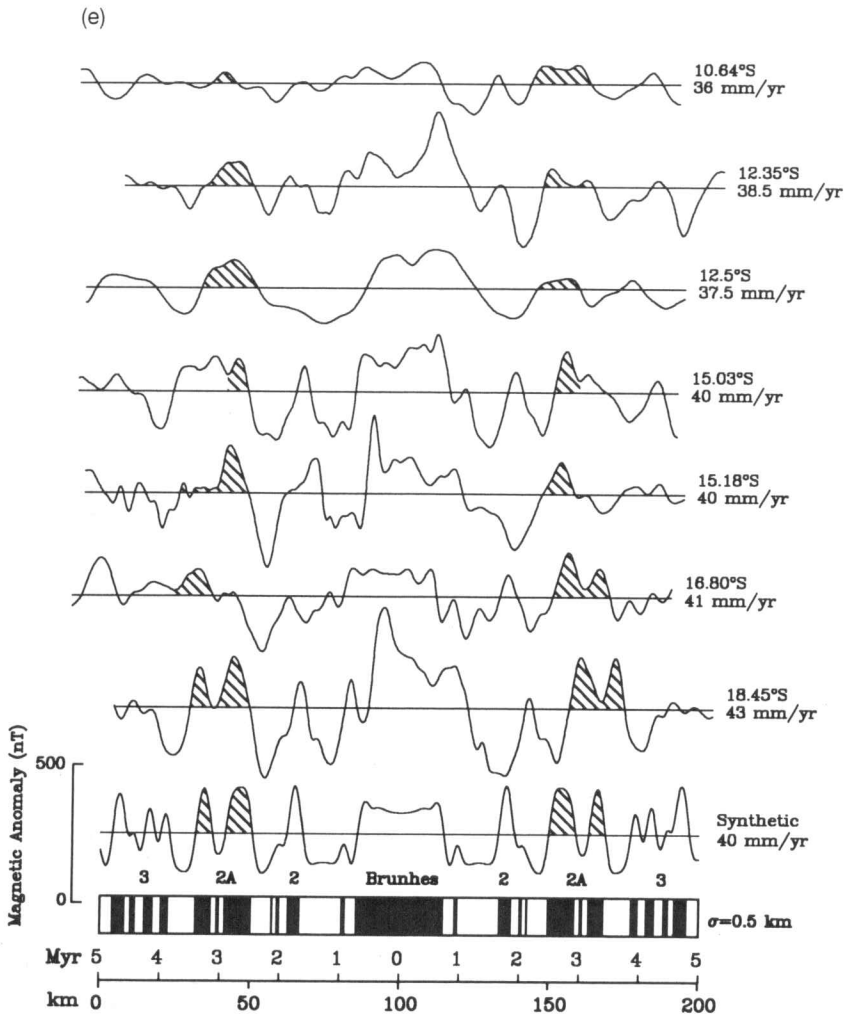

Figure 8. (*Continued.*)

(8) Two rates were determined from shipboard data located from 18.5°S to 22°S (Fig. 9) as follows.

Magnetic profiles from ten cruises, many of which became available after the last published compilation of data from this region (Fisher, Sclater & Mckenzie 1971), are shown in Fig. 9. Data from cruises *Sagar Kanya* 16 and *Sagar Kanya* 20, which consist of seven NE-trending tracks (Chaubey *et al.* 1990), are the main source of new information about anomalies in this area. Our interpretation of the earthquake epicentres, centroid-moment tensor focal mechanisms and locations, magnetic data and bathymetric data in this region (Fig. 10) is consistent with the interpretation of Chaubey *et al.* (1990) that a previously unrecognized transform fault offsets the ridge at 20.25°S.

Transform fault azimuths

As in our prior papers, we require not only that a transform fault be well surveyed, but also that the transform have an offset of at least 35 km. Many shorter transform faults, notably the Kurchatov transform fault (Searle & Laughton 1977), have been shown to fail to parallel plate motion. Thus, we excluded azimuths from transform faults with ridge offsets less than 35 km. Transforms with longer offsets were generally included if they have been adequately surveyed. In prior papers on plate motion, transform azimuths were estimated subjectively. Herein we use a new procedure for objectively estimating the uncertainties in transform fault azimuths. First, the length of the portion of the transform fault having sonar coverage is determined either from bathymetric charts that show the extent of ship-track coverage, or, when available, from side-scan sonar images. For transform faults that have been mapped in enough detail to locate the transform fault zone (i.e. the zone of active strike-slip faulting within the transform valley) (Fox & Gallo 1986; Searle 1986), the width of this zone is estimated. If the transform tectonized zone (i.e. the zone in which all strike-slip motion over time has been accommodated), but not the transform fault zone, has been identified and mapped, we estimate the width of the former. Otherwise, the width of the transform valley is estimated. A maximum uncertainty θ is then estimated by taking the inverse tangent of the width divided by the length having sonar coverage. We assume that the best estimate of the transform-fault azimuth lies within the centre of this

Table 1. Carlsberg and Central Indian Ridge data.

Lat. °N	Lon. °E	Datum	σ	Model	ι	Ridge Strike	Source
Africa-India: Spreading Rates							
8.01	59.21	25	3	25.2	0.064	s55e	NGDC *HMS Owen* 3
7.25	59.60	27	3	25.7	0.058	s55e	NGDC *USNS Wilkes* 821
7.07	59.88	26	3	25.9	0.055	s54e	NGDC *R/V Vema* 19-10
6.80	60.00	27	3	26.1	0.053	s54e	Project Magnet 505
5.43	61.66	29	3	27.5	0.039	s54e	NGDC *R/V Vema* 34-08
5.27	61.69	27	4	27.6	0.022	s54e	NGDC *HMS Owen* 6
4.24	62.64	28	3	28.5	0.031	s54e	NGDC *HMS Owen* 6
3.74	63.80	31	3	29.3	0.025	s54e	NGDC *R/V Conrad* 17-07
3.72	63.78	32	4	29.3	0.014	s54e	NGDC *HMS Owen* 1
2.87	66.00	31	1	30.8	0.145	s54e	1990 aeromagnetic
2.52	66.42	31	2	31.1	0.033	s54e	1990 aeromagnetic
1.41	66.88	31	1	31.7	0.102	s53e	1990 aeromagnetic
0.22	67.00	32	1	32.2	0.081	s51e	1990 aeromagnetic
-0.56	67.19	33	1	32.5	0.071	s51e	1990 aeromagnetic
-0.90	67.45	33	1	32.8	0.067	s51e	1990 aeromagnetic
-1.52	67.50	34	3	33.0	0.007	s51e	1990 aeromagnetic
-1.71	67.80	34	2	33.2	0.015	s51e	1990 aeromagnetic
-2.81	68.06	34	1	33.7	0.056	s51e	1990 aeromagnetic
-3.34	68.04	34	1	33.9	0.054	s50e	1990 aeromagnetic
-3.56	68.45	34	1	34.2	0.055	s50e	1990 aeromagnetic
-4.31	68.46	34	1	34.4	0.057	s50e	1990 aeromagnetic
-4.42	68.58	34	1	34.5	0.058	s50e	1990 aeromagnetic
-5.00	68.44	34.5	2	34.7	0.015	s49e	1990 aeromagnetic
-6.18	68.07	35	1	34.9	0.067	s46e	1990 aeromagnetic
-6.38	68.28	34	2	35.0	0.018	s45e	1990 aeromagnetic
-7.25	68.04	35	2	35.1	0.022	s43e	1990 aeromagnetic
-7.28	68.05	35	1	35.1	0.088	s43e	1990 aeromagnetic
-7.30	68.08	35	1	35.1	0.088	s43e	1990 aeromagnetic
-7.95	67.95	35.5	1	35.2	0.106	s41e	1990 aeromagnetic
-8.00	68.00	35.5	1	35.2	0.107	s41e	1990 aeromagnetic
-8.05	68.04	35	1	35.3	0.109	s41e	1990 aeromagnetic
-8.11	68.10	35.5	1	35.3	0.111	s41e	1990 aeromagnetic
Africa-India: Transform Azimuths							
11.00	57.50	30.0	3.7	29.4	0.281		Laughton *et al.* (1970)
-5.50	68.50	43.0	4.2	39.3	0.120		Kanaev (1975)
Africa-India: Slip Vectors							
11.74	57.71	28.0	15	28.2	0.017		CMT 04.20.80
11.28	57.49	29.0	15	29.0	0.017		CMT 04.8.83
11.28	57.25	29.0	15	29.2	0.017		CMT 05.30.78
10.76	57.00	36.0	15	30.2	0.017		CMT 09.17.86
-1.00	67.45	34.0	15	36.5	0.009		CMT 05.5.85
-1.09	67.44	37.0	20	36.6	0.005		CMT 09.6.89
-1.40	67.77	35.0	15	36.6	0.009		CMT 05.9.85
-1.41	67.75	37.0	15	36.7	0.009		CMT 07.16.81
-3.00	68.08	38.0	20	37.7	0.005		CMT 03.17.79
-5.37	68.68	44.0	25	39.0	0.003		CMT 03.06.88
-5.47	68.64	51.0	25	39.2	0.003		CMT 04.28.87
Australia-Africa: Spreading Rates							
-10.50	66.40	36	2	35.7	0.032	s39e	1990 aeromagnetic
-10.51	66.39	36	1	35.7	0.129	s39e	1990 aeromagnetic
-10.57	66.42	37	2	35.7	0.032	s39e	1990 aeromagnetic
-10.64	66.45	36	2	35.8	0.032	s39e	1990 aeromagnetic
-12.00	66.00	37	4	36.7	0.008	s38e	Fisher *et al.* (1971)
-12.35	65.71	38.5	2	36.8	0.031	s38e	1990 aeromagnetic
-12.50	65.84	37.5	1	37.1	0.121	s38e	1990 aeromagnetic
-14.11	65.93	39	2	38.7	0.028	s35e	1990 aeromagnetic + ship-board
-14.28	66.07	38	4	38.9	0.007	s35e	1990 aeromagnetic + ship-board
-15.03	66.81	40	1	40.0	0.109	s35e	1990 aeromagnetic
-15.18	67.00	40	3	40.3	0.012	s35e	1990 aeromagnetic
-15.40	67.20	40	5	40.6	0.004	s35e	NGDC *R/V Conrad* 14-02
-16.80	66.67	41	1	41.6	0.106	s30e	1990 aeromagnetic
-18.47	65.35	43	1	42.4	0.104	s30e	1990 aeromagnetic
-18.93	65.87	42	3	43.1	0.011	s30e	NGDC Antipodes 5
-19.60	66.10	44	3	43.7	0.011	s30e	NGDC ship-board composite
-20.20	66.90	44	2	44.7	0.026	s30e	NGDC ship-board & *R/V Sagar Kanya*
-20.30	67.70	46	2	45.2	0.026	s30e	NGDC ship-board & *R/V Sagar Kanya*
-21.39	68.65	45	3	46.6	0.012	s30e	NGDC *R/V Vema* 18-11
-21.57	69.00	45	4	46.9	0.007	s30e	NGDC Dodo 8
-21.95	68.96	47	3	47.2	0.012	s30e	NGDC *R/V Vema* 20-9
-22.51	69.26	48	1	47.8	0.108	s30e	NGDC *R/V J. Charcot* 84-2EME
-23.82	69.66	51	4	49.0	0.007	s30e	NGDC *R/V Atlantis II* 9306
-24.50	69.84	49.5	2	49.7	0.029	s30e	NGDC *R/V Atlantis II* 9306
-24.77	69.80	49	3	49.9	0.013	s30e	NGDC *R/V Atlantis II* 9306
-24.94	69.88	49	4	50.0	0.007	s30e	NGDC *R/V Monsoon* 4a
Australia-Africa: Transform Azimuths							
-9.00	67.30	50.0	1.6	51.6	0.361		Engel and Fisher (1975)
-13.75	66.25	60.0	1.7	58.0	0.257		Parson *et al.* (1993)
-16.25	67.00	62.0	2.4	58.8	0.113		Parson *et al.* (1993)
-17.50	66.00	60.0	3.0	61.2	0.070		Parson *et al.* (1993)
-20.25	67.25	65.0	3.8	61.2	0.038		Parson *et al.* (1993)
Australia-Africa: Slip Vectors							
-8.81	67.41	47.0	20	51.2	0.002		CMT 07.12.89
-8.94	67.67	40.0	20	51.0	0.002		CMT 10.12.78
-9.22	67.09	50.0	20	52.2	0.002		CMT 01.20.88
-9.32	67.18	48.0	15	52.2	0.004		CMT 08.19.81
-9.42	66.89	48.0	20	52.8	0.002		CMT 02.03.88
-12.11	65.40	52.0	15	57.9	0.004		CMT 10.27.84
-13.45	66.06	52.0	15	58.0	0.003		CMT 05.14.89
-13.61	65.90	55.0	20	58.4	0.002		CMT 08.14.78
-13.72	66.29	48.0	20	57.9	0.002		CMT 10.15.82
-14.03	66.20	58.0	25	58.3	0.001		CMT 11.08.90
-14.04	65.93	54.0	15	58.7	0.003		CMT 06.11.84
-16.58	66.77	57.0	15	59.4	0.003		CMT 12.01.85
-17.20	66.79	56.0	15	59.8	0.003		CMT 04.14.80
-17.21	66.67	58.0	15	60.0	0.003		CMT 11.07.81
-17.32	65.97	60.0	15	61.1	0.003		CMT 11.05.91
-17.33	66.64	56.0	25	60.2	0.001		CMT 03.07.90
-17.41	66.62	54.0	20	60.2	0.002		CMT 05.04.88
-17.55	66.04	57.0	20	61.2	0.002		CMT 08.22.79
-17.79	65.82	57.0	15	61.7	0.003		CMT 08.12.83
-17.97	65.36	58.0	20	62.5	0.002		CMT 11.29.80
-18.03	65.39	58.0	15	62.5	0.003		CMT 08.11.88
-18.07	65.62	57.0	15	62.2	0.003		CMT 09.17.84
-20.03	66.39	63.0	20	62.3	0.001		CMT 06.07.90
-20.30	67.12	55.0	25	61.4	0.001		CMT 04.29.89
-20.45	66.90	66.0	15	61.8	0.002		CMT 06.21.86
-20.43	67.92	65.0	20	60.4	0.001		CMT 09.23.83
-20.62	68.05	62.0	25	60.3	0.001		CMT 05.27.91
-23.01	69.26	54.0	25	60.1	0.001		CMT 09.24.78
-23.04	69.07	61.0	25	60.4	0.001		CMT 08.21.85

The angular velocities used to fit these data are the five-plate closure-enforced angular velocities in Table 3. "ι" is the data importance, a measure of the information content of a datum (Minster *et al.*, 1974). "σ" is the standard error assigned to a datum. Rates and their standard errors are listed in millimeters per year. All rates were determined using the time scale of Harland *et al.* (1982). Rates determined from data we obtained from the National Geophysical Data Center data are referenced NGDC. Azimuths and their standard errors are listed in degrees clockwise from north. Slip vectors referenced as CMT are determined from Harvard centroid-moment tensor solutions; see Dziewonski *et al.* (1990) for a complete listing of references to centroid moment tensor solutions for earthquakes that occurred prior to 1/01/90, and Dziewonski *et al.* (1991abc, 1992bc) for earthquakes that occurred later than 12/31/89.

maximum uncertainty range. If the transform has an equal probability of assuming any azimuth within its maximum uncertainty range, then the standard error is θ divided by $\sqrt{3}$, which is the estimate we use herein. If instead, the probability distribution is more concentrated near the centre of the tectonic domain, then the standard error would be narrower than we assume here.

Because so little of the Carlsberg and Central Indian ridges has been mapped with conventional sonar (i.e. precision depth recorders) or modern surveying systems, we re-examined near-ridge bathymetric, altimetric and magnetic data to determine the locations and (when possible) the strikes of transform faults between the Owen transform fault and the Rodriguez triple junction. From 2°N to 22°S, where we had access either to high-quality magnetic data or to charts determined from classified GEOSAT data, we have identified 21 offsets of the central anomaly or ridge crest that are long enough (i.e. exceeding 35 km) to suggest that they are transform faults. In contrast, the GEBCO

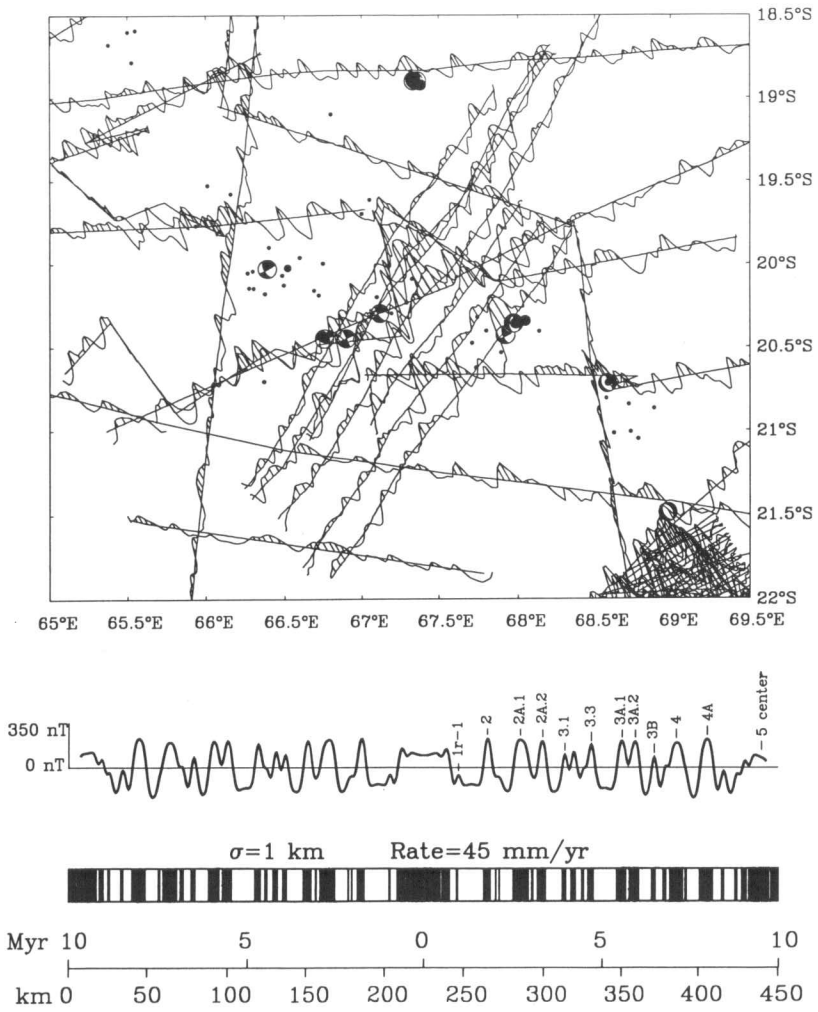

Figure 9. Upper: Magnetic anomalies (reduced to the pole), earthquake epicentres, and Harvard centroid-moment tensor focal mechanisms, 18.5°S–22°S, Central Indian Ridge. Shipboard magnetic profiles are from Antipodes 05, *Chain* 9905, Circes 07, *Conrad* 1706, Dodo 8, *Jean Charcot* 2EME, *Vema* 1811, *Vema* 2009, *Vema* 2903 and *Sagar Kanya* 16 and 20 cruises (Chaubey *et al.* 1990). Solid circles show epicentres of shallow (<50 km deep) earthquakes for 1963 January through 1989 March from the National Geophysical Data Center earthquake data file. The interpretation is given in Fig. 10. Lower: Synthetic magnetic profile drawn to same distance scale as the map in the upper portion of the figure. Spreading rate is a constant 45 mm yr^{-1}. The assumed reversal transition width (σ) is 1 km. Reversal nomenclature is adopted from Harland *et al.* (1982).

bathymetric compilations for the same area (Laughton 1975; Fisher *et al.* 1982) show only ~17 offsets exceeding 35 km. In addition to the 21 offsets that we believe are transform faults offsetting the ridge, the charts based on classified GEOSAT data indicate ~10 shorter offsets exceeding ~5 km. These may represent overlapping ridge segments or other deviations from axial linearity. Except for two poorly defined offsets near 1°S, these short offsets are located between 20°S and 12°S, and appear to correspond to short offsets of the ridge mapped by GLORIA side-scan sonar (Parson *et al.* 1993). Locations of ridge-axis normal-faulting earthquakes (e.g. from Huang & Solomon 1987 and centroid-moment tensor solutions) are consistent with our interpretation of the ridge-transform geometry. The charts based on classified GEOSAT data show evidence along the Carlsberg and Central Indian ridges for sea-floor fabric disturbed by propagating rift segments only from 20°S to 12°S.

Only 7 of the 21 offsets assumed to be transform faults are now well-enough surveyed to be useful for estimating the direction of plate motion (Table 2). The main improvement in the transform-fault azimuths relative to those we used before is the inclusion of azimuths estimated from a recent GLORIA survey of four transform faults: the Argo, the Marie Celeste, and two unnamed transform faults termed 'D4' and 'B1' (Parson *et al.* 1993). Only the Argo transform has sonar coverage along its entire length. GLORIA data along the Argo establish the maximum width of the transform tectonized zone as 5 km, and further indicate a lineament that may be the active strike-slip fault (Parson *et al.* 1993). Along RAD D4 (Ridge Axis Discontinuity D4), lineations in the transform-fault zone, which is 3–4 km wide, trend N62°E. We assumed a 4 km width for estimating the azimuthal uncertainty. GLORIA data along the Marie Celeste transform fault at 17.5°S resolved no narrow zone of recent strike-slip motion; we used the 15 km width of the transform valley to estimate the azimuthal uncertainty. GLORIA data cover only the north-eastern 65 km of the

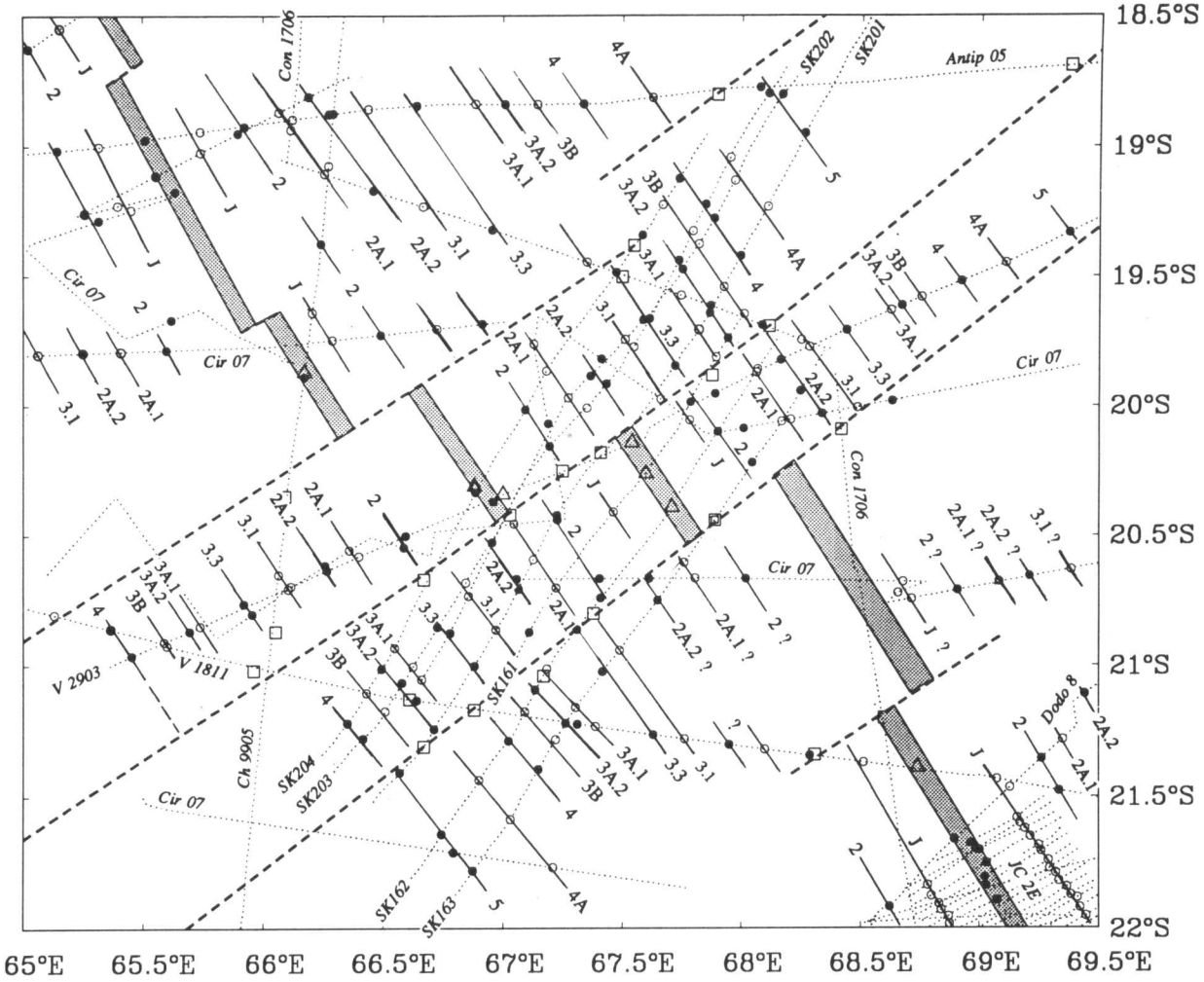

Figure 10. Interpretation of magnetic anomaly profiles shown in Fig. 9. Open and closed circles show anomaly correlations for the tie points shown on the synthetic magnetic profile in Fig. 9. Open triangles mark rift valley locations determined from bathymetry. Open squares mark shipboard crossings of fracture zones.

Table 2. Transform fault information.

Name	Lat. °N	Lon. °E	Strike °CW	Offset (km)	Surveyed Length (km)	Width (km)	θ	σ	Source
Owen	11.00	57.50	30.0	321	301	34	6.4	3.7	Laughton *et al.* (1970)
Vityaz	-5.50	68.50	43.0	130	39	5	7.3	4.2	Kanaev (1975)
Vema	-9.00	67.30	50.0	250	210	10	2.7	1.6	Engel and Fisher (1975)
Argo	-13.75	66.25	60.0	115	95	5	3.0	1.7	Parson *et al.* (1993)
RAD D4	-16.25	67.00	62.0	110	55	4	4.2	2.4	Parson *et al.* (1993)
Celeste	-17.50	66.00	60.0	186	166	15	5.2	3.0	Parson *et al.* (1993)
RAD B1	-20.25	67.25	65.0	67	27	3	6.3	3.8	Parson *et al.* (1993)

"Width" designates the width of the transform fault zone, if it is imaged, or the transform tectonised zone or valley if the transform fault zone is not detected. Transform valley widths, which are measured perpendicular to transform strike, represent the distance between the bases of the steep slopes that flank the valley. Valley widths typically vary along strike, thus, the widths given here are only approximate. θ is the maximum uncertainty in the transform fault strike and is given by $\tan^{-1}$(Width/Insonified Length). σ is the best estimate of the standard error, and is equal to θ divided by $\sqrt{3}$. The sparsely surveyed northeasternmost 40 km of the Vema transform fault does not contribute to the surveyed length. GLORIA mapping of the Celeste transform is limited to northeastern 65 km of the transform. The remaining 121 km of the transform fault has been surveyed by conventional sonar (Engel and Fisher, 1975).

transform fault, but conventional sonar profiles (Engel & Fisher 1975) cross the south-western portion and indicate a trend that agrees well with that estimated from the GLORIA data. GLORIA data along 27 km of the RAD B1 transform fault reveal no zone of active strike-slip motion, but show that the transform valley is narrow (~3 km), which limits the azimuth of slip with a maximum uncertainty of ~5°.

We estimated the azimuths of three other transform faults, the Owen, Vityaz and Vema transform faults, from bathymetric charts (Laughton, Whitmarsh & Jones 1970; Engel & Fisher 1975; Kanaev 1975; Fisher *et al.* 1982) while taking into account the data distribution indicated by ship tracks. We supplemented these data with magnetic, geoid and bathymetric profiles. Re-examination of bathymetric data led us to estimate transform-fault strikes for the Vema and Vityaz that are 2°–3° counter-clockwise of those we adopted before (DeMets *et al.* 1988, 1990), which had been simply carried over from the much earlier studies of Chase (1978) and Minster & Jordan (1978). Offsets of magnetic lineations determined from closely spaced aeromagnetic profiles over the Vema transform fault suggest a trend of N49°–50°E, in good agreement with that estimated from the bathymetry. The ±1.6° standard error estimated for the trend of the Vema transform fault, which has not been surveyed with modern side-scan or swath mapping systems, follows from a conservative 10 km estimate for the width of the transform valley along the 210 km long portion of the transform valley that is well surveyed by conventional sonar (Engel & Fisher 1975). The strike of the Owen transform fault is difficult to estimate. Its transform valley is wide, and conventional sonar data define no zone of recent strike-slip faulting. Thus the standard error (±3.7°) is large, although the offset of 320 km is also large, because the transform could lie anywhere within the unusually wide (34 km) transform valley.

Earthquake slip vectors

Slip vectors for earthquakes that occurred along transform faults were determined from 40 Harvard centroid-moment tensor solutions from 1977 to the end of 1991. Slip vectors were assigned a 15°, 20° or 25° standard error, respectively, if seismic moment was greater than or equal to 10^{25} dyne cm, between 10^{24} and 10^{25} dyne cm, or less than 10^{24} dyne cm.

ANALYSIS OF THE PLATE MOTION DATA

Herein we first test whether the data along the Carlsberg and Central Indian ridges can be acceptably fit by a model with a single Indo-Australian plate moving away from Africa, and we find that they cannot. Next, using data only along the Carlsberg and Central Indian ridges, we find the best estimate and confidence limits on the location of the intersection of the boundary between India and Australia with the Central Indian or Carlsberg ridge. Following an examination of the motion between India and Arabia, closure of the Africa–Arabia–India and Africa–Antarctica–Australia plate motion circuits are examined. These closure tests are used to place bounds on the rigidity of the plates. We conclude this section by estimating the motion between India and Australia.

Is India–Australia motion measurable?

To compare different models, we use the following measure of the goodness-of-fit of a model to the data:

$$\chi^2 = \sum_{i=1}^{N} \left[\frac{d_i^{\text{obs}} - d_i^{\text{pred}}}{\sigma_i} \right]^2 \quad (1)$$

where d_i^{pred} is the value of the ith datum predicted from a particular plate motion model, d_i^{obs} is its observed value, and σ_i is the standard error assigned to this observed datum. To determine whether the addition of a plate boundary between India and Australia reduces the misfit significantly, we use an F-ratio test based on the parameter

$$F_{4,N-7} = \frac{[\chi^2(3) - \chi^2(7)]/4}{\chi^2(7)/(N-7)} \quad (2)$$

where $\chi^2(3)$ is the value of summed squared normalized misfit for the best-fitting model with only three adjustable parameters (i.e. trying to fit all data along the Central Indian Ridge and Carlsberg Ridge by a single angular velocity), $\chi^2(7)$ is the value of this same summed misfit for the best-fitting model with seven adjustable parameters (three for the India–Africa angular velocity, three for the Australia–Africa angular velocity, and one for the latitude of the Africa–Australia–India triple junction), and N is the number of data (Gordon *et al.* 1990). We assume that this statistic is approximately F-distributed with 4 versus $N-7$ degrees of freedom. The value of F determined from observations can be compared with reference values from tables (e.g. Spiegel 1975) or computer subroutines (e.g. Press *et al.* 1986) for various significance levels for $F_{4,N-7}$. This procedure tests for statistically significant systematic differences between plate motion data north and south of any assumed intersection of the India–Australia plate boundary with the Central Indian or Carlsberg ridges. It can be interpreted as indicating significantly different motion only if systematic errors in the plate motion data can be neglected.

Systematic errors are those that do not decrease as the number of data increase. For example, if our estimated strikes of the Carlsberg Ridge are consistently a few degrees clockwise of the true strike, as is suggested by a recent Seabeam survey crossing the ridge in a few places (W. Plüger, pers. commun. 1994), then rates along the Carlsberg Ridge have a small error that would not decrease with increasing numbers of useful magnetic profiles across the ridge. Another small systematic error in rates is caused by sloping reversal boundaries within the crust and upper mantle and the finite widths of magnetic polarity transition; both cause outward displacement of magnetic anomalies away from the ridge axis (Atwater & Mudie 1973). Thus all estimates of spreading rates are slightly faster than the true rate, but the size of this small effect is poorly known. A demonstrated systematic error is the bias, which depends on the sense of offset, of 1°–5° in the azimuths of slip-vectors from focal mechanisms of strike-slip earthquakes along transform faults (Argus *et al.* 1989; DeMets 1993); results from azimuths of slip vectors thus have an error that cannot

be eliminated merely by increasing the number of data. This systematic error in slip vectors likely causes results we quote based on F-ratio tests to exaggerate significance levels and to give confidence limits that are too narrow. (On the other hand, we think we have probably systematically overestimated errors in spreading rates and this causes results based on chi-square tests to give significance levels that are understated and confidence limits that are too wide.) There are surely other significant systematic errors that we have not considered.

Using plate motion data determined mainly from analysis of magnetic profiles obtained from US national archives, we previously found a value for F of 44 for the best-fitting intersection (between 3°S and 6°S), which indicates that the probability of such an improvement in fit occurring by chance is only $\sim 2 \times 10^{-16}$ (Gordon *et al.* 1990). If instead we had assumed that we had accurately estimated the errors in the data, then a chi-square test, instead of an F-ratio test, would have been appropriate. In that case, we find that the difference in χ^2 between a model with a single Indo-Australian plate and a model divided at the best-fitting latitude is 19.5 with 4 degrees of freedom, which indicates that the probability of such an improvement in fit occurring by chance is $\sim 6 \times 10^{-4}$. Thus, differences between plate motion data north and south of ~5°S were statistically significantly resolvable from data only along the Central Indian and Carlsberg Ridges, irrespective of data along with other plate boundaries. Repeating this test with the new data, F is 108; the probability of such an improvement in fit occurring by chance is less than 10^{-34}. If we instead use a chi-square test, we find that the difference in χ^2 between a model with a single Indo-Australian plate and a model divided at the best-fitting latitude is 65.8 with 4 degrees of freedom, which indicates that the probability of such an improvement in fit occurring by chance is less than $\sim 2 \times 10^{-13}$. Thus, the plate motion data recording motion between India and Africa unambiguously and systematically differ from those recording motion between Australia and Africa.

To calibrate the strength of our conclusion of distinct Indian and Australian plates, we also applied this test to plate motion data along the Arctic and Mid-Atlantic ridges north of 20°N (Argus *et al.* 1989). The North American plate lies to the west of this ridge system, whereas the Eurasian and African plates lie to the east of this ridge system. Using the same method as that applied to the Central Indian Ridge and Carlsberg Ridge plate motion data, we searched for the best location of the Africa–Eurasia boundary along the Mid-Atlantic ridge and tested for its statistical significance. χ^2 reaches its lowest value of 10.08 at the Azores triple junction, in good agreement with abundant independent data that restrict the location of this triple junction. The value of F in an F-ratio test for the significance of this additional boundary is 83, less than the value of 108 determined from the test for the significance of separate Indian and Australian plates. Similarly, the value of the difference in χ^2 is 49.2, less than the value of 65.8 found above. Thus, the evidence for motion between distinct Indian and Australian plates is now comparable to, if not better than, that for another slowly slipping boundary between major plates. In fact, the maximum predicted speed across a (hypothetical) narrow boundary between Australia and India near the Central Indian Ridge (5.0 ± 2.2 mm yr^{-1}) is about the same (4.6 ± 1.4 mm yr^{-1}) as that between Africa and Eurasia near the Azores triple junction, and probably larger than that (2.8 ± 1.2 mm yr^{-1}) between the North and South American plates near the Mid-Atlantic Ridge. (These are 95 per cent confidence limits.)

Where is the Africa–Australia–India triple junction?

In this section we seek to answer the following questions: are the plate motion data consistent with rigidity of the Indian, Australian and African plates, and with the boundary between the Indian and Australian plates being narrow where it intersects the Central Indian or Carlsberg Ridge? If so, where do the plate motion data indicate that the boundary between the Indian and Australian plates intersects the Central Indian or Carlsberg Ridge and what are the uncertainties in its location?

Our prior analysis of plate motion data from the Central Indian and Carlsberg Ridge showed that the boundary between the Indian and Australian plates, if narrow, intersects the Central Indian and Carlsberg Ridge somewhere between 4°N and 9°S, with the best estimate of its location being between 3°S and 6°S (Gordon *et al.* 1990). These large confidence limits were mainly the consequence of the near absence of plate motion data between 4°N and 9°S (Fig. 2b). We now have 23 new spreading rates from the aeromagnetic data in this data gap (Fig. 2a).

Here we try to fit the data along the Central Indian and Carlsberg ridges by the simplest possible model having two rigid plates (i.e. the Indian and Australian plates) moving away from the African plate. We assume that the boundary between the two plates is narrow where it intersects the ridge. Thus, each datum is assumed to record motion either between India and Africa or between Australia and Africa. A useful estimate of the most likely location for the intersection of the boundary between the Indian and Australian plates with the Central Indian or Carlsberg ridges is the location giving the smallest value of χ^2, i.e. the smallest summed squared normalized error, when fit to the 105 plate motion data. We successively calculated χ^2 for all distinct possible hypothetical locations for the intersection of the boundary with the ridge.

When we require all 105 spreading rates and azimuths along the two ridges (Table 1) to be fit by a single angular velocity, χ^2 equals 80.62. For many hypothetical locations of triple junctions, χ^2 is much lower (Fig. 11). The lowest value of χ^2 is 14.86, which is about seven times smaller than expected if we have estimated the errors correctly. Thus, as in our prior studies, if systematic errors are negligible, then we have overestimated the size of the errors, in this case by an average factor of $\sqrt{7}$. The minimum misfit occurs when the boundary between the Indian and Australian plates is assumed to intersect the Vema transform fault nearest its northern end between 8.8°S and 9.0°S (Fig. 11). The precise location of this minimum is an artefact of discretization—instead of specifying its azimuth at the middle of the transform, we could have specified it anywhere along the transform including its southern or northern end. With the available data, the true minimum could be anywhere along the transform or along the ridge segment just north of the transform.

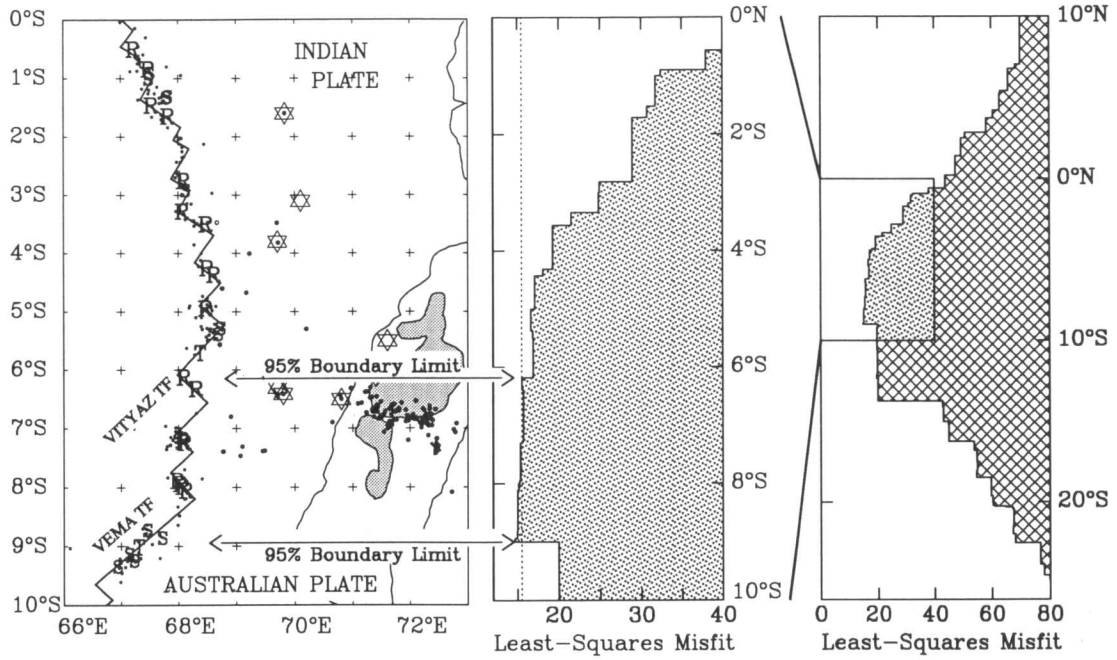

Figure 11. Results of a search for the location of the Africa–Australia–India triple junction that gives the optimal fit to the 105 Carlsberg and Central Indian ridge plate-motion data (Table 1). Right panel shows variations in χ^2, the least-squares normalized misfit, for various assumed latitudes of a hypothetical narrow boundary between India and Australia. The middle panel shows the variation in χ^2 from the equator to 10°S, which is an interval containing the minimum in χ^2. Vertical dashed line shows the threshold value of χ^2 above which the fit is significantly worse than the best fit. Left panel shows the corresponding 95 per cent confidence limit of the location of the Africa–Australia–India triple junction if the Australia–India boundary is very narrow. Locations of plate motion data (spreading rate, R; transform faults azimuths, T; and slip vectors, S) and earthquakes (post-1963, circles; pre-1963, stars) are also shown.

More useful than the location of the minimum are the limits on the possible location of the triple junction. If we assume that systematic errors are negligible and that the errors have been consistently overestimated by the same multiplicative factor, then the confidence limits can be estimated from an F-ratio test. In this case, the increase in χ^2 away from the minimum becomes statistically significant at the 2.5 per cent significance level when the Vema transform is traversed south-eastward and near the north-western end of the ridge segment just south of the Vityaz transform (i.e. at 6.2°S) as the segment is traversed north-westward. Thus a narrow boundary between India and Australia, if it is indeed narrow, is restricted to intersecting the Central Indian Ridge between 6.2°S and 9°S, along one of several ridge and transform segments north of (but possibly including part of) the Vema transform fault and south of the north-western portion of the ridge segment just south of the Vityaz transform fault. In other words, the plate motion data indicate that the Indian plate extends south to at least the Vityaz transform fault and part of the ridge segment just south of it, and possibly as far south as the Vema transform fault; the Australian plate extends north to at least the Vema transform fault, and possibly as far north as the ridge segment just south of the Vityaz transform fault, if the boundary is narrow. These new confidence limits along the ridge are less than one-fourth of the latitudinal limits of 4°N–9°S previously inferred without the new rates from aeromagnetic data (Gordon *et al.* 1990). If we instead assume that our assigned errors are correct, and use a chi-square test, the 95 per cent confidence limits are a larger, but usefully narrow, interval of 3.6°S to 9°S.

Observed spreading rates vary continuously along the ridge (Figs 12 and 13). However, the gradient in observed rates changes near 8°S, which marks the change that we interpret as the cross-over from Australia–Africa to India–Africa spreading. Although the transform-fault azimuth data are too sparse and inaccurate to resolve the precise location of the cross-over, they nevertheless provide some strong constraints. The standard error in azimuth calculated from the Africa–India best-fitting angular velocity is less than 2° along the entire Central Indian Ridge, yet the calculated value differs from the observed by 7° to 17° for every surveyed transform fault south of the Vityaz, with the difference being significant at the 95 per cent confidence level in every case. This evidence shows that a rigid Indian plate cannot extend along the Central Indian Ridge south of the Vema fracture zone. The converse is false, however. Because the Carlsberg Ridge is near the Australia–Africa pole of rotation, the standard error in azimuth calculated from the Africa–Australia best-fitting angular velocity is large along the western Carlsberg Ridge and the calculated azimuth differs insignificantly from the observed azimuth of the Owen transform fault. The large uncertainty of the azimuth of the Vityaz includes the azimuths calculated from both best-fitting angular velocities.

Further below we return to the subject of the narrowness of the boundary between India and Australia.

Motion between India and Arabia

Gordon & DeMets (1989) found that the present motion between India and Arabia is statistically insignificant if

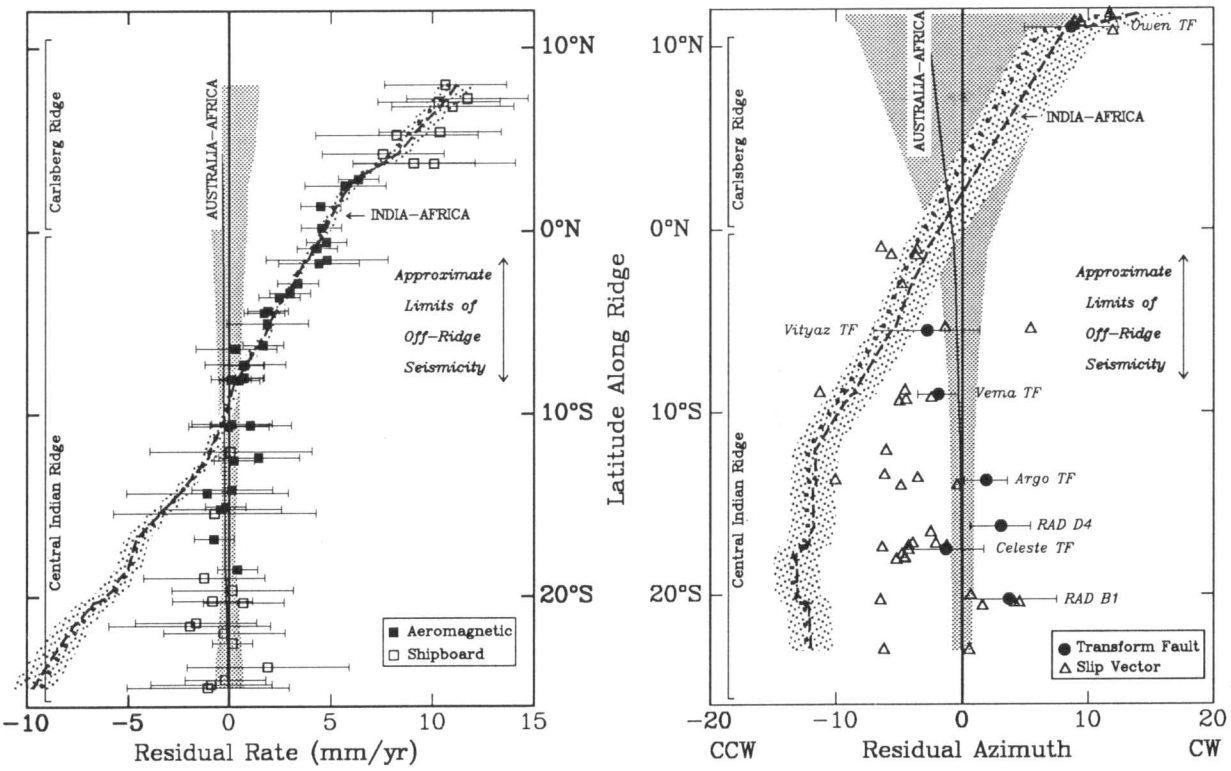

Figure 12. Spreading rates (squares), transform fault azimuths (circles), and azimuths of earthquake slip vectors (triangles) observed along the Central Indian and Carlsberg ridge systems are compared with those calculated from best-fitting and closure-enforced angular velocities describing India–Africa and Australia–Africa motion. Observed and calculated values are plotted as residuals from the values calculated from the best-fitting Australia–Africa angular velocity (Table 3). Key to curves: India–Africa best fitting angular velocity, short-dashed; India–Africa closure-enforced angular velocity, long-dashed; Australia–Africa closure-enforced angular velocity, thin solid. The $\pm 1\sigma$ errors for the values calculated from the best-fitting angular velocities are shaded with different patterns. If India and Australia were part of a single Indo-Australian plate, the Australia–Africa best-fitting angular velocity would fit all the data within the combined uncertainties of the observed and calculated values along the Carlsberg and northern Central Indian ridges.

estimated only from vector subtraction of separate India–Africa and Arabia–Africa best-fitting angular velocities. Motion differing significantly from zero was found only after fault azimuths and slip vectors from earthquakes along the Arabia–India boundary were added. The speed found was 2 mm yr^{-1} with a 95 per cent confidence interval exceeding 0 but less than or equal to 7 mm yr^{-1}. Here we re-examine these same questions to investigate how the new aeromagnetic data change these results.

The new aeromagnetic rates are slightly but systematically slower than those predicted from the best-fitting Arabia–Africa angular velocity of Gordon & DeMets (1989) (Fig. 13). The new India–Africa best-fitting angular velocity, combined with the best-fitting Arabia–Africa angular velocity of Gordon & DeMets (1989), gives an India–Arabia angular velocity of 14.8°N, 85.8°E, 0.045°/Myr, which predicts motion of 2.1 mm yr^{-1} directed N04°E with 95 per cent confidence limits of ± 1.9 mm yr^{-1} and $\pm 96°$ at 18°N, 60.2°E along the Owen fracture zone. Therefore we conclude that plate motion data along the Sheba Ridge, Carlsberg Ridge and Central Indian Ridge now show with marginal statistical significance that slow motion occurs between Arabia and India without using directional data along the Arabia–India boundary. This motion is now restricted to being no faster than 4 mm yr^{-1}. The consistency of this motion with independent data along the Owen fracture zone is tested below.

Closure tests

A continuing goal of our work has been to test the assumptions of plate rigidity and the narrowness of plate boundaries. Here we use our new aeromagnetic data to strengthen these tests.

Closure of the Africa–Arabia–India plate motion circuit

Gordon & DeMets (1989) previously applied the test for plate circuit closure to the three-plate Africa–Arabia–India circuit and found a value for F of 2.3 for 2 versus 58 degrees of freedom, which has a probability of being exceeded by chance of 11 per cent. Thus, the prior data are consistent with plate circuit closure. Repeating this test with our new set of 45 data from the Africa–India plate boundary, and with the NUVEL-1 data from the Africa–Arabia and Arabia–India plate boundaries, we find a value for F of 3.4 for 2 versus 78 degrees of freedom, which has a probability of being exceeded by chance of 3.8 per cent. Because there are many three-plate circuits that can be examined on Earth, it seems more appropriate to use a 1 per cent significance

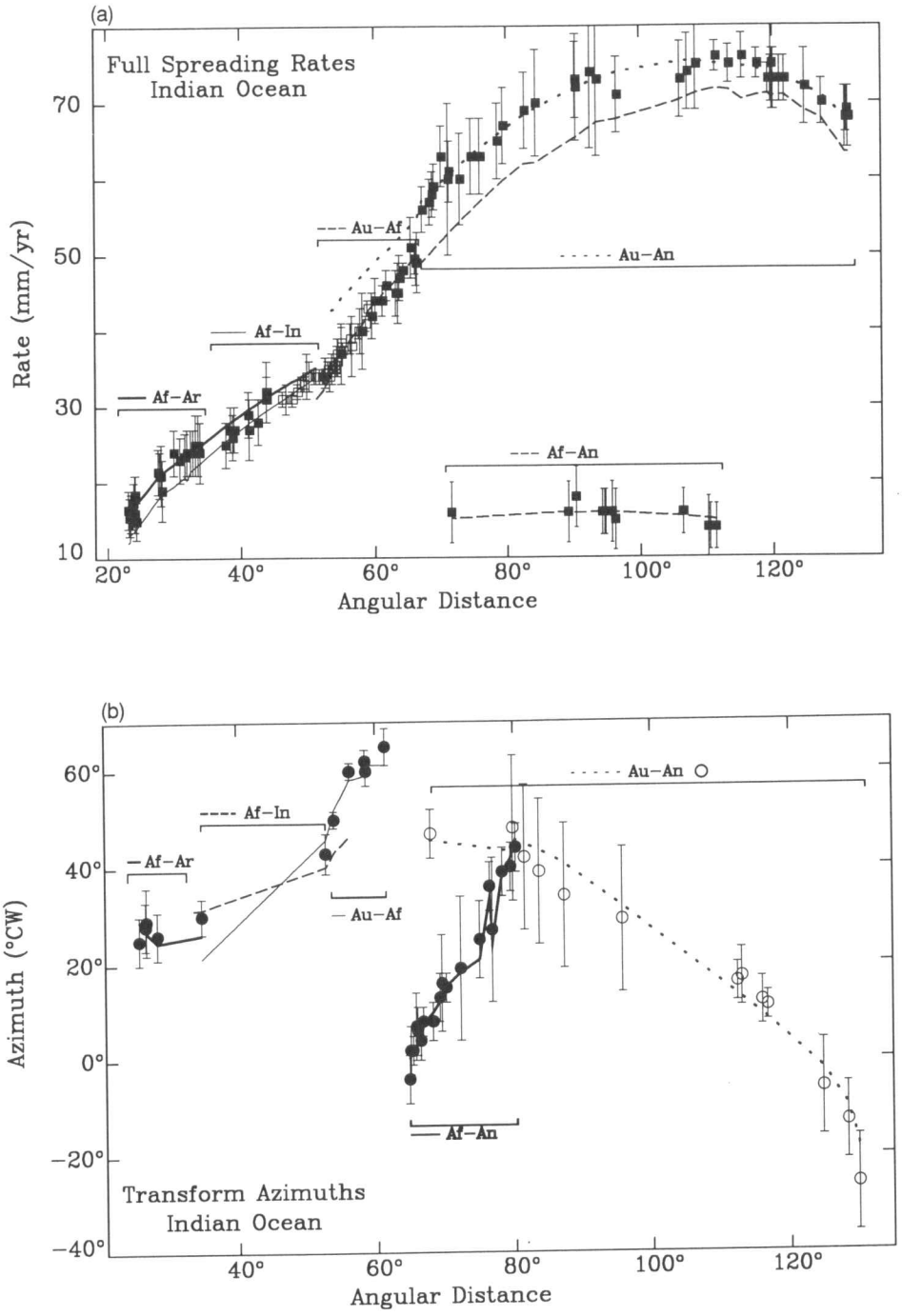

Figure 13. (a) Indian Ocean spreading rates plotted as a function of angular distance of their location from the angular velocity that best fits Africa–Arabia plate motion data. Spreading rates determined from the new aeromagnetic data are shown as open squares. The spreading rates calculated from the angular velocities that best fit the rates along each of the Indian Ocean spreading centres are shown by various curves labelled in the figure. Vertical error bars show $1-\sigma$ errors assigned to the rates. (b) Azimuths of Indian Ocean transform faults plotted as a function of distance from the angular velocity that best fits Africa–Arabia plate-motion data. Azimuths of transform faults along the Southeast Indian Ridge are shown as open circles with azimuths of other transform faults shown as solid circles. Vertical error bars show $1-\sigma$ errors assigned to the azimuths.

level than a 5 per cent significance level when examining plate circuit closure (Gordon *et al.* 1987). Thus, at the 1 per cent (but not the 5 per cent) significance level, the plate motion data remain consistent with the joint hypotheses of rigid African, Arabian and Indian plates (as far south as ~8°S along the Central Indian Ridge) and with insignificant systematic errors in the plate motion data. If we re-invert the data omitting the azimuths of slip vectors, which are a known source of systematic error, we obtain a value of F of 2.55 with 2 versus 57 degrees of freedom, which has a probability of being exceeded by chance of 9 per cent.

An alternative approach to examining closure is to use a chi-square test for closure instead of an F-ratio test (Gordon *et al.* 1987). The key difference between the two tests is that the chi-square test makes the strong assumption that the assigned errors are correct, whereas the F-ratio test assumes only that the ratios of the assigned errors along any one plate boundary are correct. The F-ratio is appropriate if, for example, the errors are all overestimated or underestimated by the same constant multiplicative factor. The dispersion of the NUVEL-1 global plate motion data set (see Fig. 9 of DeMets *et al.* 1990) suggests that this factor varies little between different types of data, although the dispersions in the present analysis suggest that the spreading rates along the Carlsberg Ridge have assigned errors that are too large relative to those assigned to azimuths of transform faults. If we instead assume that our assigned errors are correct, then we have a difference of chi-square of 0.9 with 2 degrees of freedom, which has a probability of being exceeded by chance of 64 per cent, indicating no hint of non-closure. This difference in result between the F-ratio test and chi-square test suggests that the assigned errors in the data from the Africa–Arabia–India plate motion circuit are on average too large.

Along the Carlsberg Ridge, northern Central Indian Ridge (Fig. 14a), and Sheba Ridge (Fig. 14b), all data are fit nearly as well by the three-plate model as by the best-fitting angular velocity. Along the Owen fracture zone, azimuths are fit within their uncertainties after closure is enforced (Fig. 14c). These results can be used to bound how much deformation can be taking place along a closed path on Earth's surface that crosses all three plate boundaries. The bound is incomplete because only azimuth and no rate data are available along the boundary between Arabia and India. Fig. 14(c) compares the direction and uncertainties (standard errors) of Arabia–India motion from the closure-fitting angular velocity (i.e. that determined by summing the Arabia–Africa and Africa–India angular velocities) with that found from the observed azimuths. In this case, the uncertainty in the directly observed azimuth is negligible compared with the uncertainty of the azimuth calculated from the closure-fitting angular velocity, which is ±30°–40°. For concreteness, we consider the situation at 14.6°N, where the azimuth calculated from the closure-fitting angular velocity differs from that of the best-fitting angular velocity by $31° \pm 29°$ at one standard error. Assuming that the errors assigned to the data are realistic, this implies a 95 per cent confidence limit of ±58° or a worse possible fit of 89° (=31° + 58°). With a slip rate along the Owen fracture zone of 2.1 mm yr^{-1}, this places an upper bound of 2 mm yr^{-1} (=2.1 mm yr^{-1} × sin 89°) on the component of the summed deformation perpendicular to the Owen fracture zone. That reduced chi-square is much less than one indicates that we have, on average, overestimated errors in the data by a factor of 2.7 if systematic errors are negligible. If we reduce the uncertainties by this factor, which is appropriate only if all the errors are consistently overestimated by the same multiplicative factor, the bounds on the azimuthal misfit become $31° \pm 21°$ (95 per cent confidence limits), which in turn place bounds on the deformation perpendicular to the Owen fracture zone of 0.4–1.6 mm yr^{-1} (95 per cent confidence limits).

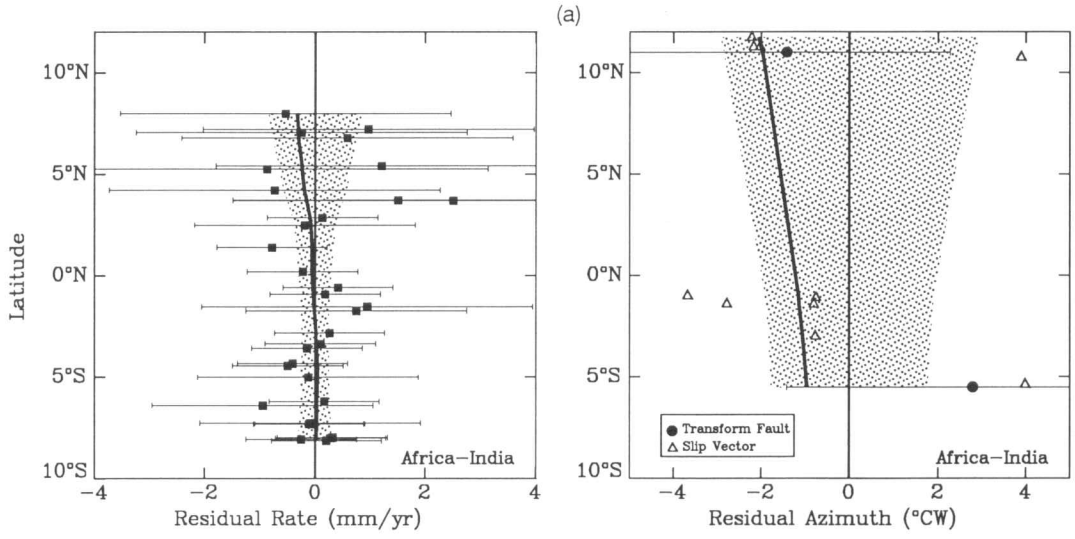

Figure 14(a). Rates and azimuths along the Carlsberg and northern Central Indian Ridge are shown after subtraction of the rate or azimuth calculated from the best-fitting Africa–India angular velocity. Observed spreading rates are shown as squares, transform-fault azimuths as circles, and earthquake slip-vector azimuths as triangles. The rates and azimuths calculated from the Africa–India three-plate angular velocity, which is determined from inversion of all data from the Africa–Arabia–India plate motion circuit, are shown by the solid curves. The $\pm 1\sigma$ errors for the best-fitting angular velocity are shaded. Error bars show the $\pm 1\sigma$ errors assigned to the rates and transform-fault azimuths.

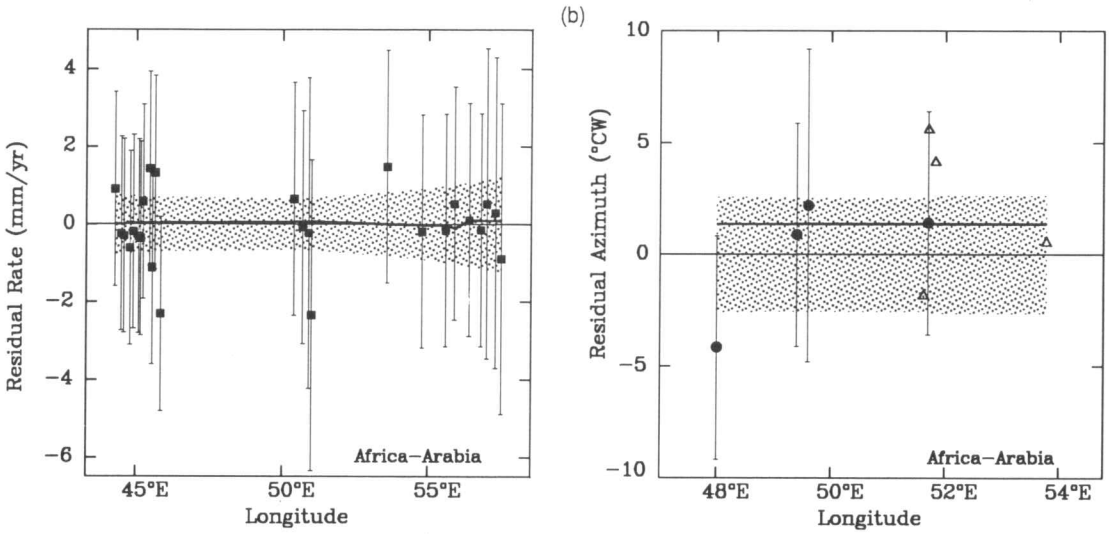

Figure 14(b). Rates and azimuths along the Sheba ridge in the Gulf of Aden are shown after subtraction of the rate or azimuth calculated from the best-fitting Africa–Arabia angular velocity. Observed spreading rates are shown as squares, transform-fault azimuths as circles, and earthquake slip-vector azimuths as triangles. The rates and azimuths calculated from the Africa–Arabia three-plate angular velocity, which is determined from inversion of all data from the Africa–Arabia–India plate motion circuit, are shown by the solid curves. The $\pm 1\sigma$ errors for the best-fitting angular velocity are shaded. Error bars show the $\pm 1\sigma$ errors assigned to the rates and transform-fault azimuths.

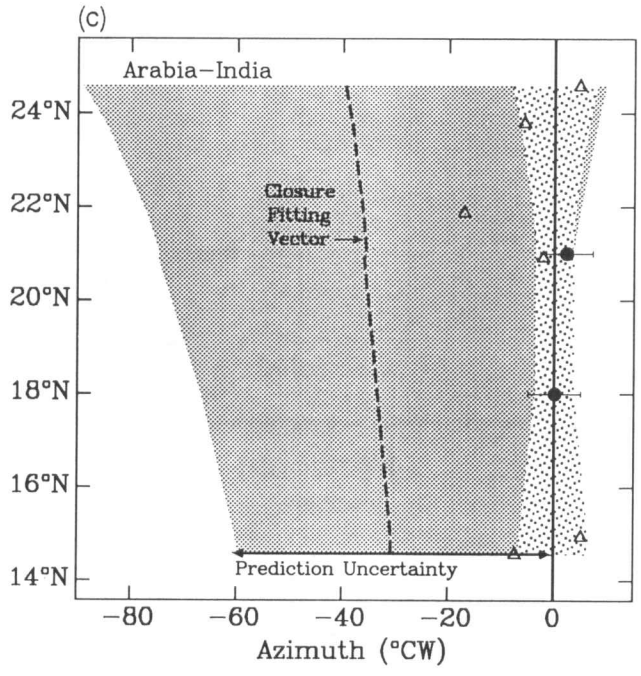

Figure 14(c). Azimuths along the Arabia–India boundary (mainly the Owen fracture zone) are shown after subtraction of the azimuth calculated from the best-fitting Arabia–India pole of rotation. Observed transform-fault azimuths as shown as circles and earthquake slip-vector azimuths as triangles. The azimuths calculated from the Arabia–India closure-fitting angular velocity, which is determined from summation of the Africa–Arabia and Africa–India best-fitting angular velocities, are shown by the dashed curve. The $\pm 1\sigma$ errors for the best-fitting angular velocity and for the closure-fitting angular velocity are shaded with different patterns. Error bars show the $\pm 1\sigma$ errors assigned to the transform-fault azimuths.

Closure of the Africa–Antarctica–Australia plate motion circuit

Several observations suggest that non-rigidity within the Australian or African plate (or both) could contribute to plate-circuit non-closure. First, active extension across the East Africa rift system shows that Nubia (West Africa) moves relative to Somalia (East Africa), although the amount of deformation is only about 3 mm yr^{-1} at the fastest separation point in the north, near Afar, and must decrease to much less in southern Africa and within the sea-floor south, south-east, and possibly east of Africa (DeMets *et al.* 1990). Second, although deformation between India and Australia is concentrated in the equatorial deforming zone, the pattern of seismicity has long suggested additional deformation may be concentrated along the southern Ninetyeast Ridge and may connect south-westward with the Southeast Indian Ridge near ~75°–80°E (Stein & Okal 1978; Stein & Gordon 1984; Bergman & Solomon 1985). Such a model would have a hypothetical 'Central Indian Basin' plate west of the Ninetyeast Ridge and a hypothetical 'eastern Australian' east of the Ninetyeast Ridge (see Fig. 17 of DeMets *et al.* (1988) for this geometry). Third, the deformation zone between India and Australia may extend south of 8.5°S, where we assume it lies for this analysis. Fourth, the deformation that occurs within a narrow salient of the Australian plate west of the Macquarie ridge complex may bias the azimuthal data located east of ~135°E (Fig. 15c) (DeMets *et al.* 1988; Royer & Sandwell 1989; Marks & Stock 1991).

DeMets *et al.* (1988) previously applied the test for plate circuit closure to the three-plate Africa–Antarctica–Australia circuit and found a value for F of 3.1 for 3 versus 231 degrees of freedom, which has a probability of being

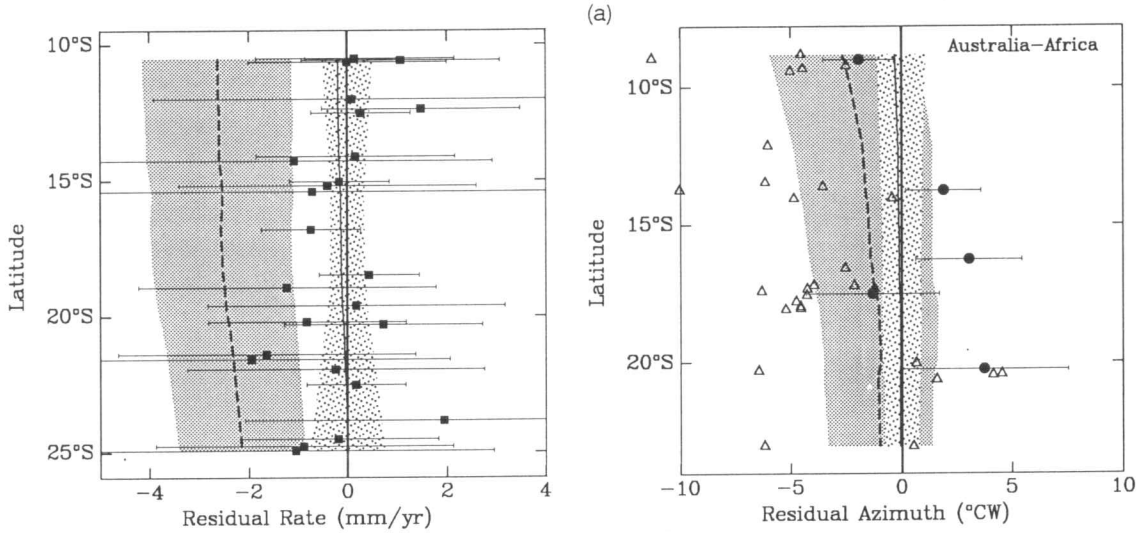

Figure 15(a). Rates and azimuths along the southern Central Indian Ridge are shown after subtraction of the rate or azimuth calculated from the best-fitting Africa–Australia angular velocity. Observed spreading rates are shown as squares, transform-fault azimuths as circles, and earthquake slip-vector azimuths as triangles. The rates and azimuths calculated from the Africa–Australia three-plate angular velocity, which is determined from inversion of all data from the Africa–Antarctica–Australia plate motion circuit, are shown by the solid curves. The rates and azimuths calculated from the Africa–Australia closure-fitting angular velocity, which is found by vector addition of the Africa–Antarctica and Antarctica–Australia best-fitting angular velocities, are shown by the dashed curves. The $\pm 1\sigma$ errors for the best-fitting and closure-fitting angular velocities are shaded with different patterns. Error bars show the $\pm 1\sigma$ errors assigned to the rates and transform-fault azimuths.

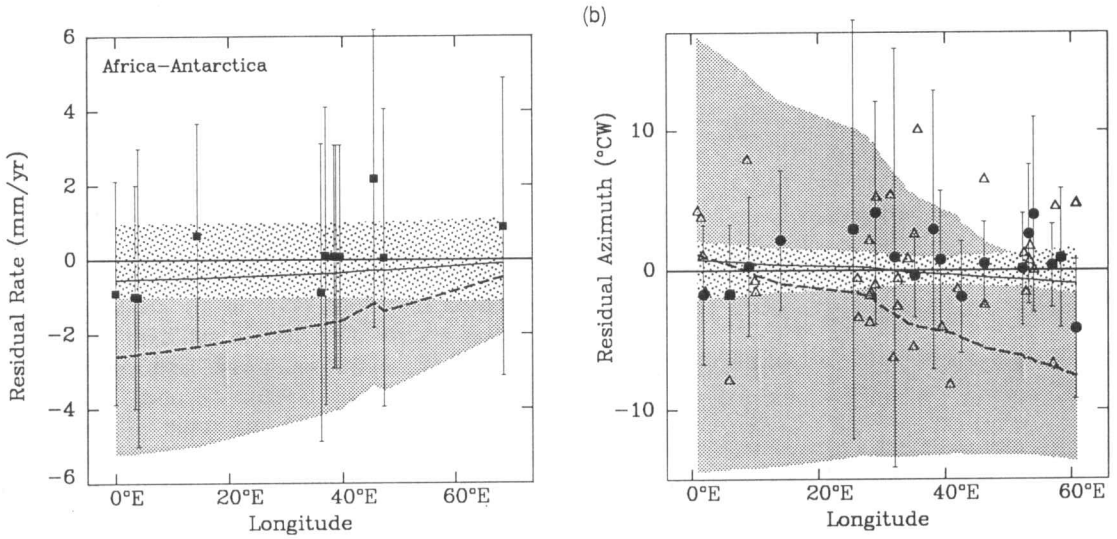

Figure 15(b). Rates and azimuths along the Southwest Indian Ridge are shown after subtraction of the rate or azimuth calculated from the best-fitting Africa–Antarctica angular velocity. Observed spreading rates are shown as squares, transform-fault azimuths as circles, and earthquake slip-vector azimuths as triangles. The rates and azimuths calculated from the Africa–Antarctica three-plate angular velocity, which is determined from inversion of all data from the Africa–Antarctica–Australia plate motion circuit, are shown by the solid curves. The rates and azimuths calculated from the Africa–Antarctica closure-fitting angular velocity, which is found by vector addition of the Africa–Australia and Australia–Antarctica best-fitting angular velocities, are shown by the dashed curves. The $\pm 1\sigma$ errors for the best-fitting and closure-fitting angular velocities are shaded with different patterns. Error bars show the $\pm 1\sigma$ errors assigned to the rates and transform-fault azimuths.

exceeded by chance of 3 per cent. Thus, the prior data are consistent with plate circuit closure at the 1 per cent significance level even when systematic errors are assumed to be negligible. From non-rigorous numerical experiments, DeMets *et al.* (1988) concluded that the data could detect intraplate deformation if it exceeded ~2 mm yr^{-1}.

Here we repeat that test by combining our new Australia–Africa data with the NUVEL-1 Africa–Antarctica and Australia–Antarctica data. We assume that the Australian plate exists as far north as ~8.5°S, which is the best-fitting location for a discrete boundary between India and Australia found above. Figs 15(a)–(c) compare the observations with the rates and azimuths calculated from the best-fitting, three-plate (i.e. closure-enforced), and closure-fitting angular velocity for each plate pair. The distance scales on these three plots are non-uniform; the Central Indian Ridge south of 9°S is several times shorter than either the Southwest Indian Ridge or the Southeast

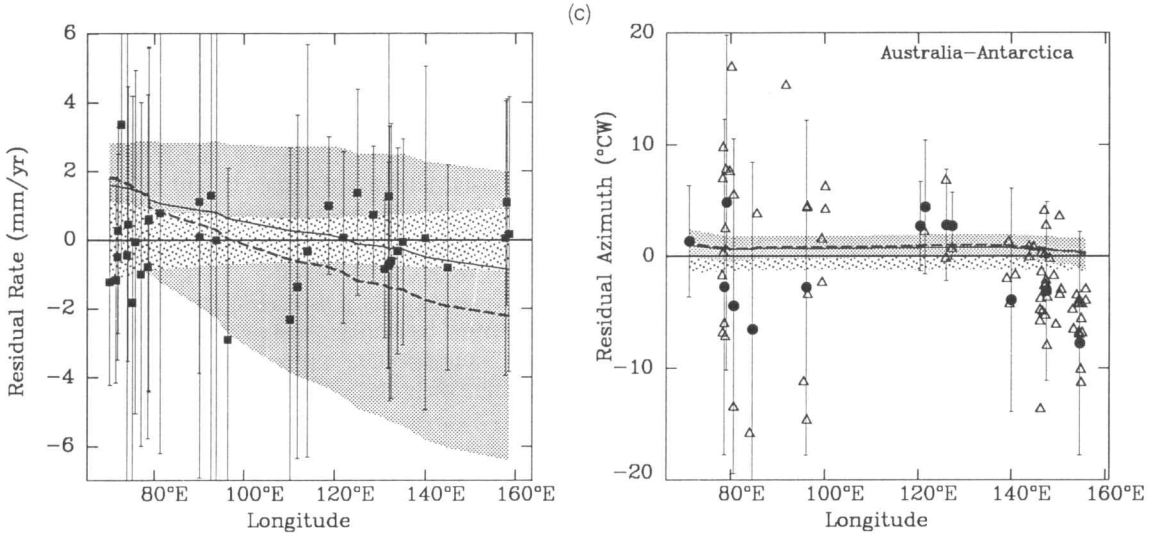

Figure 15(c). Rates and azimuths along the Southeast Indian Ridge are shown after subtraction of the rate or azimuth calculated from the best-fitting Australia–Antarctica angular velocity. Observed spreading rates are shown as squares, transform-fault azimuths as circles, and earthquake slip-vector azimuths as triangles. The rates and azimuths calculated from the Australia–Antarctica three-plate angular velocity, which is determined from inversion of all data from the Africa–Antarctica–Australia plate motion circuit, are shown by the solid curves. The rates and azimuths calculated from the Australia–Antarctica closure-fitting angular velocity, which is found by vector addition of the Australia–Africa and Africa–Antarctica best-fitting angular velocities, are shown by the dashed curves. The $\pm 1\sigma$ errors for the best-fitting and closure-fitting angular velocities are shaded with different patterns. Error bars show the $\pm 1\sigma$ errors assigned to the rates and transform-fault azimuths.

Indian Ridge and its data density is now much higher than on the other two spreading centres. Along the Central Indian Ridge, all data are fit nearly as well by the three-plate model as by the best-fitting angular velocity (Fig. 15a). Along the Southwest Indian Ridge, transform fault azimuths are fit as well by the three-plate model as by the best-fitting angular velocity, but rates are misfit systematically by 0.2–0.6 mm yr^{-1} (Fig. 15b). Along the Southeast Indian Ridge, transform fault azimuths are fit as well by the three-plate model as by the best-fitting angular velocity, but rates are predicted to be about 1 mm yr^{-1} too slow near the eastern end and 1.6 mm yr^{-1} too fast at the western end of the ridge, i.e. near the Rodriguez triple junction (Fig. 15c). We find a value for F of 6.5 for 3 versus 249 degrees of freedom, which has a probability of being exceeded by chance of 3×10^{-4}. Therefore, the data are significantly and systematically misfit at the 0.03 per cent significance level if systematic errors are negligible and all data types have errors consistently overestimated by the same multiplicative factor. If we re-invert the data omitting the azimuths of slip vectors, which are a known source of systematic error, we obtain a value of F of 5.7 with 3 versus 103 degrees of freedom, which has a probability of being exceeded by chance of 1×10^{-3}. The significant misfit implies that systematic errors are non-negligible, or (as seems likely) that the errors of both data types are not overestimated by the same multiplicative factor, or that one or more assumptions of our model—in particular that of plate rigidity—are in error, or some combination of these possibilities.

A comparison with F-ratio tests for closure about other three-plate circuits well populated with plate motion data show that the indicated significance level for non-closure is not unusually large. Values of F of 3.7, 8.3 and 7.0 have been found respectively for the plate circuits enclosing the Azores, Bouvet and Galapagos triple junctions (DeMets *et al.* 1990). Thus the plate motion data in the Africa–Antarctica–Australia circuit are about as consistent with closure as the data contained in other plate motion circuits.

If we instead assume that the assigned errors are correct and apply a chi-square test for closure, the difference in chi-square is 3.3 with 3 degrees of freedom, which has a probability of 34 per cent of being exceeded by chance. Thus, the misfits are near those expected from the errors we assigned to the data, but are large relative to the dispersion of these data about the values calculated from their respective best-fitting angular velocities.

The values calculated from the closure-fitting angular velocities differ little from those from the best-fitting angular velocities. The differences in rate nowhere exceed 3 mm yr^{-1} (Figs 15a–c). Differences in azimuths do not exceed 3° (corresponding to a rate of less than 2 mm yr^{-1}) along the Central Indian Ridge, 1° (corresponding to a rate of ~1 mm yr^{-1}) along the Southeast Indian Ridge, and 8° (corresponding to a rate of ~2 mm yr^{-1} along the Southwest Indian Ridge).

Shaded regions on Figs 15(a)–(c) show the $\pm 1 - \sigma$ error propagated from the errors in the best-fitting angular velocities and those from the closure-fitting angular velocities. These uncertainties reflect those assigned to the data, and have not been re-scaled to account for the dispersion being much smaller than expected from the assigned uncertainties. Along the two long boundaries (i.e. the Southwest Indian Ridge and the Southeast Indian Ridge), the standard errors on the closure-fitting angular velocities increase considerably with distance from the Rodriguez triple junction. Hence tests of plate circuit closure are strongest nearest the triple junction, where the differences between best-fitting and closure-fitting angular

velocities are manifested differently along each plate boundary.

Along the Southwest Indian Ridge, rates calculated from the best-fitting and closure-fitting angular velocities agree well, differing by less than $1 \pm 2\,\text{mm yr}^{-1}$ ($\pm 1\sigma$); the azimuths differ by $8 \pm 8°$ ($\pm 1\sigma$). Along the Southeast Indian Ridge, the rates calculated from the best-fitting and closure-fitting angular velocities differ by $2 \pm 1.5\,\text{mm yr}^{-1}$ ($\pm 1\sigma$); the azimuths agree well, differing by $1 \pm 2°$ ($\pm 1\sigma$). Along the Central Indian Ridge rates calculated from the best-fitting and closure-fitting azimuths differ by $2.1 \pm 1.5\,\text{mm yr}^{-1}$ ($\pm 1\sigma$) at the southern end and by $2.6 \pm 1.6\,\text{mm yr}^{-1}$ ($\pm 1\sigma$) at the northern end; the azimuths agree well, differing by $1 \pm 2.4°$ ($\pm 1\sigma$) at the southern end and by $3 \pm 3.5°$ ($\pm 1\sigma$) at the northern end. As 95 per cent confidence limits for a 1-D Gaussian distribution are 1.96 times σ, none of these differences is significant if the assigned errors are accurate. Of greater importance is the upper limit that this places on the combined effects of systematic errors and intraplate deformation. For example, near the southern end of the Central Indian Ridge, the azimuth difference is $1 \pm 4.7°$ and the rate difference is $2.1 \pm 2.9\,\text{mm yr}^{-1}$ (95 per cent confidence level). None of the lower bounds on deformation differs significantly from zero.

An upper bound for the summed deformation around the triple junction was found as follows. Subtraction of the Australia–Africa closure-fitting velocity from the corresponding best-fitting velocity calculated at the triple junction gives a residual velocity of $2.2\,\text{mm yr}^{-1}$ toward N79°E (Fig. 16). The combined covariance matrix found by summing the covariance matrices for the best- and closure-fitting Australia–Africa angular velocities gives 2-D 95 per cent principal semi-axes of $4.8\,\text{mm yr}^{-1}$ oriented S54°E and $3.6\,\text{mm yr}^{-1}$ oriented N36°E for the residual velocity (Fig. 16). This error ellipse includes the origin, as well as points with residual velocities as fast as $6.6\,\text{mm yr}^{-1}$ (Fig. 16). A rigorously determined upper bound would account for the bias inherent to multidimensional distance estimates (*cf.* Cox & Gordon 1984; Acton & Gordon 1994 and would be smaller than this, however.

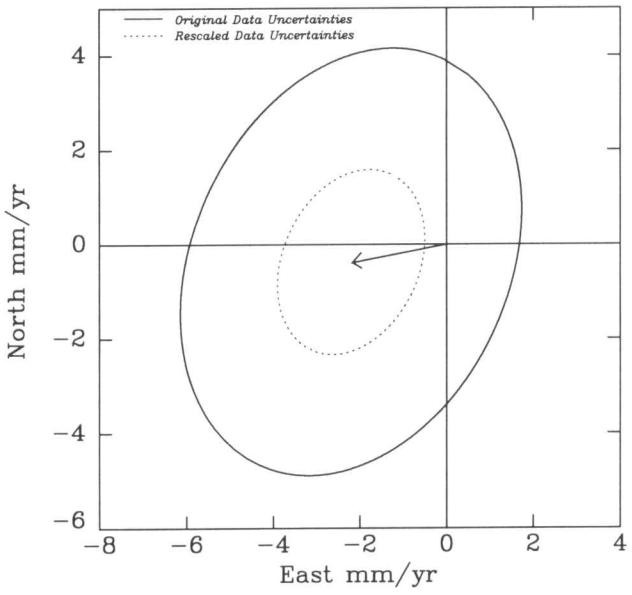

Figure 16. Residual velocity found by subtracting the Australia–Africa closure-fitting velocity at the Rodriguez triple junction from the corresponding best-fitting velocity. The 95 per cent confidence limits were calculated from two different assumptions: (1) that the assigned errors are all correct (solid ellipse), or (2) that they are all uniformly overestimated by the same multiplicative constant required to give a reduced chi-square of one when closure is unenforced (dashed ellipse).

If we assume that systematic errors are negligible and that the errors have been systematically overestimated by the same multiplicative factor irrespective of data type and location, then the confidence limits could be rescaled by multiplying them by the value of the square root of reduced chi-square. Here, this effects a division by a factor of 2.3; in the case of the southern Central Indian Ridge this gives 95 per cent confidence limits of $1 \pm 2.0°$ in azimuth and $2.1 \pm 1.3\,\text{mm yr}^{-1}$ in rate. Rescaling the covariances reduces the upper bound of the summed deformation to $4\,\text{mm yr}^{-1}$ and excludes the origin with the slowest velocity enclosed within the confidence ellipse being less than $1\,\text{mm yr}^{-1}$ (Fig. 16). This result deserves great caution in interpretation because we have treated the errors for transform faults differently on the Central Indian Ridge than on the other two plate boundaries. Moreover, systematic errors in earthquake slip vectors are clearly non-negligible. In any event these results show that this upper bound, which we believe to be smaller than the true upper bound, is larger than the upper bound ($\sim 2\,\text{mm yr}^{-1}$) that we quoted in prior work (DeMets *et al.* 1988). Evidently, our prior non-rigorous analysis gave unrealistically low bounds on the limits on intraplate deformation placed by the plate motion data.

The non-closure of this circuit, if real, is manifested by only a tiny systematic misfit to the Central Indian Ridge data (Fig. 15a). The enforcement of closure about this circuit thus causes almost no change in the resulting Africa–Australia angular velocity (Table 3). Because we calculate confidence limits from the errors assigned to the data, and because non-closure is insignificant when these errors are assumed to be correct, the resulting confidence limits are not assigned inconsistently with the non-closure indicated by the F-ratio test, but we cannot exclude a minuscule bias smaller than the difference between rates or azimuths calculated from the best-fitting angular velocity on the one hand and the three-plate angular velocity on the other.

Estimated location of the Africa–Australia–India triple junction when closure is enforced

What is the effect of the enforcement of closure on the best-fitting location and confidence limits of the Africa–Australia–India triple junction? We used the same search as before, but enforced closure about both the Africa–Arabia–India plate motion circuit and about the Africa–Antarctica–Australia plate motion circuit using the NUVEL-1 data set along the Africa–Arabia, Arabia–India, Africa–Antarctica and Australia–Antarctica plate boundaries. We found that the distribution of χ^2 values is similar to that derived from data from only the Central Indian and Carlsberg ridges. The 95 per cent confidence limit for the southernmost location of

Table 3(a). Three Myr average angular velocities for the Indian Ocean basin.

Plate Pair	Angular Velocities °N	°E	ω °/Myr	Standard Error Ellipse σ_{max}	σ_{min}	ζ_{max}	σ_ω °/Myr
Best-fitting angular velocities derived from inversion of Table 1 data							
Au-In	–3.4	74.3	0.312	3.8°	1.3°	N39°E	0.048
Au-Af	14.0	49.3	0.650	2.8°	0.7°	N32°W	0.032
In-Af	25.2	28.6	0.412	4.5°	1.9°	N57°W	0.021
Closure-enforced angular velocities derived from Table 1 and NUVEL-1 data							
Au-In	–3.2	75.1	0.305	2.5°	1.2°	N43°E	0.028
Au-Af	13.5	49.5	0.656	0.8°	0.6°	N28°W	0.009
In-Af	23.8	29.6	0.422	3.7°	1.4°	N69°W	0.018
Au-An	13.9	37.2	0.680	1.1°	0.9°	N88°W	0.005
Af-An	3.9	–37.6	0.141	5.8°	1.4°	N45°W	0.008
In-Ar	3.7	90.6	0.048	23.2°	2.4°	N59°W	0.023
Ar-Af	24.6	23.0	0.402	2.7°	1.3°	N63°W	0.022

First plate rotates counter-clockwise relative to the second. All uncertainties are 1σ. The rotation rate uncertainty σ_ω is determined from a one-dimensional marginal distribution, whereas the lengths of the principal semi-axes are determined from a two-dimensional marginal distribution. One-sigma error ellipses are specified by the angular lengths of the principal semi-axes and by the azimuths ζ_{max} of the major axis. Information about complete 3-D error ellipsoids and covariances is given in Tables 3b and 3c. Solution is derived through inversion of the data in Table 2 supplemented by Australia-Antarctica, Africa-Antarctica, Africa-Arabia, and India-Arabia data given in DeMets *et al.* (1990). Abbreviations are as follows: Af, Africa; Ar, Arabia; An, Antarctica; Au, Australia; In, India. To recalibrate these angular velocities and their uncertainties so as to incorporate recent revisions to the geomagnetic reversal time scale, multiply ω and σ_ω by 0.9562 (DeMets et al. 1994).

the India–Australia plate boundary remains at the Vema transform fault, but the northern limit is farther south, at ~8°S, along the ridge segment immediately north-west of the Vema fracture zone. This narrow confidence interval is less than one-tenth as long as the analogous confidence interval determined by Gordon *et al.* (1990).

To determine how closure of the Africa–Arabia–India circuit and of the Africa–Antarctica–Australia circuit each affect the 95 per cent confidence limits, we repeated the search for the location of the Africa–Australia–India triple junction using the subsets of data that correspond to each of these two circuits. Enforcing closure only about the Africa–Arabia–India circuit gives an optimal location for the triple junction identical to that shown in Fig. 11, but shifts the northernmost 95 per cent confidence limit southwards from 6.2°S (Fig. 11) to 7.3°S. Enforcing closure only about the Africa–Antarctic–Australia circuit also gives the same location for the triple junction, but shifts the northernmost 95 per cent confidence limit even farther south to 8.0°S. Thus, closure constraints from these two independent three-plate circuits each suggest that the 95 per cent confidence limits are narrower than shown in Fig. 11. Thus, the spreading rates calculated from the closure-enforced Australia–Africa angular velocity have small enough uncertainties to exclude the possibility that spreading rates located along the two ridge segments between 6.0°S and 7.5°S record motion between the Australian and African plates. If we instead assume that our assigned errors are correct, and use a chi-square test, the 95 per cent confidence limits span 4.4°S–9°S, only slightly narrower than those when no circuit closures are enforced.

Motion of India and Australia relative to Africa

The analysis of the data presented thus far gives two pairs of angular velocities describing the motion of India relative to Africa and of Australia relative to Africa (Fig. 17 and Table 3). The first pair of best-fitting angular velocities, those with poles of rotation 1 and 2 in Fig. 17, were derived only from the spreading rates and azimuths of plate motion along the Carlsberg and Central Indian ridges. The new best-fitting angular velocities lie within the confidence limits of those that we found before (DeMets *et al.* 1988; Gordon & DeMets 1989), but now have smaller

Table 3(b). Description of angular velocity error ellipsoids.

Plate Pair	Semi-Axis 1 σ_ω, °/Myr	Trend, °CW	Plunge, °Down	Semi-Axis 2 σ_ω, °/Myr	Trend, °CW	Plunge, °Down	Semi-Axis 3 σ_ω, °/Myr	Trend, °CW	Plunge, °Down
Semi-axes from inversion of data in Table 2									
In-Af	0.054	123.6	42.5	0.017	214.6	1.2	0.004	306.0	47.5
Au-Af	0.067	327.7	55.1	0.010	236.5	0.8	0.005	146.0	34.9
In-Au	0.085	220.1	79.3	0.020	38.4	10.7	0.009	128.4	0.3
Semi-axes from closure-enforced 5-plate model									
In-Af	0.046	112.4	43.3	0.013	210.2	8.2	0.004	308.6	45.6
Au-Af	0.018	329.9	52.5	0.009	237.8	1.6	0.005	146.6	37.5
In-Au	0.049	301.7	86.0	0.016	42.4	0.8	0.007	132.5	3.9

Semi-axis length is 1σ, and is determined from a three dimensional marginal distribution. Trend is the azimuth of the ellipse axis in the down-dip direction. Plunge is the angle between the ellipse axis and horizontal plane. See Table 3a for abbreviations. Lengths and orientations of ellipsoid semi-axes are extracted from model covariances (Table 3c) as follows: Cartesian covariances are transformed into a north, east, down coordinate system centered on the pole of rotation. Eigenvalues and eigenvectors are then derived from the n,e,d covariances. Eigenvectors specify the orientations (in north, east, and down) of the three perpendicular axes of the error ellipsoid. Eigenvalues are the squared lengths of the three semi-axes. Eigenvalues are converted to estimates of the trivariate standard error for each of the semi-axes by multiplying the length of the semi-axis by three and taking the square root of the product. To recalibrate the angular lengths of the ellipsoid axes so as to incorporate recent revisions to the geomagnetic reversal time scale, multiply σ_ω by 0.9562 (DeMets et al., 1994).

Table 3(c). Model variances and covariances.

Covariances derived from inversion of data in Table 1			Covariances derived from 5-plate closure-enforced model		
	Au-Af			Au-Af	
654.7	1438.8	-469.0	92.2	76.8	-57.3
1438.8	3627.8	-1075.1	76.8	281.2	-76.0
-469.0	-1075.1	378.4	-57.3	-76.0	74.7
	In-Af			In-Af	
566.3	1005.9	-213.0	279.7	602.3	-55.3
1005.9	2492.3	-153.0	602.3	1924.1	68.0
-213.0	-153.0	179.2	-55.3	68.0	91.6
	In-Au			In-Au	
1220.9	2444.6	-682.0	371.9	679.1	-112.6
2444.6	6120.1	-1228.1	679.1	2205.3	-8.0
-682.0	-1228.1	557.6	-112.6	-8.0	166.3

Units are 10^{-10} radians^2/m.y.^{2} Rows and columns are listed in the following order of components: x (0°N, 0°E), y (0°N, 90°E), z (90°N). See Table 3a for abbreviations. To recalibrate the covariances so as to incorporate recent revisions to the geomagnetic reversal time scale, multiply each of the covariances by 0.9562^2 (DeMets et al. 1994).

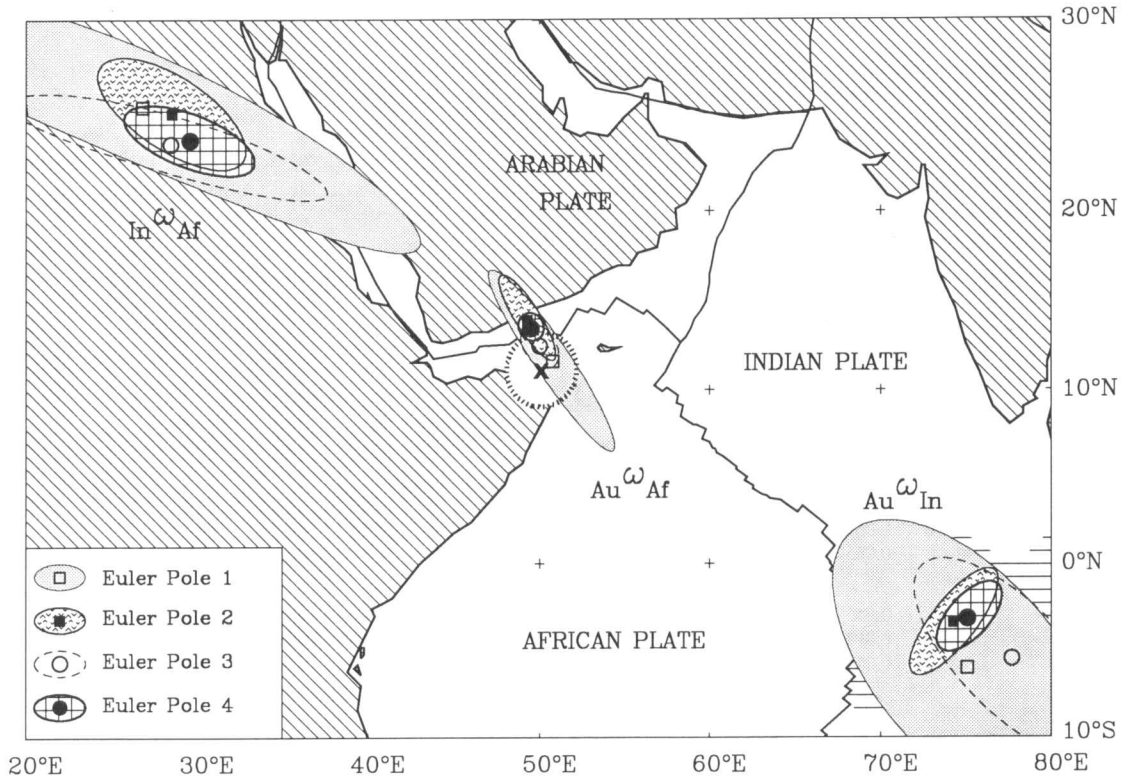

Figure 17. Comparison of India–Africa, Australia–Africa and India–Australia poles of current rotation from this and prior studies. For each plate pair, four poles of rotation are shown. Those labelled '1' are the poles of rotation for the old Africa–India and Africa–Australia best-fitting angular velocities, as well as the old Australia–India pole of rotation, which corresponds to the angular velocity obtained from the vector difference between the old best-fitting Africa–India and Africa–Australia angular velocities (Gordon *et al.* 1990). Those labelled '2' are the poles corresponding to, or calculated from, the two new best-fitting angular velocities (Table 2). Those labelled '3' are the old five-plate closure-enforced poles of rotation (Gordon *et al.* 1990). Those labelled '4' are the new five-plate closure-enforced poles of rotation (Table 3). The pole for the Australia–Africa closure-fitting angular velocity is shown with an 'X'; its confidence ellipse is dotted. All error ellipses are 2-D 1σ limits.

confidence limits. The length of the major axes of the India–Africa and Australia–Africa confidence ellipses (Fig. 17) mainly reflect the uncertainties in the rate gradient along the India–Africa and Australia–Africa boundaries; for each new best-fitting angular velocity, the major axis of the new confidence ellipse is much shorter than that of the old. Moreover, the minor axis of the India–Africa confidence ellipse is also much narrower than before. This is caused not by new data, but by changes in analysis and interpretation, i.e. by the assignment of the Vityaz transform fault azimuth to the India–Africa instead of the Australia–Africa boundary and by the assignment of a smaller error (±3.7° instead of ±5°) to the azimuth of the Owen transform fault. As might be expected with so many new rate data, the uncertainty in rotation rate has also decreased for these best-fitting angular velocities, from ±0.11° Myr^{-1} to ±0.02° Myr^{-1} for the India–Africa best-fitting angular velocity, and from ±0.07° Myr^{-1} to ±0.03° Myr^{-1} for the Australia–Africa best-fitting angular velocity (Table 3).

The second pair of angular velocities, those with poles of rotation 3 and 4 in Fig. 17, are found by enforcing closure about local three-plate circuits, as described above in the tests for closure. Unsurprisingly, enforcing closure decreases the confidence limits of the angular velocities (Fig. 17). The new closure-enforced angular velocities are similar to, but have smaller confidence limits than, the closure-enforced angular velocities that we found before (Fig. 17 and Table 3). The fit of the closure-enforced India–Africa and Australia–Africa angular velocities to the new spreading rates and azimuths are similar to that of the best-fitting angular velocities (Figs 14a and 15a). The Australia–Africa and India–Africa best-fitting angular velocities give rates that differ by no more than 0.5 mm yr^{-1} from those from the closure-enforced angular velocities. The largest difference is that azimuths along the India–Africa boundary calculated from the India–Africa closure-enforced angular velocity are 1°–2° counter-clockwise of those from the best-fitting angular velocity (Fig. 14a).

Motion of Australia relative to India

No observation from the wide plate boundary separating the Indian plate from the Australian plate was used to estimate motion between Australia and India. Instead, each of two estimated Australia–India angular velocities was calculated by subtracting an India–Africa angular velocity from an Australia–Africa angular velocity. In the first case the two best-fitting angular velocities are subtracted and in the second case the two closure-enforced angular velocities are subtracted.

Model inferred from best-fitting angular velocities

The India–Australia angular velocity that was calculated from the two best-fitting angular velocities is located 2.8° NNW of the analogous angular velocity derived from the NUVEL-1 India–Africa and Australia–Africa best-fitting angular velocities (Fig. 17). The confidence limits of the new pole of rotation are many times smaller than those of the old (Fig. 17). In particular, the N45°W axis of the error ellipse is one-seventh as long as before. Similarly the uncertainty of the rotation rate of the new angular velocity (±0.048° Myr^{-1} $1-\sigma$ error) is one-third of the old (±0.154). The new pole of rotation and angular velocity lie within the confidence limits of the old, but the old pole and angular velocity lie outside the confidence limits of the new.

Closure-enforced model

The new closure-enforced India–Australia angular velocity is similar to, and has smaller confidence limits than, the one determined from the best-fitting angular velocities (Fig. 17). The pole of rotation for the closure-enforced India–Australia angular velocity of Gordon *et al.* (1990) and that for the 0–10 Ma finite rotation of Royer & Chang (1991) are respectively located ~3.5° to the SE and 8.5° to the SSE of the new pole of rotation, which has confidence limits many times smaller than the old (Fig. 18). Similarly the uncertainty of the rotation rate of the new angular velocity (±0.028° Myr^{-1} $1-\sigma$ error) is smaller than that for the old (±0.074° Myr^{-1}). The new pole lies within the 95 per cent

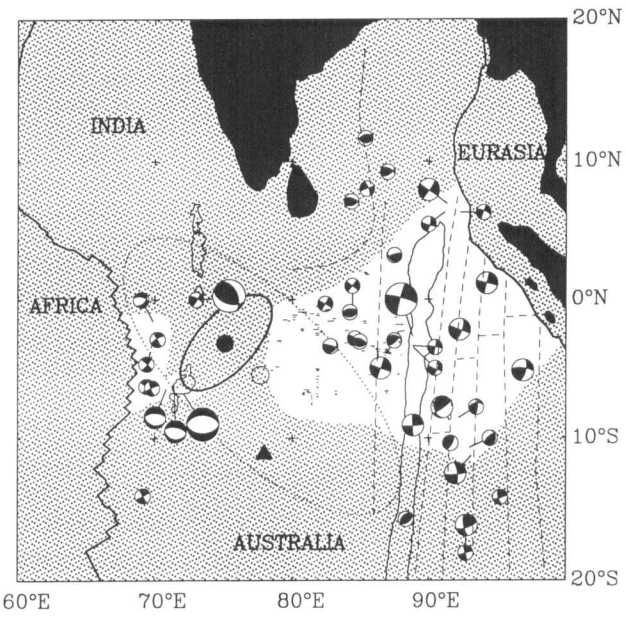

Figure 18. Tectonic map of central Indian Ocean deformation and of old and new Australia–India poles of rotation. A wide plate boundary (shown approximately by the unshaded regions) separates the assumed-rigid Australian and Indian plates. The Australian plate moves counter-clockwise relative to the Indian plate about the pole of rotation. The new pole (solid circle) has much smaller 95 per cent confidence limits (solid ellipse) than does the old pole (open circle with dotted 95 per cent confidence ellipse). The estimated pole of rotation from 10 Ma to present (solid triangle) (Royer & Chang 1991) lies near the other two poles of rotation, but outside the confidence limit of the new pole of rotation. Thin lines within the plate boundary are faults with significant basement offsets. Focal-mechanism size increases with magnitude. The largest mechanisms are for earthquakes with M_S exceeding 7.0; the middle-sized mechanisms are for earthquakes with M_S between 6.0 and 7.0; the smallest mechanisms are for earthquakes with M_S less than 6.0. The mechanisms are taken from Stein (1978), Stein & Okal (1978), Wiens & Stein (1984), Bergman *et al.* (1984), Bergman & Solomon (1985), Wiens (1986), Petroy & Wiens (1989) and the Harvard CMT catalogues (Table 5). Some mechanisms near 70°E have been omitted for simplicity.

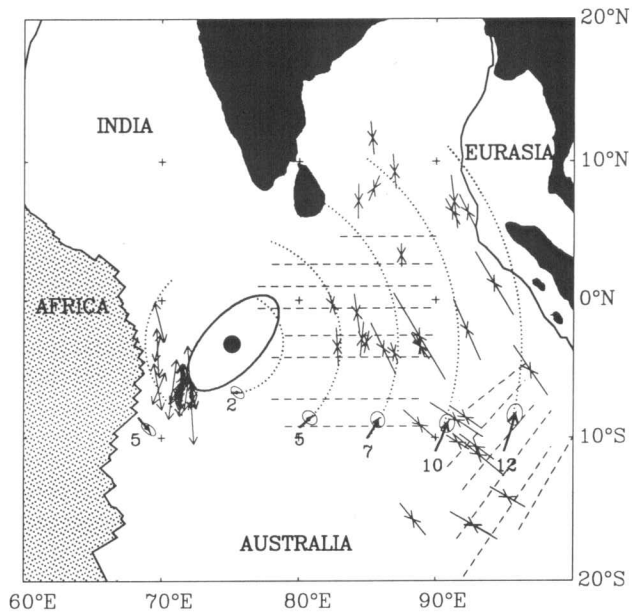

Figure 19. Predicted velocity of the Australian plate relative to the Indian plate at six locations near the postulated southern edge of the diffuse boundary. The predicted speeds in millimetres per year are given beneath the bold velocity arrows, which are drawn to show the trajectory over 25 Myr if motion were to continue with the same constant angular velocity. Error ellipses centred on the tips of the velocity arrows show 95 per cent confidence limits from the five-plate closure-enforced model. The dotted lines, which lie along small circles about the India–Australia pole of rotation (solid circle), would be tangent to the direction of India–Australia motion if the India–Australia boundary were a narrow boundary between two rigid plates. The horizontal projection of the direction of maximum shortening is shown for earthquakes east of 75°E. The horizontal projection of the direction of maximum stretching is shown for earthquakes west of 75°E. Their lengths are proportional to the logarithm of the estimated seismic moment release of each earthquake. Dashed lines show the location and orientation of gravity lineations identified by Stein *et al.* (1989).

confidence limits of the old, but the new confidence limits exclude the old pole. The new angular velocity also lies within the 3-D 95 per cent confidence limits of the old angular velocity, but the old angular velocity lies outside the 3-D confidence limits of the new.

Deformation across the deforming zone is predicted to sum to the velocity calculated for one plate relative to the other. Fig. 19 shows the velocity of Australia relative to arbitrarily fixed India at some representative locations. The 95 per cent confidence limits are in most cases several times smaller than the predicted velocity (Fig. 19). For example, a point (8.5°S, 68.3°E) assumed to be on the Australian plate near the Central Indian Ridge moves 5.1 ± 2.2 mm yr^{-1} toward S38 ± 12°E (95 per cent confidence limits) relative to the Indian plate, indicating a net divergence of Australia from India along a N–S profile near the Central Indian Ridge (*cf.* Table 4). A point (11°S, 90°E) assumed to be on the Australian plate near the Ninetyeast Ridge moves 9.8 ± 2.4 mm yr^{-1} toward N27 ± 12°E relative to the Indian plate, indicating net convergence of Australia toward India along a N–S profile through the Ninetyeast Ridge (*cf.* Table 4). The new India–Australia angular velocity unequivocally

Table 4. Predicted baseline rates of change between points on the Indian and Australian plates.

		Australian Plate						
		10°S	10°S	10°S	10°S	10°S	10°S	10°S
Indian Plate		70°E	75°E	80°E	85°E	90°E	95°E	99°E
0.0°N	70.0°E	3±2	2±2	1±2	+0±2	-0±2	-1±2	-1±2
3.0°N	75.0°E	1±1	+0±2	-1±2	-2±2	-3±2	-3±2	-3±2
3.0°N	80.0°E	-0±1	-1±1	-3±2	-4±2	-4±2	-5±2	-5±2
7.0°N	85.0°E	-0±1	-2±1	-4±2	-6±2	-7±2	-8±3	-8±3
8.0°N	90.0°E	-1±1	-2±1	-4±2	-7±2	-9±2	-10±3	-10±3

The baseline rate-of-change between 33.9°S, 151.2°E (Sydney, Australia) and 22.5°N, 88.5°E (Calcutta, India) is -12.0±2.7 mm yr^{-1} (2σ).

All rates are given in millimeters per year for points on the Australian plate relative to points on a fixed Indian plate. Positive rates indicate increasing baseline lengths; negative rates indicate decreasing baseline lengths. All uncertainties are 95% confidence limits.

predicts N–S to NW–SE convergence across the eastern portion of the plate boundary and N–S divergence across the portion of the plate boundary near the Central Indian Ridge. Except for a small region near the edge of the confidence ellipse, the new model also unequivocally predicts a component of N–S divergence across the deforming zone along the edge of the Chagos Bank (Fig. 19). The new rate of rotation is slower than we found before; thus many predicted rates are slightly slower than we found before. Because the pole of rotation is farther west than before, the new model predicts slower rates of divergence summed across the western portion of the plate boundary and slightly faster convergence summed across the easternmost portion of the plate boundary than was predicted by the old model (Fig. 19 and Table 4; *cf.* Table 2 of Gordon *et al.* 1990).

DISTRIBUTED DEFORMATION BETWEEN INDIA AND AUSTRALIA

Introduction

Predicting the motion of the rigid interior of the Australian plate relative to the rigid interior of the Indian plate (Fig. 19) is insufficient to predict specific motions within the deforming zone between them (see, e.g. McKenzie & Jackson 1983). Here, we discuss the predictions of the revised model in relation to current knowledge about deformation within the divergent zone near the Central Indian Ridge and within the convergent zone east of ~75°E.

Is the boundary between India and Australia narrow or wide near the Central Indian Ridge?

To this point, we have considered only the simplest tectonic and kinematic model for the motion between India and Australia near the Central Indian Ridge, one in which rigid plates are separated by a narrow boundary, i.e. one with a width comparable to a typical oceanic transform fault (0.5–2 km: Fox & Gallo 1986; Searle 1986) or spreading centre (where volcanism is concentrated within a zone 1–2 km wide but some deformation occurs over a zone

8–60 km wide; Macdonald 1982). As can be seen from Figs 14 and 15, the plate motion data are well fit by this model and do not require greater complexity. If the plate boundary between India and Australia is in fact wide near the Central Indian Ridge, then the departure from plate rigidity is small enough that the data, in particular the spreading rates, cannot resolve it. Here we examine other observations to test these assumptions further.

A narrow boundary ought to have some bathymetric expression and be marked by seismicity. The velocity across a narrow boundary should be that predicted by the angular velocity. The seismicity observed immediately east of the ridge is not narrow; it is distributed between ~4°S and 8°S (Figs 1 and 11). If the boundary is narrow, our analysis above limits its intersection with the Central Indian Ridge to be no farther south than the Vema transform fault and no farther north than part of the ridge segment just south of the Vityaz transform (or possibly a little farther north if the assumption of consistent overestimation of the errors is inappropriate). If closure is enforced, the boundary can occur no farther north than the ridge segment just north of the Vema transform fault. Available bathymetric and satellite-altimetric data suggest only one set of candidate sea-floor structures that might be the India–Australia plate boundary—the fracture zones on the Indo-Australian side of the Central Indian Ridge, namely the Vema fracture zone, the two fracture zones immediately to the north of the Vema, the Vityaz fracture zone, or the fracture zone immediately north of the Vityaz. We will refer to the first and second fracture zones north of the Vema respectively as the 'Vema-N1' and the 'Vema-N2' fracture zones, and the fracture zone north of the Vityaz as the 'Vityaz-N1'.

The India–Australia angular velocity determined from the two best-fitting angular velocities predicts velocities of 4.6 ± 1.3 mm yr^{-1} toward N38 ± 8°W, 4.3 ± 1.3 mm yr^{-1} toward N33 ± 10°W, 4.0 ± 1.2 mm yr^{-1} toward N29 ± 12°W, 3.6 ± 1.2 mm yr^{-1} toward N19 ± 16°W, and 3.4 ± 1.1 mm yr^{-1} toward N11 ± 19°W (all $\pm 1\sigma$ uncertainties) where the Vema, Vema-N1 and Vema-N2, Vityaz and Vityaz-N1 fracture zones respectively intersect the ridge. The India–Australia closure-enforced angular velocity predicts corresponding velocities of 5.0 ± 1.1 mm yr^{-1} toward N36 ± 6°W, 4.7 ± 1.0 mm yr^{-1} toward N31 ± 7°W, 4.4 ± 1.0 mm yr^{-1} toward N27 ± 8°W, 4.0 ± 1.0 mm yr^{-1} toward N18 ± 10°W, and 3.8 ± 0.9 mm yr^{-1} toward N11 ± 11°W (all $\pm 1\sigma$ uncertainties). The predicted azimuths of motion can be compared with the corresponding observed fracture-zone azimuths of N45°E, N42°E, N42°E, N43°E and N43°E, which are more than 50° from the predicted azimuths. The large differences between predicted and observed azimuths show that none of these fracture zones could serve as the sole boundary unless the motion across one of them was mainly stretching perpendicular to the strike of the fracture zone.

The few earthquakes along these fracture zones large enough to have estimated mechanisms (Table 6) are dominantly strike slip, however. Between 69° and 70°E, the mechanisms of five earthquakes located close to, but east of, the Central Indian ridge and transform system are available (Fig. 20). Four of these have strike-slip mechanisms, with two occurring on or near the Vema fracture zone and two occurring near or a few tens of kilometres north-west of the Vityaz fracture zone. Each of these four mechanisms has one nodal plane that could accommodate right-lateral strike slip along the nearby fracture zones (Wiens 1986). This azimuth is very different from that predicted if each earthquake occurred along a narrow boundary dividing India from Australia. On the other hand, the other nodal plane of each earthquake, corresponding to left-lateral slip, gives a direction closer to that predicted for India–Australia motion. There is no evidence in the geophysical (Fig. 3) and satellite-altimetric profiles in the region, however, for a north-west-striking feature that might accommodate the prescribed azimuth of left-lateral strike slip. Moreover, the existence of such a hypothetical feature still would not explain how the motion was transferred to the Central Indian ridge and transform system. Therefore, this hypothesis can be rejected both as being inconsistent with the observations and as insufficient to explain the basic constraint. The focal mechanism of the fifth earthquake in the region, which indicates mainly normal faulting but with a component of strike slip, is too far north to be on any narrow boundary between India and Australia.

Therefore, we can exclude the hypothesis that the slip in any of these earthquakes is recording motion across a single narrow boundary. Thus, it seems likely that the motion is accommodated across a deforming zone with multiple faults. This is not completely convincing, however, because the component of predicted stretching perpendicular to the fracture zones is merely ~10–12 km over the past 3 Myr. With the sparse bathymetric data available for this region, it is hard to exclude the possibility of this small amount of stretching across one fracture zone.

Perhaps the best guide that we currently have for the near-ridge N–S width of the deforming zone is the N–S extent of seismicity east of the Central Indian Ridge and transform system, but west of the Chagos–Laccadive Ridge. This seismicity seems to be distributed mainly between the Sealark and Vema fracture zones (i.e. about 4°S–8°S; Fig. 20), but some earthquakes related to the distributed deformation may occur as far north as 1°S and as far south as ~1.5°S (Fig. 18). The diffuseness of the deformation indicated by the failure of the earthquake epicentres to align on a single feature may be due, at least in part, to uncertainties in the locations of these earthquakes. That the epicentres align well along the south edge of Chagos Bank, along what appears in bathymetric charts to be a linear depression, provides some qualitative evidence, however, that the uncertainties in the locations are small enough to show that seismicity west of the Chagos–Laccadive Ridge but east of the Central Indian Ridge is really diffuse. All it would take to change this interpretation, however, is one large earthquake along a fracture zone with a mechanism indicating a large component of horizontal stretching perpendicular to the fracture zone.

A stronger test of the rigid-plate narrow-boundary hypothesis can probably be made by examining the fit to crossings of older anomalies, including anomalies 5 and 6, building upon Royer & Chang's (1991) analysis of a data set much sparser than is now available.

In contrast to the distributed seismicity west of 70°E, earthquakes between ~71°E and 73°E are concentrated along the southern and south-western edge of the Great Chagos Bank, suggesting that deformation there is localized

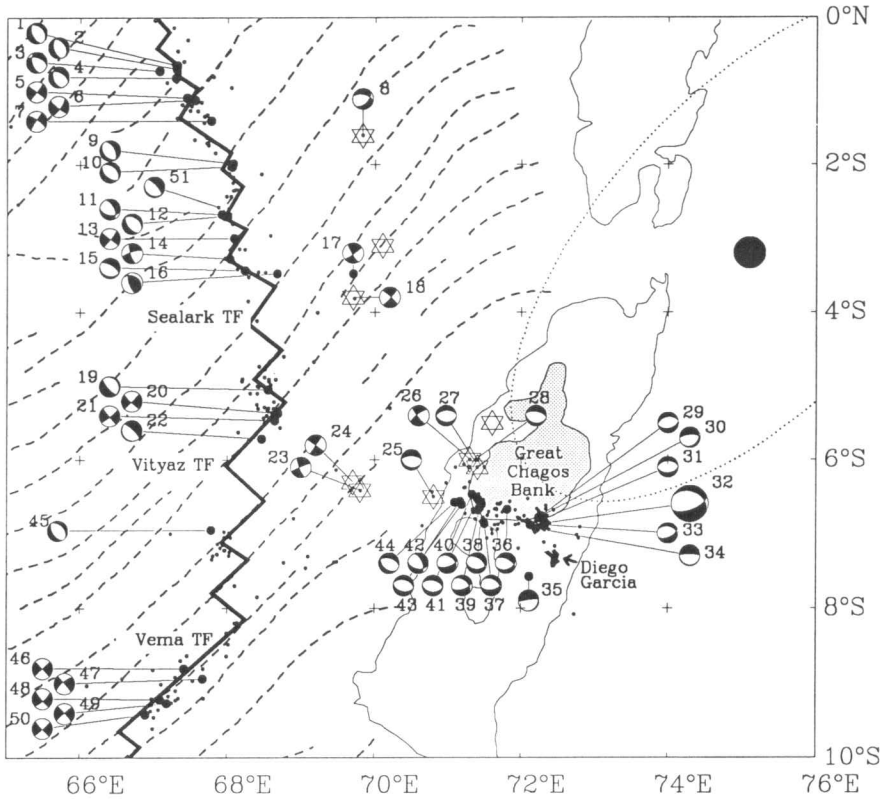

Figure 20. Epicentres and focal mechanisms (Table 6) of earthquakes near the intersection of the boundary between India and Australia with the Central Indian Ridge. Stars show locations of earthquakes from 1900 to 1977 (Wiens 1986); other epicentres are for shallow earthquakes from 1963 to 1988 (NGDC earthquake data file). Bathymetric contours are shown at 300 m and 1000 m. The new five-plate closure-enforced Australia–India pole of rotation (solid circle) and its 95 per cent confidence limits (dotted ellipse) are shown.

in latitude along a narrower, possibly discrete, zone. This possibility is examined in Fig. 21, which shows that the observed slip differs significantly from the predicted direction of slip. We infer that either the southern flank of the Chagos Bank is not a single narrow boundary between the Indian and Australian plates or that rotations of blocks within the rift about vertical axes are large enough that the slip vectors fail to parallel the motion of the bounding plates. The directions of slip portray a pattern that is characteristic of most regions of distributed deformation: the slip vectors from the largest earthquakes are more nearly perpendicular to the strike of the deforming zone than they are parallel to the direction of the bounding rigid blocks.

Comparison of predicted motion with deformation observed in the plate boundary zone between Australia and India

Many data not used to obtain our plate motion model record deformation in the wide plate boundary between India and Australia. These data place limits on the sense and orientation of average principal strains in the zone between the assumed-rigid Indian and Australian plates. The simplest predictions made by our model are that east of the pole of rotation the rigid Indian and Australian plates converge, whereas west of the pole of rotation they diverge (Fig. 18) (*cf.* Gordon *et al.* 1990). Because the pole lies near our prior pole, the predictions differ only modestly from those made before, but the uncertainties of the predictions are much smaller than before.

These predictions remain mainly consistent with the observed deformation as indicated by earthquake focal mechanisms, thrust faults mapped by reflection seismic data, and topographic and geoidal undulations. The western zone can be divided into the two provinces discussed above: the near-ridge province where mainly strike-slip earthquakes occur, and the Chagos rift farther east (Figs 18 and 20). In the near-ridge province the direction of the maximum principal stretching of the crust in earthquakes is nearly N–S, consistent with predictions. The existence of the one normal-faulting event at ~1.5°S suggests that at least some of the deformation involves crustal thinning processes also with a N–S direction of maximum stretching.

Many data imply N–S to NW–SE shortening in the eastern plate boundary. The horizontal projection of the direction of maximum shortening in earthquake focal mechanisms and the horizontal direction perpendicular to topographic lineations, to geoidal lineations, and to the strike of thrust faults is nearly N–S west of the Ninetyeast Ridge but more nearly NW–SE east of Ninetyeast Ridge (Fig. 19) (Bergman & Solomon 1985; Petroy & Wiens 1989; Stein, Cloetingh & Wortel 1989). The indicated direction of maximum shortening is not inconsistent with the motions predicted from the new angular velocity.

The observations that are unexplained by our model are the two isolated focal mechanisms on the Laccadive Ridge

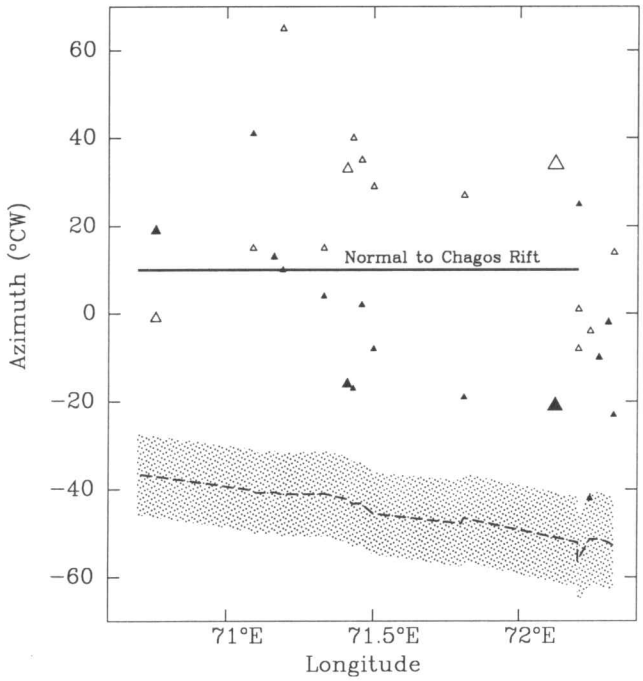

Figure 21. Azimuths of slip vectors along both nodal planes for earthquakes along the apparent rift south of the Chagos Bank (Fig. 20 and Table 6); all the earthquakes were normal-faulting events. Solid and open triangles show slip azimuths computed for planes that respectively dip to the north and south. Triangle size increases monotonically with earthquake magnitude, with the largest triangle corresponding to the 1983 November 30, $M = 7.6$ earthquake, and the remaining earthquakes mainly representing small aftershocks. The direction of motion predicted by the India–Australia closure-enforced angular velocity (Table 3) is shown by a dashed line with its $\pm 1\sigma$ uncertainties stippled; it differs systematically and significantly from the azimuths of earthquake slip.

near the equator. The mechanism of the large mainly thrust earthquake was determined from old (1944) data (Table 5), however, and may be unreliable (Wiens 1986); thus we are hesitant to place much weight on it. The other mechanism is from an earthquake that is small ($M_0 = 7 \times 10^{23}$ dyne cm). It suggests that our model is incomplete in detail, but the deformation it represents is so small that it does not contradict the observations that the deformation west of the pole of rotation is dominated by N–S stretching.

Although a few earthquake focal mechanisms show a component of thrust faulting east of ~86°E, the dominant mode of deformation is by strike-slip faulting (Fig. 18). Thus little of the convergence is taken up by thickening of the crust or lithosphere. Therefore shortening must be mainly accommodated by north-eastward transport, accompanied by inevitable rotation of crust and lithosphere; this transport of lithosphere is presumably accommodated by faster subduction at the Sumatra Trench (Gordon *et al.* 1990).

POSSIBLE TESTS AND FUTURE DIRECTIONS OF RESEARCH

Our model makes testable predictions of the angular velocity of Australia relative to India. These predictions can now be made with severalfold better accuracy than the predictions we made before (i.e. in Gordon *et al.* 1990). A direct way to test these predictions would be to estimate the angular velocity of Australia relative to India using space geodesy. With two or more sites on each continent, a very strong test could be made by independently estimating the angular velocity of Australia relative to India. Other tests can be made with fewer observing sites. In a reference frame stationary relative to India, the velocity predicted for Sydney, Australia (33.87°S, 151.22°E), for example, is 33 ± 6 mm yr^{-1} toward N05 ± 4°E (95 per cent confidence limits), which could be tested with observations from at least two observing sites on the Indian plate plus a site in Sydney. Similarly, in a reference frame stationary relative to Australia, the velocity predicted for Calcutta, India (22.5°N, 88.5°E), for example, is 16 ± 3 mm yr^{-1} toward S61°E ± 4° (95 per cent confidence limits), which could be tested with observations from at least two observing sites on the Australian plate plus a site in Calcutta. A strong test can still be made with just one site on each continent. For example, the new angular velocity predicts that the chord connecting Sydney and Calcutta should be shortening at a rate of 12 ± 3 mm yr^{-1} (95 per cent confidence limits).

The new tight bounds on the angular velocity describing motion between India and Australia now provide useful constraints on the integral of the velocity gradient across the deforming zones. An important next step should be the proposal of specific models for how motion is accommodated within the deforming zones and tests of the consistency of these models with both the bounds from the angular velocity and with the observed distribution and mechanism of earthquakes in the deforming zone. It seems inappropriate, however, to compare 3 Myr of motion with the total deformation observed in the zone. Such comparisons require accurate estimates of the total rotation between India and Australia.

Molnar, Pardo-Cesas & Stock (1988) and Royer & Chang (1991) show that motion between India and Australia can be resolved from magnetic anomaly and fracture zone crossings used to constrain finite reconstructions. In particular, Royer & Chang (1991) show that the pole of total rotation between India and Australia since either 10 Ma or 20 Ma is similar to the 0–3 Ma pole of rotation (Gordon *et al.* 1990), but with very large confidence limits. Their results further indicate that motion began between 10 and 20 Ma (but with marginal statistical significance), before the age inferred from seismic stratigraphy and deep-sea drilling (Cochran 1990). Each of our 35 long, fracture-zone parallel, aeromagnetic profiles spans all or nearly all the sequence from the central anomaly to anomaly 6 on both sides of the ridge crest. The next step in our work will be to analyse the crossings of anomalies 5 and 6, to compare past with present motion between India and Australia, to bound the total motion between the two plates, if possible, and to place bounds on when motion started.

The 95 per cent confidence limits on the location of the boundary between India and Australia where it intersects the Central Indian Ridge are small only if we assume that the boundary itself is narrow. If it is wide, as suggested by arguments presented above, there are more adjustable parameters, and these cannot be tightly constrained with available data. Most of the near- but off-ridge earthquakes

Table 5. Epicentral parameters for earthquakes in the central Indian Ocean.

Date mo.dy.yr	Latitude (°N)	Longitude (°E)	M_o (10^{24} dyn cm)	Mechanism†	Source
03.09.28	-2.66	88.83	4800	194/84/351	Petroy and Wiens (1989)
02.29.44	0.3	74.8	1400	110/50/060*	Wiens (1986)
01.23.49	-11.23	93.13	130	085/80/195	Petroy and Wiens (1989)
03.22.55	-8.74	91.54	170	055/78/118	Petroy and Wiens (1989)
10.02.57	-6.30	69.70	14	035/90/180	Wiens (1986)
05.25.64	-9.08	88.89	9.6	177/87/005	Bergman and Solomon (1985)
09.12.65	-6.5	70.8	68	270/60/260	Stein (1978)
10.31.65	-14.22	95.27	6.1	165/68/009	Bergman and Solomon (1985)
03.02.68	-6.09	71.41	7.7	284/52/280	Bergman and Solomon (1984)
03.31.70	-3.80	69.70	15	248/62/217	Wiens and Stein (1984)
04.25.70	-6.41	69.80	3.5	320/78/330	Wiens and Stein (1984)
10.10.70	-3.56	86.19	41	019/89/358	Bergman and Solomon (1985)
06.26.71	-5.18	96.90	54	014/67/019	Bergman and Solomon (1985)
11.24.72	11.67	85.34	3.0	254/52/076	Bergman and Solomon (1985)
04.07.73	7.00	91.32	25	034/84/356	Bergman and Solomon (1985)
08.30.73	7.15	84.33	3.7	290/52/118	Bergman and Solomon (1985)
11.17.73	-1.60	69.83	7.4	278/55/322	Wiens and Stein (1984)
08.03.78	-0.93	84.24	5.9	261/53/090	Bergman and Solomon (1985)
09.29.79	1.19	94.25	220	284/88/181	††
10.16.79	6.39	91.20	2.4	014/76/353	††
01.28.80	-3.39	88.87	2.6	280/83/178	††
03.11.80	-3.37	88.89	1.7	018/62/350	Petroy and Wiens (1989)
12.02.81	-15.82	88.39	6.2	195/52/033	††
04.12.81	8.07	85.46	1.8	340/73/183	††
08.21.83	3.25	87.49	1.6	132/23/146	††
11.18.84	0.07	74.83	0.7	297/68/166	††
08.11.86	-14.80	66.37	0.5	296/45/232	††
03.15.87	-10.35	91.63	2.2	224/19/105	††
09.22.87	-0.77	84.41	1.0	307/90/180	††
02.10.89	6.35	92.30	6.2	291/71/184	††
06.20.89	-3.88	87.00	1.1	284/31/139	††
10.15.89	-0.32	82.43	0.9	299/90/180	††
12.17.89	-8.55	92.21	7.6	259/46/158	††
01.06.90	-10.67	93.02	12	008/25/052	Dziewonski *et al.* (1991a)
10.15.90	-2.20	92.28	135	019/70/358	Dziewonski *et al.* (1991c)
01.13.91	-2.86	84.61	5.9	048/33/022	Dziewonski *et al.* (1992a)
05.13.91	-3.42	82.81	10	041/27/028	Dziewonski *et al.* (1992b)
01.11.92	9.27	86.98	3.5	296/48/136	Dziewonski *et al.* (1993a)
06.02.92	-16.14	92.75	6.8	254/90/-180	Dziewonski *et al.* (1993b)
06.02.92	-16.20	92.81	25	169/70/021	Dziewonski *et al.* (1993b)
08.16.92	-3.07	84.96	1.0	090/33/072	Dziewonski *et al.* (1993c)

† Strike (°CW from N)/Dip (°CW rotation about strike)/Slip (°CCW from strike, in nodal plane)

†† See Dziewonski *et al.* (1990) for a complete listing of references to centroid moment tensor solutions for earthquakes that occurred prior to 1/01/90.

* Focal mechanism is poorly constrained.

are distributed between ~4°S and the Vema transform fault at ~8.2°S (Fig. 20). North of the Vema transform fault and south of the Sealark transform fault, which is the interval that seems most likely to be accommodating distributed relative motion between the Indian and Australian plates, our model suggests that the predicted directions of India–Africa motion may differ from those of Australia–Africa motion with increasing differences to the south. The uncertainties in calculated direction are too large, however, to demonstrate this for transform faults north of ~7°S (Fig. 22). (These results are only slightly modified and give slightly smaller uncertainties if we instead use the results from the five-plate solution enforcing closure about both the Owen and the Rodriguez triple junctions.) Whether the direction of India–Africa motion differs significantly from that of Australia–Africa motion could be more strongly tested by obtaining new data that would more narrowly limit transform-fault azimuths along the Carlsberg Ridge, which would permit more accurate predictions of the direction of India–Africa motion along the Central Indian Ridge. Such improved accuracy could be attained from surveys of transforms north-west of the Sealark transform fault (~4°S). Moreover, if new data gave a more accurate azimuth of the Vityaz transform, as well as new and accurate azimuths of the two transform faults between the Vema and the Vityaz, then a stronger test could be made of whether these transforms are consistent with India–Africa motion, with Australia–Africa motion, or with neither. Even if a narrow fault zone only 3 km wide could be identified along the entire length of each of the two transforms south of the Vityaz, however, the smallest conceivable 95 per cent confidence limits that could be determined for their azimuths from simple calculations like those used in Table 2 are ±2.2° for the transform near 6.8°S and ±2.7° for the transform near 7.6°S. Thus new observations may very well exclude either the direction of India–Africa motion or that of Australia–Africa motion, but are unlikely to be able to discern a direction of motion significantly different from both (i.e. between the two predicted directions of motion) unless the confidence limits on the predicted directions can be further reduced.

A final future direction of research is to try to estimate uncertainties that are both more realistic and more consistent with the uncertainties used in finite rotations (e.g. Royer & Chang 1991). In this paper we believe that the uncertainties of transform-fault azimuths are for the first

Table 6. Epicentral parameters for earthquakes in the region 0°N–10°S, 65°E–76°E.

No.	Date mo.dy.yr	Latitude (°N)	Longitude (°E)	M_o (10^{24} dyn cm)	Mechanism†	Source
1	01.05.85	-0.65	67.31	2.4	315/37/-108	††
2	01.05.85	-0.70	67.30	1.3	324/40/-106	††
3	01.05.85	-0.72	67.07	0.9	289/49/-132	††
4	01.05.85	-0.82	67.29	0.5	163/48/-56	††
5	09.06.89	-1.09	67.44	2.6	307/90/180	††
6	07.16.81	-1.12	67.55	2.2	35/73/-10	††
7	05.09.85	-1.40	67.77	6.0	304/76/-173	††
8	11.17.73	-1.60	69.83	7.4	278/55/322	Wiens and Stein (1984)
9	09.07.72	-1.99	68.07	3.5	335/55/276	Huang and Solomon (1987)
10	08.21.80	-2.03	68.06	3.5	311/39/-92	††
11	01.11.85	-2.68	67.91	2.7	100/46/-134	††
12	12.25.79	-2.70	67.96	5.8	303/36/-107	††
13	03.17.79	-3.00	68.08	3.5	38/83/-1	††
14	07.27.88	-3.28	68.03	0.8	253/77/-167	††
15	11.16.88	-3.44	68.23	1.0	103/25/-107	††
16	08.04.78	-3.48	68.67	1.3	300/33/54	††
17	05.20.78	-3.48	69.70	1.9	148/81/08	††
18	03.31.70	-3.80	69.70	15	248/62/217	Wiens and Stein (1984)
19	12.14.84	-5.05	68.55	1.2	333/16/-76	††
20	03.06.88	-5.37	68.68	0.6	134/82/-178	††
21	04.28.87	-5.47	68.46	0.6	51/83/-4	††
22	10.21.89	-5.72	68.64	2.1	145/12/-79	††
23	04.25.70	-6.41	69.80	3.5	320/78/330	Wiens and Stein (1984)
24	10.02.57	-6.30	69.70	14	35/90/180	Wiens (1986)
25	09.12.65	-6.5	70.8	68	270/60/260	Stein (1978)
26	11.10.67	-6.03	71.34	3.0	234/76/191	Bergman and Solomon (1984)
27	11.11.67	-6.01	71.36	3.7	264/50/261	Bergman and Solomon (1984)
28	03.02.68	-6.09	71.41	7.7	284/52/280	Bergman and Solomon (1984)
29	12.20.83	-6.76	72.27	0.8	260/45/-90	††
30	07.03.87	-6.79	72.24	3.8	48/25/-125	††
31	12.04.83	-6.81	72.30	0.3	268/45/-90	††
32	11.30.83	-6.89	72.12	4100	293/35/-52	††
33	04.05.84	-6.89	72.32	1.8	284/38/-59	††
34	06.10.88	-6.94	72.20	3.1	112/10/-69	††
35	03.23.89	-7.58	72.11	0.2	13/12/-159	††
36	12.01.83	-6.68	71.81	5.0	71/41/-128	††
37	04.26.84	-6.87	71.50	2.5	299/39/-60	††
38	12.12.83	-6.61	71.46	2.4	92/44/-115	††
39	12.01.83	-6.66	71.43	4.9	310/46/-43	††
40	12.03.83	-6.54	71.41	31	303/37/-47	††
41	12.01.83	-6.47	71.33	0.5	93/40/-99	††
42	12.29.83	-6.61	71.19	1.3	100/46/-135	††
43	12.27.83	-6.57	71.16	0.4	283/45/-90	††
44	12.02.83	-6.58	71.09	2.1	131/41/-70	††
45	09.16.82	-6.96	67.78	1.0	316/40/-99	††
46	07.12.89	-8.81	67.41	2.9	137/90/180	††
47	10.12.78	-8.94	67.67	3.8	229/73/-02	††
48	01.20.88	-9.22	67.09	2.2	48/74/-08	††
59	08.19.81	-9.27	67.18	21	228/85/-05	††
50	02.03.88	-9.42	66.89	4.7	138/86/-176	††
51	10.06.90	-2.58	67.87	4.2	118/19/-109	Dziewonski *et al.* (1991c)

† Strike (°CW from N)/Dip (°CW rotation about strike)/Slip (°CCW from strike, in nodal plane)

†† See Dziewonski *et al.* (1990) for a complete listing of references to centroid moment tensor solutions for earthquakes that occurred prior to 1/01/90.

time estimated objectively and realistically, but only along the Carlsberg and Central Indian ridges. The corresponding uncertainties of transform-fault azimuths along the Southwest and Southeast Indian ridges need to be similarly re-evaluated to attain a consistent test for plate-circuit closure. The dispersions of the data indicate that on average the assigned errors are too large for both spreading rates and for azimuths of earthquake slip vectors. Because slip vectors have known systematic errors, it would be wrong to reduce their uncertainties for consistency with their smaller observed dispersion. For spreading rates, however, serious consideration should be given in future work to reducing their uncertainties to values consistent with their observed dispersion.

DISCUSSION AND CONCLUSIONS

The most important implication of our new results is that the treatment of the deforming zone in the equatorial Indian Ocean as a wide plate boundary between rigid Indian and Australian plates seems successful. Such a model gives a good fit to a set of plate-motion data that is now populous and of high quality. The plate-motion data, in combination with plate-motion data along other Indian Ocean plate boundaries, show little (if any) significant inconsistency with plate-circuit closure. Moreover, the narrow confidence limits on the new India–Australia pole of rotation give specific predictions of N–S shortening in the eastern portion of the deforming zone and N–S stretching in the western deforming zone, both of which agree with the independent observations. They further predict little deformation in the vicinity of the pole of rotation itself, which agrees with the absence of observed deformation in that region. These results reinforce our prior conclusions that the deforming zone is more usually interpreted as a wide plate boundary than as intraplate deformation.

Also important is the considerable narrowing of the quantifiable limits of several aspects of the model. In

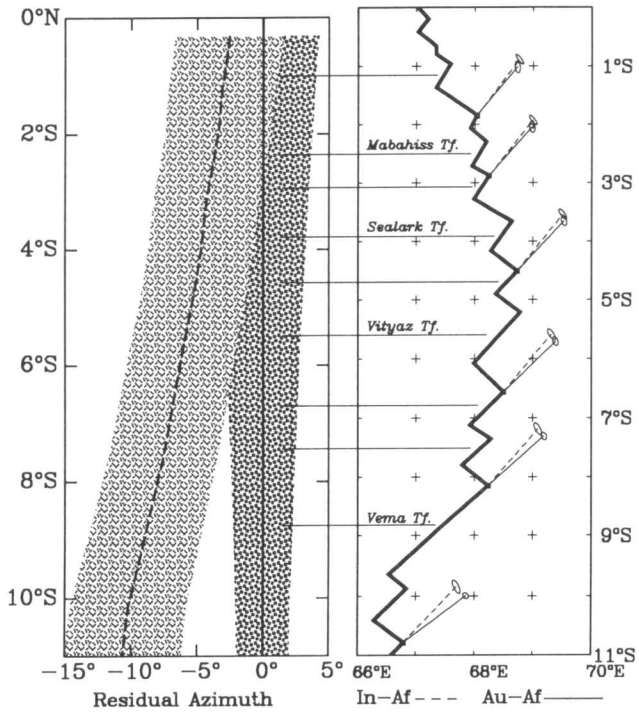

Figure 22. Comparison of directions of plate motion along the Central Indian Ridge calculated from best-fitting Africa–India and Africa–Australia angular velocities derived excluding data between the Vema and Vityaz transform faults. All uncertainties shown are 95 per cent confidence limits.

addition to the substantial shrinking of the confidence limits on the India–Australia, India–Africa and Australia–Africa angular velocities, the uncertainty in the location of the boundary between the Indian and Australian plates where it intersects the Central Indian or Carlsberg Ridge has been greatly narrowed. This is illustrated by the reduction of the confidence limits on the location of the boundary if it were very narrow: Gordon *et al.* (1990) were able to restrict it to lie only between 14°S and 5°N if data along the Central Indian Ridge and Carlsberg Ridge were used and between 9°S and 4°N when closure is enforced about the Owen and Rodriguez triple junctions. With our new data, it is now restricted to lie between 6.2°S and 9°S from data only along the Central Indian and Carlsberg ridges and between 8°S and 9°S when closure is enforced about the two triple junctions. (Limits quoted here from both sets of data are valid only if systematic errors in the data are negligible and if all errors were consistently underestimated by the same multiplicative factor.) Thus, if the boundary between India and Australia were narrow where it intersects the Central Indian Ridge, the spreading rates that we determined from our new aeromagnetic profiles would show that the Indian plate is spreading away from the African plate, not only along the entire Carlsberg Ridge, but also along the Central Indian Ridge at least as far south as ~8°S and possibly as far south as ~9°S. Similarly, the Australian plate would be spreading away from the African plate along the Central Indian Ridge at least as far north as ~9°S and possibly as far north as ~8°S.

The new plate motion data, in combination with the old, are consistent with plate-circuit closure about the Owen triple junction. If the errors assigned to the plate-motion data are accurate, then they are also consistent with closure about the Rodriguez triple junction, and place an upper bound of $7\,\mathrm{mm\,yr^{-1}}$ on combined systematic errors and intraplate deformation near the triple junction. If we assume that systematic errors are negligible and that the errors on all data have been consistently overestimated by the same multiplicative factor, then the data place a lower bound of $1\,\mathrm{mm\,yr^{-1}}$ and an upper bound of $4\,\mathrm{mm\,yr^{-1}}$ for deformation summed about the triple junction.

Although the plate-motion data along the Central Indian and Carlsberg ridges, as well as those along the Southeast Indian, Southwest Indian and Sheba ridges, are not inconsistent with the boundary between India and Australia being narrow where it intersects the Central Indian Ridge, we think it is likely that the boundary is wide because the direction of slip observed or inferred along candidate features is in the wrong direction to accommodate the motion predicted between India and Australia. The best guide to the near-ridge width of the plate boundary separating the Indian from the Australian plate is probably the near-ridge extent of seismicity, which suggests that deformation is concentrated between about 4°S to 8°S.

ACKNOWLEDGMENTS

We thank the NRL flight teams for keeping the P-3 Orion in the air for as long and as far as possible. Their success in flying all of the planned flight hours, despite two nearby hurricanes and airplane damage, was instrumental to the scientific success of this project. We also thank Jim Jarvis for his tireless efforts onshore and in the air, and Hank Fleming and Mary Peters at NRL for their efforts in making this project a success. We thank an anonymous reviewer for perceptive and helpful comments. We thank J.-Y. Royer for some helpful suggestions. RGG finished his contributions to this paper while on research leave at the Laboratoire de Géodynamique Sous-marine in Villefranche sur Mer, France. The survey was flown with joint support from the Naval Research Laboratory and the National Science Foundation. The investigators were supported by NSF grant OCE-890090 and OCE-9218541 (RGG), the Naval Research Laboratory (CD and PRV), and the Jet Propulsion Laboratory (CD).

REFERENCES

Acton, G.D. & Gordon, R.G., 1994. Paleomagnetic tests of Pacific plate reconstructions and implications for motion between hotspots, *Science,* **263,** 1246–1254.

Argus, D.F., Gordon, R.G., DeMets, C. & Stein, S., 1989. Closure of the Africa–Eurasia–North America plate motion circuit and tectonics of the Gloria fault, *J. geophys. Res.,* **94,** 5585–5602.

Atwater, T. & Mudie, J.D., 1973. Detailed near-bottom geophysical study of the Gorda Rise, *J. geophys. Res.,* **78,** 8665–8686.

Bergman, E.A. & Solomon, S.C., 1984. Source mechanisms of earthquakes near mid-ocean ridges from body waveform inversion: Implications for the early evolution of oceanic lithosphere, *J. geophys. Res.,* **89,** 11 415–11 441.

Bergman, E.A. & Solomon, S.C., 1985. Earthquake source mechanisms from body waveform inversion and intraplate tectonics in the northern Indian Ocean, *Phys. Earth planet. Inter.,* **40,** 1–23.

Bergman, E.A., Nabelek, J.L. & Solomon, S.C., 1984. An extensive region of off ridge normal-faulting earthquakes in the southern Indian Ocean, *J. geophys. Res.*, **89,** 2425–2443.

Blakely, R. & Cox, A., 1972. Identification of short polarity events by transforming marine magnetic profiles to the pole, *J. geophys. Res.*, **77,** 4339–4349.

Bull, J.M., 1990. Structural style of intra-plate deformation, Central Indian ocean Basin: Evidence for the role of fracture zones, *Tectonophysics,* **184,** 213–228.

Bull, J.M. & Scrutton, R.A., 1990. Fault reactivation in the central Indian Ocean and the rheology of oceanic lithosphere, *Nature,* **344,** 855–858.

Chamot-Rooke, F.J., de Voogd, B. & Phèdre Working Group, 1993. Intraplate shortening in the central Indian Ocean determined from a 2100-km-long north–south deep seismic reflection profile, *Geology,* **21,** 1043–1046.

Chase, C.G., 1978. Plate kinematics: The Americas, East Africa, and the rest of the world, *Earth planet. Sci. Lett.*, **37,** 355–368.

Chaubey, A.K., Krishna, K.S., Subba Raju, L.V. & Gopala Rao, D., 1990. Magnetic anomalies across the southern Central Indian Ridge: Evidence for a new transform fault, *Deep-Sea Res.*, **37,** 647–656.

Cochran, J.R., 1990. Himalayan uplift, sea level, and the record of Bengal Fan sedimentation at the ODP leg 116 sites, in *Proceedings of the Ocean Drilling Program, Scientific Results, 116,* pp. 397–414, eds Cochran, J.R., Stow, D.A.V. *et al.*, Ocean Drilling Program, College Station, TX.

Courtillot, V. & Le Mouel, J.L., 1988. Time variations of the Earth's magnetic field, *Ann. Rev. Earth planet. Sci.*, **16,** 389–476.

Cox, A. & Gordon, R.G., 1984. Paleolatitudes determined from paleomagnetic data from vertical cores, *Rev. Geophys. Space Phys.*, **22,** 47–72.

Curray, J.R. & Moore, D.G., 1971. Growth of the Bengal Deep-Sea Fan and denudation in the Himalayas, *Bull. geol. Soc. Am.*, **82,** 563–572.

Curray, J.R. & Munasinghe, T., 1989. Timing of intraplate deformation, northeastern Indian Ocean, *Earth planet. Sci. Lett.*, **94,** 71–77.

Curray, J.R., Emmel, F.J., Moore, D.G. & Raitt, R.W., 1982. Structure, tectonics, and geological history of the northeastern Indian Ocean, in *The Ocean Basins and Margins, volume 6: The Indian Ocean,* pp. 399–450, eds Naim, A.E.W. & Stehli, F.G., Plenum Press, New York.

DeMets, C., 1993. Earthquake slip vectors and estimates of present-day plate motions, *J. geophys. Res.*, **98,** 6703–6714.

DeMets, C., Gordon, R.G. & Argus, D.F., 1988. Intraplate deformation and closure of the Australia–Antarctica–Africa plate circuit, *J. geophys. Res.*, **93,** 11 877–11 897.

DeMets, C., Gordon, R.G., Argus, D.F. & Stein, S., 1990. Current plate motions, *Geophys. J. Int.*, **101,** 425–478.

DeMets, C., Gordon, R.G., Argus, D.F. & Stein, S., 1994. Effect of recent revisions to the geomagnetic reversal time scale on estimates of current plate motions, *Geophys. Res. Lett.*, in press.

Dziewonski, A.M., Ekström, G., Woodhouse, J.H. & Zwart, G., 1990. Centroid-moment tensor solutions for October–December 1989, *Phys. Earth planet. Inter.*, **62,** 194–207.

Dziewonski, A.M., Ekström, G., Woodhouse, J.H. & Zwart, G., 1991a. Centroid-moment tensor solutions for January–March 1990, *Phys. Earth planet. Inter.*, **65,** 197–207.

Dziewonski, A.M., Ekström, G., Woodhouse, J.H. & Zwart, G., 1991b. Centroid-moment tensor solutions for April–June 1990, *Phys. Earth planet. Inter.*, **66,** 133–143.

Dziewonski, A.M., Ekström, G., Woodhouse, J.H. & Zwart, G., 1991c. Centroid-moment tensor solutions for October–December 1990, *Phys. Earth planet. Inter.*, **68,** 201–214.

Dziewonski, A.M., Ekström, G., Salganik, M.P. & Zwart, G., 1992a. Centroid-moment tensor solutions for January–March 1991, *Phys. Earth planet. Inter.*, **70,** 7–15.

Dziewonski, A.M., Ekström, G. & Salganik, M.P., 1992b. Centroid-moment tensor solutions for April–June 1991, *Phys. Earth planet. Inter.*, **71,** 6–14.

Dziewonski, A.M., Ekström, G. & Salganik, M.P., 1992c. Centroid-moment tensor solutions for October–December 1991, *Phys. Earth planet. Inter.*, **74,** 89–100.

Dziewonski, A.M., Ekström, G. & Salganik, M.P., 1993a. Centroid-moment tensor solutions for January–March 1992, *Phys. Earth planet. Inter.*, **77,** 143–150.

Dziewonski, A.M., Ekström, G. & Salganik, M.P., 1993b. Centroid-moment tensor solutions for April–June 1992, *Phys. Earth planet. Inter.*, **77,** 151–163.

Dziewonski, A.M., Ekström, G. & Salganik, M.P., 1993c. Centroid-moment tensor solutions for July–September 1992, *Phys. Earth planet. Inter.*, **79,** 287–297.

Eittreim, S. & Ewing, J., 1972. Mid-plate tectonics in the Indian Ocean, *J. geophys. Res.*, **77,** 6413–6421.

Engel, C.G. & Fisher, R.L., 1975. Granitic to ultramafic rock complexes of the Indian Ocean ridge system, western Indian Ocean, *Bull. geol. Soc. Am.*, **86,** 1553–1578.

Fisher, R.L., Sclater, J.G. & Mckenzie, D.P., 1971. Evolution of the central Indian Ridge, western Indian Ocean, *Bull. geol. Soc. Am.*, **82,** 553–562.

Fisher, R.L., Jantsch, M.Z. & Comer, R.L., 1982. General Bathymetric Chart of the Oceans (GEBCO), Sheet 5.09, Canadian Hydrographic Service, Ottawa.

Fox, P.J. & Gallo, D.G., 1986. The geology of North Atlantic transform plate boundaries and their aseismic extensions, in *The Western North Atlantic Region, Decade of North American Geology M,* pp. 157–172, eds Vogt, P.R. & Tucholke, B.E., Geological Society of America, Boulder, CO.

Geller, C.A., Weissel, J.K. & Anderson, R.N., 1983. Heat transfer and intraplate deformation in the central Indian Ocean, *J. geopyhys. Res.*, **88,** 1018–1032.

Gordon, R.G. & DeMets, C., 1989. Present-day motion along the Owen Fracture Zone and Dalrymple Trough in the Arabian Sea, *J. geophys. Res.*, **94,** 5560–5570.

Gordon, R.G., Stein, S., DeMets, C. & Argus, D.F., 1987. Statistical tests for closure of plate motion circuits, *Geophys. Res. Lett.*, **14,** 587–590.

Gordon, R.G., DeMets, C. & Argus, D.F., 1990. Kinematic constraints on distributed lithospheric deformation in the equatorial Indian Ocean from present motion between the Australian and Indian plates, *Tectonics,* **9,** 409–422.

Gutenberg, B. & Richter, C.F., 1954. *Seismicity of the Earth and Associated Phenomena,* 2nd edn, Princeton University Press, Princeton, NJ.

Harland, W.B., Cox, A.V., Llewellyn, P.G., Pickton, C.A.G., Smith, A.G. & Walters, R., 1982. *A Geologic Time Scale,* Cambridge University Press, New York.

Haxby, W.F., 1987. Gravity field of the world's oceans, Map, NOAA, Boulder, CO.

Huang, P.Y. & Solomon, S.C., 1987. Centroid depths and mechanisms of mid-ocean ridge earthquake in the Indian Ocean, Gulf of Aden, and Red Sea, *J. geophys. Res.*, **92,** 1361–1382.

Joselyn, J.A. & Tsurutani, B.T., 1990. Geomagnetic sudden impulses and storm sudden commencements, *EOS, Trans. Am. geophys. Un.*, **71,** 1808–1809.

Kanaev, V.F., 1975. Relief of the rift zone and its role in the general system of ocean bottom morphology, in *Rift Zones of the World Ocean,* pp. 32–62, eds Vinogradov, A.P. & Udintsev, G.B., John Wiley, New York.

Laughton, A.S., 1975. General Bathymetric Chart of the Oceans (GEBCO), sheet 5.5, Canadian Hydrographic Service, Ottawa.

Laughton, A.S., Whitmarsh, R.B. & Jones, M.T., 1970. The

evolution of the Gulf of Aden, *Phil. Trans. R. Soc. Lond.*, A, **267,** 227–266.

Liu, C.S., Curray, J.R. & McDonald, J.M., 1983. New constraints on the tectonic evolution of the eastern Indian Ocean, *Earth planet. Sci. Lett.*, **65,** 331–342.

Macdonald, K.C., 1982. Mid-ocean ridges: Fine scale tectonic, volcanic and hydrothermal processes within the plate boundary zone, *Ann. Rev. Earth planet. Sci.*, **10,** 155–190.

Marks, K.M. & Stock, J.M., 1991. High-precision location of fracture zones in Geosat data: The Macquarie triple junction region (abstract), *Trans. Am. geophys. Un.*, **72,** 444.

McAdoo, D.C. & Sandwell, D.T., 1985. Folding of oceanic lithosphere, *J. geophys. Res.*, **90,** 8563–8569.

McKenzie, D. & Jackson, J., 1983. The relationship between strain rates, crustal thickening, paleomagnetism, finite strain, and fault movements within a deforming zone, *Earth planet. Sci. Lett.*, **65,** 182–202.

McKenzie, D.P. & Sclater, J.G., 1971. The evolution of the Indian Ocean since the late Cretaceous, *Geophys. J. R. astr. Soc.*, **24,** 437–528.

Minster, J.B. & Jordan, T.H., 1978. Present-day plate motions, *J. geophys. Res.*, **83,** 5331–5354.

Minster, J.B. & Jordan, T.H., 1984. Vector constraints on Quaternary deformation of the western United States east and west of the San Andreas Fault, in *Tectonics and Sedimentation along the California Margin,* Fieldtrip Guidebook 38, pp. 1–16, eds Crouch, J. K. & Bachman, S.B., Pacific Section, SEPM, Los Angeles, CA.

Minster, J.B., Jordan, T.H., Molnar, P. & Haines, E., 1974. Numerical modeling of instantaneous plate tectonics, *Geophys. J. R. astr. Soc.*, **36,** 541–576.

Mitchell, N.C., 1991. An evolving ridge system around the Indian Ocean triple junction, *Mar. geophys. Res.*, **13,** 173–201.

Molnar, P., Pardo-Casas, F. & Stock, J., 1988. The Cenozoic and Late Cretaceous evolution of the Indian Ocean Basin: Uncertainties in the reconstructed positions of the Indian, African and Antarctic plates, *Basin Res.*, **1,** 23–40.

Parker, R.L., 1974. Stacking marine magnetic anomalies: A critique, *Geophys. Res. Lett.*, **1,** 259–260.

Parson, L.M., Patriat, P., Searle, R.C. & Briais, A.R., 1993. Segmentation of the Central Indian Ridge between 12°12′S and the Indian Ocean triple junction, *Mar. geophs. Res.*, **15,** 265–282.

Petroy, D.E. & Wiens, D.A., 1989. Historical seismicity and implications for diffuse plate convergence in the northeast Indian Ocean, *J. geophys. Res.*, **94,** 12 301–12 319.

Press, W.H., Flannery, B.P., Teukolsky, S.A. & Vetterling, W.T., 1986. *Numerical Recipes: The Art of Scientific Computing,* Cambridge University Press, New York.

Royer, J.-Y. & Chang, T., 1991. Evidence for relative motions between the Indian and Australian plates during the last 20 Myr from plate tectonic reconstructions: Implications for the deformation of the Indo-Australian plate, *J. geophys. Res.*, **96,** 11 779–11 802.

Royer, J.-Y. & Sandwell, D.T., 1989. Evolution of the eastern Indian Ocean since the Late Cretaceous: Constraints from Geosat altimetry, *J. geophys. Res.*, **94,** 13 755–13 800.

Schouten, H. & McCamy, K., 1972. Filtering marine magnetic anomalies, *J. geophys. Res.*, **77,** 7089–7099.

Searle, R.C., 1986. GLORIA investigations of oceanic fracture zones: comparative study of the transform fault zone, *J. geol. Soc. Lond.*, A, **143,** 743–756.

Searle, R.C. & Laughton, A.S., 1977. Sonar studies of the Mid-Atlantic Ridge and Kurchatov Fracture Zone, *J. geophys. Res.*, **82,** 5313–5328.

Spiegel, M.R., 1975. *Schaum's Outline of Theory and Problems of Probability and Statistics,* McGraw-Hill, New York.

Stein, S., 1978. An earthquake swarm on the Chagos–Laccadive Ridge and its tectonic implications, *Geophys. J. R. astr. Soc.*, **55,** 577–588.

Stein, S. & Gordon, R.G., 1984. Statistical tests of additional plate boundaries from plate motion inversions, *Earth planet. Sci. Lett.*, **69,** 401–412.

Stein, S. & Okal, E.A., 1978. Seismicity and tectonics of the Ninetyeast Ridge area: Evidence for internal deformation of the Indian plate, *J. geophys. Res.*, **83,** 2233–2245.

Stein, C.A., Cloetingh, S.A.P.L. & Wortel, M.J.R., 1989. Seasat-derived gravity constraints on stress and deformation in the northeastern Indian Ocean, *Geophys. Res. Lett.*, **16,** 823–826.

Sykes, L.R., 1970. Seismicity of the Indian Ocean and a possible nascent island arc between Ceylon and Australia, *J. geophys. Res.*, **75,** 5041–5055.

Telford, W.M., Geldart, L.P., Sheriff, R.E. & Keys, D.A., 1976. *Applied Geophysics,* Cambridge University Press, Cambridge.

Weissel, J.K., Anderson, R.N. & Geller, C.A., 1980. Deformation of the Indo-Australian plate, *Nature,* **287,** 284–291.

Wiens, D.A., 1986. Historical seismicity near Chagos: A complex deformation zone in the equatorial Indian Ocean, *Earth planet. Sci. Lett.*, **76,** 350–360.

Wiens, D.A. & Stein, S., 1984. Intraplate seismicity and stresses in young oceanic lithosphere, *J. geophys. Res.*, **89,** 11 442–11 464.

Wiens, D.A., DeMets, C., Gordon, R.G., Stein, S., Argus, D., Engeln, J.F., Lundgren, P., Quible, D., Stein, C., Weinstein, S. & Woods, D.F., 1985. A diffuse plate boundary model for Indian Ocean tectonics, *Geophys. Res. Lett.*, **12,** 429–432.

Wilson, J.T., 1965. A new class of faults and their bearing on continental drift, *Nature,* **207,** 343–347.

Zuber, M.T., 1987. Compression of oceanic lithosphere: An analysis of intraplate deformation in the Central Indian Basin, *J. geophys. Res.*, **92,** 4817–4826.